External Flow Effects in the Engine/Airframe Integration Testing Technique

A new Thrust/Drag Bookkeeping Approach at the German-Dutch Wind Tunnels

Christian Sabater Campomanes

Technische Universiteit Delft

TU Delft Delft University of Technology

DNW German-Dutch Wind Tunnels

Challenge the future

External Flow Effects in the Engine/Airframe Integration Testing Technique

A new Thrust/Drag Bookkeeping Approach at the German-Dutch Wind Tunnels

by

Christian Sabater Campomanes

in partial fulfillment of the requirements for the degree of

Master of Science
in Aerospace Engineering

at the Delft University of Technology,
to be defended publicly on Friday October 13, 2017 at 09:30 AM.

Supervisor, TU Delft:	Prof. Dr.-Ir. G. Eitelberg
Supervisor, DNW:	Ir. G. H. Hegen
Thesis Committee:	Dr. A. Gangoli Rao
	Dr. R. P. Dwight

An electronic version of this thesis is available at http://repository.tudelft.nl/.
Thesis registration number: 163#17#MT#FPP

TU Delft Delft University of Technology

DNW German-Dutch Wind Tunnels

PREFACE

'The formulation of a problem is often more essential than its solution, which may be merely a matter of mathematical or experimental skill. To raise new questions, new possibilities, to regard old problems from a new angle requires creative imagination and marks real advances in science' [1]. Einstein wrote this quote in his book *'The Evolution of Physics'* to remark the importance of curiosity. After writing my thesis I can say that finding the problems to tackle in this project was one of the most challenging, yet interesting tasks that I have ever been faced with. My thesis was in overall a roller coaster full of emotions: the struggling of the first CFD setup, the satisfaction of obtaining preliminary consistent results, the thrill of wind tunnel tests and the strive to fit all the pieces of the puzzle together. This process boosted my curiosity and interest for research as I would have never imagined two years ago, when I started my Master in Delft.

I would not have successfully completed this thesis without the support of many people. First of all, special thanks to my supervisors Sinus and Georg. Together, they offered me the opportunity of working for one year at the German-Dutch Wind Tunnels, where I learned experimental aerodynamics from an unique point of view. I deeply appreciate the weekly meetings with Sinus, pushing the project forward with his curiosity and sharing his expertise in engine/airframe integration testing. I strongly value the key suggestions from Georg, always making sure that I communicate my work effectively, having the best approach towards my research.

There are several colleagues from DNW that I am really grateful for. Without the help of Onno, Alfons, Wouter, Paul and Rick the wind tunnel test would have not been possible. Also thanks a lot to the fellow interns Marcus, Sidney and Ali for the friendly company, making my time here even more enjoyable.

I also have to appreciate the support of my parents and sister, always present during my studies. They encouraged me to thoughtfully plan, set and reach my goals. Thinking in my family makes me realize how lucky I am.

Last but not least, special thanks to you, Alexandra, for your support, help and confidence in me. You are the best proofreader any Master student could ever wish for. From you I have learned to continuously improve and put my mark even higher. We started in Delft side by side and here we are, continuing our path together.

Christian Sabater Campomanes
Vollenhove, September 2017

CONTENTS

SUMMARY

The integration of the engine with the airframe is investigated in the German-Dutch Wind tunnels (DNW) using special scale engines called Turbofan Powered Simulators (TPS). The bookkeeping of thrust and drag must be clear. The TPS thrust is determined under static conditions in a calibration facility, and then subtracted in the wind tunnel test from the balance force of the aircraft model (airframe + TPS) to obtain the airframe drag including jet interference drag. A critical assumption valid for traditional turbofan engines is that the external flow does not affect the statically calibrated thrust. However, with the rise of more efficient engines with higher bypass ratio this may not be the case due to the close coupling between the engine flow and the wing. The objective of this Thesis is to identify the current limitations of the testing procedure as well as to produce scientific basis to deal with these limitations. This is achieved by means of a consistent thrust/drag bookkeeping combining numerical methods and a modified experimental setup.

External flow effects are identified by means of the analysis of theoretical models, the comparison with testing procedures undertaken in similar facilities, the review of standard bookkeeping techniques of full-scale turbofan engines and the analysis of previous test data. The change in thrust is quantified using a mathematical model integrated in an error propagation study by means of Monte Carlo simulations. The influence of the external flow and wing pressure field is further studied through a numerical analysis in RANS-SST for a very high bypass ratio TPS unit, and a Through-Flow Nacelle respectively. The latter configuration is also tested in the Low Speed Tunnel in DNW to investigate which instrumentation can be used to detect external flow effects in the future. In this case the velocity in the fan exhaust plane is measured with a hot wire and static pressure sensors are placed in the intake, exhaust and boattail.

The theoretical, numerical and experimental approach show that the external flow and wing pressure field change the conditions in the TPS exhaust with respect to static calibration. In the wind tunnel, the nozzle exhaust shear layer decreases in size as the difference in velocities between plume and free air is decreased, reducing the flow spreading rate and increasing the local pressure at the nozzle exit plane. The local Nozzle Pressure Ratio is reduced. This leads to flow suppression, the reduction of the fan mass flow and exhaust velocity. In addition, the scrubbing and boattail drag, currently bookkept as loss of thrust in the modified standard net thrust, are changed from static to wind tunnel conditions. These effects change the TPS thrust leading towards an improperly bookkeeping of the aircraft installation drag. The bias error produced by external flow effects is one order of magnitude higher than the random instrumentation error and should be corrected for, especially at low power settings. Differences decrease proportionally to the Fan Nozzle Pressure Ratio until chocked conditions are reached, where the freestream velocity has no influence in the TPS performance.

A possible solution lies in the advanced derivation of thrust and drag. The current approach neglects the thrust contribution from the nozzle exhaust to infinite downstream. According to the definition of the Jones thrust, a better solution lies in the assumption that the flow is expanded from the exhaust to infinity downstream without any transfer of energy of momentum. The decrease in mass flow and velocity can be effectively captured by pressure taps located at the intake or fan plane. A linear correlation exists between both stations, that can be used for the bookkeeping of the TPS thrust in the wind tunnel according to additional calibration in the wind tunnel. The new bookkeeping method can also be used to correct for the decrease in local jet exhaust Mach number from design conditions, the parameter of interest in engine/airframe integration tests.

The research presents and solves the limitations of the new generation of turbofan engines by accounting for the local conditions at the TPS exhaust due to external flow effects. The new thrust/drag bookkeeping method leads to optimized configurations by improving the accuracy of engine/airframe integration tests.

NOMENCLATURE

$\bar{V}$	Velocity vector
$\bar{V}_{HW}$	Average Velocity Obtained with the hot wire
$\dot{m}^*_{fan}$	Fan mass flow rate at chocked nozzle
$\dot{m}_0$	Freestream mass flow
$\dot{m}_{core}$	Core mass flow rate
$\dot{m}_{fan_{ac}}$	Actual Fan mass flow rate
$\dot{m}_{fan_{id}}$	Ideal Fan mass flow rate
$\dot{m}_{fan_{NONDIM}}$	Dimensionless Fan mass flow rate
$\dot{m}_{fan}$	Fan mass flow rate
$\dot{m}_I$	Intake mass flow rate
η_{prop}	Propulsive Efficiency
γ	Heat capacity ratio
Λ	Source Strength
$\hat{\mathbf{n}}$	Normal vector
μ	Mean
ϕ	Circumferential location of pressure sensor
ϕ_P	Potential Function
ϕ_{AB}	Force generated by the streamtube flow on the core cowl
ϕ_a	Afterbody cowl force
ϕ_{CB}	Force generated by the streamtube flow on the engine hub
ϕ_{cowl}	Force generated by the streamtube flow on the fan cowl
ϕ_c	Forebody cowl force
ϕ_{nac}	Force generated by the flow on the nacelle
ϕ_{plug}	Force generated by the streamtube flow on the core plug
$\phi_{post,0}$	Force generated by the flow on the core post-exit streamtube
$\phi_{post,1}$	Force generated by the flow on the fan post-exit streamtube
ϕ_{post}	Force generated by the flow on the post-exit streamtube
ϕ_{pre}	Force generated by the flow on the pre-entry streamtube
ψ_P	Stream Function
ρ	Density

σ	Standard Deviation
τ	Shear force
θ	Local surface angle
A_0	Freestream area of streamtube infinitely upstream
A_00	Freestream area of streamtube infinitely downstream
A_1	Intake Area
A_18	Fan nozzle throat area
A_19	Fan nozzle exhaust area
A_2	Fan face Area
A_7	Nozzle entrance Area
A_8	Core nozzle throat area
A_9	Core nozzle exhaust area
A_{ac}	Actual nozzle exit area
$A_{flatplate}$	Flat Plate Cross Section Area
A_{id}	Ideal nozzle exit area
BPR	Bypass Ratio
C_D	Discharge coefficient
C_V	Velocity coefficient
$C_{P,fan}$	Pressure Coefficient at the Fan Exhaust Plane
C_P	Pressure Coefficient
CD_{BM}	Bellmouth discharge coefficient
$CNPR$	Core nozzle pressure ratio
D	Nozzle exhaust diameter
D_a	Afterbody drag
D_cowl	Cowl drag
D_I	Internal drag
D_P	Drag at power conditions
D_plug	Plug drag
$D_{a,datum}$	Datum afterbody drag
D_a	Afterbody drag
$D_{boattail}$	Boattail Drag
$D_{c,datum}$	Datum intake flow drag
D_c	Forebody drag
D_{INST}	Installed drag

D_{INTERF} Interference drag

D_J Jet interference drag

D_{nac} Nacelle drag

D_{post} Post-exit drag

D_{pre} Pre-entry drag (equivalent to additive drag)

D_{spill} Spillage drag

F Absolute stream force

F'_N Overall net thrust

$F^*_{G,19}$ Fan modified gross thrust

$F^*_{G,9}$ Core modified gross thrust

F^*_N Modified standard net thrust

F_x Thrust force component in x (freestream) direction

$F_{BAL,cal}$ Calibration balance force

$F_{BAL,WT}$ Wind tunnel balance force

F_{BAL} Balance force

F_{BM} Bellmouth force

$F_{G,000}$ Absolute stream force relative to ambient conditions in infinitely downstream core streamtube station

$F_{G,00}$ Absolute stream force relative to ambient conditions in infinitely downstream streamtube station

$F_{G,0}$ Absolute stream force relative to ambient conditions in the infinitely upstream streamtube station

$F_{G,100}$ Absolute stream force relative to ambient conditions in infinitely downstream fan streamtube station

$F_{G,19,id_{con-div}}$ Gross thrust of ideal convergent-divergent ideal flexible nozzle

$F_{G,19,id_{con}}$ Gross thrust of ideal convergent nozzle

$F_{G,19}$ Fan gross thrust: absolute stream force relative to ambient conditions in the fan nozzle exhaust

$F_{G,1}$ Absolute stream force relative to ambient conditions in the nacelle intake

$F_{G,2}$ Absolute stream force relative to ambient conditions in the fan face

$F_{G,9}$ Core gross thrust: absolute stream force relative to ambient conditions in the core nozzle exhaust

F_{int} Intrinsic Thrust

F_N Standard net thrust

F_{post} Post-exit Thrust (equivalent to post-exit drag)

F_{pre} Pre-entry thrust (equivalent to pre-entry or additive drag)

F_{seal} Sealing force

$F_{X,fan}$ Momentum at the fan exhaust plane

$FNPR$ Fan nozzle pressure ratio

FPR Fan Pressure Ratio

K_s	Spillage drag factor
M	Mach number
M_0	Freestream Mach number
M_9	Mach number at the nozzle exit
M_e	Equivalent Mach number in the Engine Calibration Facility
n_{fan}	Number of cell elements in the fan exhaust plane
$n_{i,HW}$	Number of discrete sections after interpolation of Hot Wire velocity field
NPR	Nozzle pressure ratio
NPR^*	Choked nozzle pressure ratio
$P_{s,00}$	Static pressure infinitely downstream
$P_{s,0}$	Static pressure infinitely upstream
$P_{s,BM}$	Static pressure at the bellmouth throat
$P_{s,boattail}$	Average Pressure at the Through-Flow Nacelle Boattail
$P_{s,e,19}$	Static local pressure at the fan nozzle exhaust
$P_{s,e,9}$	Static local pressure at the core nozzle exhaust
$P_{s,e}$	Static local pressure at the nozzle exhaust
$P_{s,tank}$	Tank static pressure
P_s	Static pressure
$P_{t,0}$	Total Pressure at the infinitely upstream station (Ambient total pressure)
$P_{t,13}$	Total Pressure at the entrance of the fan duct
$P_{t,17}$	Total Pressure at the entrance of the fan nozzle
$P_{t,18}$	Total Pressure at the fan nozzle throat
$P_{t,2}$	Total Pressure at the fan face
$P_{t,core}$	Total pressure at the TPS core duct
$P_{t,fan}$	Total pressure at the TPS fan duct
R	Radius
Re	Reynolds number
RPM	Revolutions per minute
SFC	Specific Fuel Consumption
$T_{t,BM}$	Total temperature at the bellmouth lip
$T_{t,core}$	Total temperature at the TPS core duct
$T_{t,fan}$	Total temperature at the TPS fan duct
V_0	Freestream velocity
$V_{9,eff}$	Effective exit velocity

x Longitudinal distance from flat plate to fan exhaust plane

X^* Dimensionless longitudinal distance along the Through-Flow Nacelle Boattail

y^+ Dimensionless wall distance

AGARD Advisory Group for Aerospace Research and Development

AIAA American Institute of Aeronautics and Astronautics

ARA Aircraft Research Association

ARC Aerospace Research Center

BM Bellmouth

CFD Computational Fluid Dynamics

CRUF Counter Rotating Ultra-High Bypass Ratio

DC Distortion Ratio

DLR German Aerospace Center

DNW German-Dutch Wind Tunnels

DSFR Dual Separate Flow Reference

ECF Engine Calibration Facility

ESWIRP European Strategic Wind Tunnels Improved Research Potential

ETOPS Extended Range Twin Engine Operations

HST High-speed tunnel

HW Hot Wire

HWB Hybrid Wing Body

ISA International Standard Atmosphere

LLF Large low-speed facility

LST Low-Speed Tunnel

MIDAP Ministry-Industry Drag Analysis Panel

MST Mach Simulation Tank

NASA National Aeronautics and Space Administration

NLR Dutch Aerospace Laboratory

ONERA French Aerospace Lab

PIV Particle Image Velocimetry

PN Isolated pylon/nacelle configuration

RANS Reynolds Average Navier Stokes

SAE Society of Automotive Engineers

SST Shear Stress Transport Turbulence Model

TDI Tech Development inc

TFN	Through-Flow Nacelle
TPS	Turbofan Propulsion Simulator
WB	Wing/body configuration
WBPN	Wing/body/pylon/nacelle configuration
WT	Wind Tunnel

1

INTRODUCTION

This chapter places and motivates the research topic in its historical framework. The current testing technique is introduced and compared with respect to other facilities globally. Finally the research questions are introduced.

1.1. HISTORICAL BACKGROUND

With the continuous growth of commercial aviation, environmental and economic concerns are key drivers to the reduction of the aerodynamic drag and specific fuel consumption [2], [3]. The next generation of commercial aircraft is expected to considerably reduce the direct operating costs, the noise and the greenhouse gasses emissions [4]. As a result, the airframe manufacturers are putting great effort in the reduction of the drag of the complete aircraft, while engine manufacturers are reducing the specific fuel consumption of the powerplant by increasing the propulsive efficiency through the bypass ratio. Despite airframe and engine companies follow different paths, the integration of both must come together [5] in order to achieve the desired improved performance.

Since the Wright Brothers, engineers have been concerned with the proper integration of the engine within the airframe [6]. The optimum configuration depends on a combination of aerodynamic performance, flight mechanics, weight, flutter, engine fuel consumption, maintenance, one engine out performance during second segment climb and Extended Range Twin Engine Operations (ETOPS), thrust reverser and safety requirements. The evolution of the turbofan led to the collocation of the engines under the wing. This configuration has the advantages of a good weight distribution and maintenance accessibility. However, it comes with the penalty of a longer landing gear and a stronger interference between the wing, pylon and engine, leading to aerodynamic performance losses. This aerodynamic interference is more important nowadays, with the continuous increase of the engine diameter associated with more efficient engines with higher Bypass Ratio. In addition of the increased friction drag due to the increased nacelle, a closer coupling between the engine flow and the wing will occur [2].

Aircraft and propulsive units must be conceived from the very heart of the integration process. Maximum benefits are achieved by an integral redesign of the airframe. Otherwise, if the integration process starts too late, an excessive amount of resources spent and a lack of performance will be the only result. In a similar way, by replacing an existing engine on an aircraft by a more efficient engine, only partial savings in efficiency will be achieved. For example, if a more efficient engine is employed the wing should be resized to carry less fuel, reducing the wing weight and as a result achieving further fuel efficiency gains in a snowball effect.

Engine/airframe interference is defined by Harris (1992) [7] as the difference in the performance of the integrated engine/ airframe compared with the sum of the individual engine and airframe performance at a given value of flight Mach, angle of attack and power settings. When two or more bodies are brought together in close proximity with a common external flow each one affects the flow field around the other [8]. As a result the drag is not equal to the sum of the individual bodies in isolation. Interference drag is the second largest contributor to the total drag of the installation after profile drag according to Boeing engineers Dagget, Brown and Kawai [9].

Engine/airframe interference then is based on reciprocity and is largely characterized by:

- The effect that the nacelle, the pylon, the intake flow and the exhaust jet (thrust streamtube) has in changing the flow around the wing.
- The effect that the flow around the wing has on the nacelle, the pylon, the intake and the jet (thrust streamtube).
- Interactions among the different components, such as in the interface between wing and pylon and the nacelle and pylon.

Interaction originates because engine and airframe are tested independently. According to the MIDAP [8], if the "drag of a complete aircraft with an operating powerplant in an infinite freestream could be calculated directly, then there would be no interference drag". However, this is not possible and the magnitude of the interference effect acting on a particular part of a body depends on the bookkeeping system.

The integration of engine with the airframe can effectively be investigated in wind tunnels using special engine simulators called Turbofan Powered Simulators (TPS) [10]. This technique has become the standard in wind tunnel testing during the last 40 years [11], as it provides the most realistic flow simulation for the study of the turbofan/airframe interference drag [12]. A reduction of aircraft drag of 1% by increasing the performance generates savings in Direct Operating Costs more than 2.5 times the costs of the TPS program [13]. Because of its complexity, engine/airframe integration tests are undertaken in a few research centers. Among others, the German-Dutch Wind tunnels, DNW, has been contributing during many years in the development of TPS as prime choice for the simulation of installation effects.

1.1.1. INTEGRATION OF ULTRA-HIGH BYPASS RATIO TURBOFAN

During the last years engine manufacturers have been driven towards the increase in the engine Bypass Ratio, defined as the mass flow rate of the bypass stream $\dot{m}_{fan}$ to the mass flow rate of the core $\dot{m}_{core}$, in order to reduce the Specific Fuel Consumption (SFC) and noise of the isolated configuration.

$$BPR = \frac{\dot{m}_{fan}}{\dot{m}_{core}} \tag{1.1}$$

The decrease of the exhaust jet velocity associated to modern high bypass ratio turbofan engines increases its propulsive efficiency:

$$\eta_{prop} = \frac{2}{1 + \frac{V_{9,eff}}{V_0}} \tag{1.2}$$

As shown in Figure 1.1 the increase in the aircraft efficiency with higher bypass ratio engines will be neutralized, among others, by the increase in the installation drag [6]. The optimization of the whole system engine/pylon/airframe is necessary to achieve low interference drag and can determine the success of an aircraft [14]. As a result, nowadays is more important than ever to provide an accurate method for modelling, predicting and assessing the complex installation effects in the overall aircraft performance. This entails technical challenges for airframe aerodynamic, structures, systems and propulsion engineers [4].

The further increase in the bypass ratio not only possesses a challenge for airframe and engine manufacturers, but also for wind tunnel specialists [12]. The definition of thrust and drag must be clear as the determination of thrust of the TPS is undertaken under static conditions in an engine calibration facility, and then subtracted in the wind tunnel test from the measured total (airframe + TPS) balance force in order to obtain the airframe drag. A critical assumption valid for traditional turbofan engines is that the external flow does not affect the internal thrust. However, with Ultra High Bypass Ratio engines operating at unchoked conditions this may not be the case due to the close coupling between the engine flow and the wing. For example, a decrease in thrust due to external flow in comparison with static conditions may be wrongly accounted as an increase in airframe drag.

The traditional experimental approach alone cannot answer all the questions raised from an optimized propulsion system. New requirements, problems and solutions make a broader perspective necessary to tackle engine/airframe integration testing with special consideration to the thrust/drag bookkeeping method and the influence of external flow on thrust. A combination between wind tunnel tests and numerical simu-

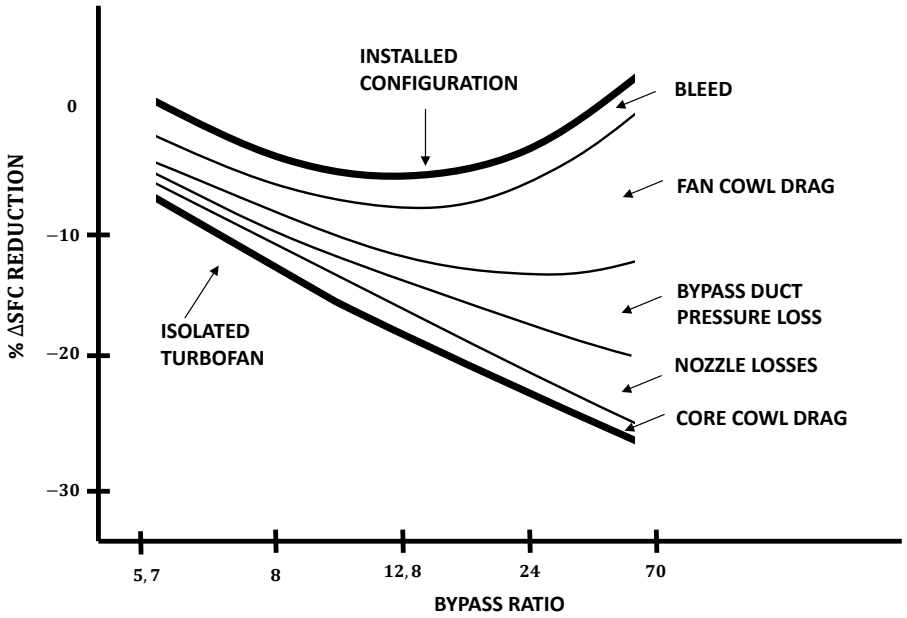

Figure 1.1: Increase in Specific Fuel Consumption (equivalent to increase in drag) from isolated to installed turbofan as a result of the increase in the bypass ratio due to installed drag. Source: *Advanced Ducted Engine Nacelle Aerodynamics and Integration Testing* [15]

lations is likely necessary to undertake the analysis of the ultra-high bypass ratio turbofan interference drag. As a result, the research objectives for this Master Thesis are:

1. To identify the current limitations of the engine/airframe integration testing performed at the German-Dutch Wind Tunnels (DNW) by an exhaustive assessment of the TPS technique in relation to theoretical models, policies from other facilities and full scale turbofan testing.

2. To produce scientific basis to deal with the identified limitations by means of establishing a consistent thrust/drag bookkeeping using numerical methods and a modified experimental setup.

1.2. CURRENT ENGINE/AIRFRAME INTEGRATION TESTING TECHNIQUE AT DNW

The German-Dutch Wind Tunnels (DNW) is a non-profit foundation under Dutch law, established by the aerospace research laboratories of the Netherlands (NLR) and Germany (DLR). It is one of Europe's most advanced and specialized organization for wind tunnel testing. DNW manages eleven facilities located in five different sites across the Netherlands and Germany. It provides solutions for the experimental simulation needs of aerodynamic research and development projects. Among others, the combination of Through-Flow Nacelles and Turbofan Powered Simulators has become the standard testing technique for the testing of installation effects.

Figure 1.2: Large Low-speed Facility at DNW, Marknesse. Source: ESWIRP

The main objective of the engine/airframe integration tests is to assess the effect of the installed powerplant in the performance of the aircraft. To achieve this it is necessary to duplicate the external flow field through and around the engine as close as possible [16]. In overall it is important to achieve a thrust calculation accuracy level consistent with the model drag measurement.

This section introduces the testing technique carried out at DNW.

1.2.1. FLOW-THROUGH NACELLES

During many years flow-through nacelles was the standard technique used for the simulation of the engine [17]. Nowadays it is the simplest method for the evaluation of installation effects at a baseline (idle power) and for the simulation of the inlet flow. It provides the best compromise for the initial assessment and study of isolated and installed inlet spillage drag. The internal drag of the nacelle must be subtracted as it belongs to the thrust, in order to obtain the drag of the aircraft. This is commonly done through boundary layer calculations for the internal nacelle flow, or internal drag measurements in a static calibration facility.

The best geometry for the nacelle must be chosen according to steady inlet flow, good behavior at low and high angle of attack and minimum drag. A cross section of the flow-through nacelle compared with the Full Scale Turbofan is shown in Figure 1.3 a.

1.2.2. TURBOFAN POWERED SIMULATORS

Turbofan Powered Simulator (TPS) are scaled air motors developed to simulate the thrust characteristics of a conventional turbofan engines without the necessity of fuel, combustion or high temperatures, making them appropriate for wind tunnel testing [18]. Several sizes are available at DNW, from 4.2" to 10" fan diameter, in order to simulate engines at different bypass ratio [11]. The most common TPS consist of a single stage titanium fan having between 20 and 30 fan blades. The fan is driven by a shaft in a multi-stage turbine that is powered by externally supplied compressed dry air through the support pylon. Due to the expansion in the turbine, the core dry air is cooled down to -100 °C. As a result if the supplied air is not completely dry condensation could be initiated and the moisture could freeze generating ice that could affect the instrumentation and change the nozzle exhaust area. The supply airline was specifically designed to minimize the interference forces with a swan-neck concept with new materials [11]. In Figure 1.3 the left half shows the A380 model in asymmetric configuration (3 TPS and one flow-through nacelle) being tested at the Large Low-Speed Facility of DNW. The TPS is also compared with the full scale turbofan engine.

The function of the Turbofan Powered Simulators is to simulate at the same time both the inlet and exhaust flow in a realistic way in the wind tunnel. It is the only method for simulating coupling effects. As it duplicates the position of the engine streamflow, the flow around the air nacelles and pylons is reproduced. It can provide non uniform pressure profiles in a similar way as a real engine. The flow inside the streamtube is not relevant as far as it does not interfere with the mixing layer between the fan and external flow. In addition, the Fan Nozzle Pressure Ratio ($FNPR$) and the jet to freestream velocity are duplicated to ensure that the mixing process in the jet boundary is simulated due to Reynolds effects [12]. This is achieved by duplicat-

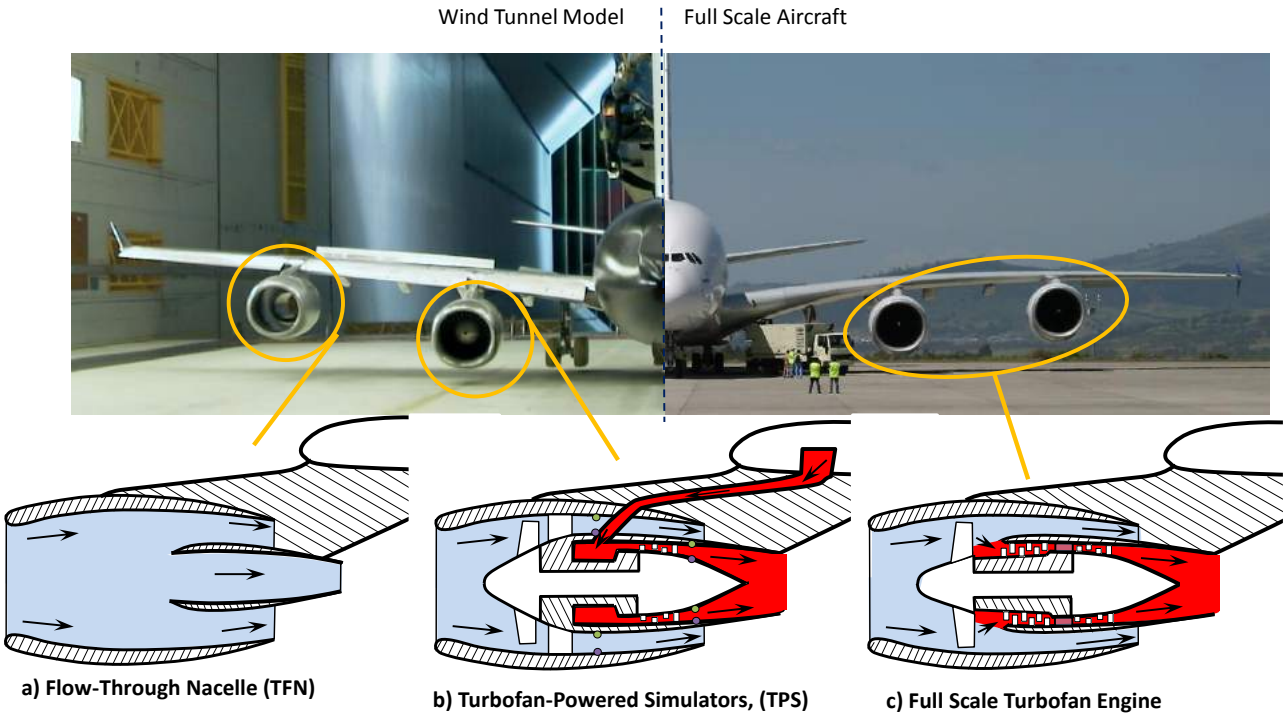

Figure 1.3: Cross section of Flow-Through Nacelle (a), Turbofan Powered Simulator unit (b) and full scale turbofan (c), and its location in the model. In red, the core flow. Left image, wind tunnel model in asymmetric configuration. Right image, full scale aircraft

ing the fan pressure ratio and the wind tunnel Mach number. Primary flow can be simulated with a realistic pressure but with a low temperature, which is not important for nowadays high bypass ratio engines due to its small contribution to the thrust and weak dependency of temperature to thrust. As the core air is supplied externally, the inlet mass flow contains only the mass flow of the fan. In comparison with the full scale aircraft, the inlet mass flow consists on the addition of the fan and core mass flow [16]. Then, for a correctly scaled fan nozzle and inlet, duplication of the fan mass flow in the TPS leads to an inlet mass flow which is too small by an amount of $\frac{1}{1+BPR}$ [16]. In terms of mass flow ratio, a lower mass flow ratio in comparison with the full scale is obtained by a factor of $\frac{BPR}{BPR+1}$ [12]. This would increase the negative pressures on the forebody of the nacelle [19]. To solve this problem the cowl forebody is usually modified by reducing the highlight diameter enough and by extending the inlet forward (to prevent excessive internal diffuser angles). As a result, the cowl forebody peak pressure and drag characteristics are similar to the actual engine cowl [16], [19]. The stagnation point on the inlet lip is restored. Extensive work is investigated by Laban and Soemarwoto [20]. To match the outer nacelle pressure distribution, the reduction in the highlight area is around 50% of the scaled mass flow reduction as a result of the missing core flow that no longer enters in the intake.

Instrumentation probes are placed both to monitor the health of the engine and to obtain the thermodynamic properties of the fan and core flow, as shown in Figure 1.3. For the first case, RPM pickups and thermocouples measuring the bearings temperature are installed. In order to determine the performance of the engine, at the fan and core duct entry (stations 17 and 7) several total and static pressure probes, as well as total temperature sensors are installed.

1.2.3. TPS CALIBRATION

The propulsive force that is generated as a result of the simulation of the external flow field is not a simulated parameter and a priory is not relevant [21]. However, the contribution of the net thrust of the TPS unit must be known and subtracted from the balance force in order to obtain the model drag. Accuracies in the gross thrust of 0.2% are necessary to obtain reliable data on engine installation drag due to interference effects [12].

The thrust cannot be determined from an isolated pylon/nacelle force measurement in the wind tunnel, as the external nacelle drag forces would contaminate the force balance data. As a result static calibration is necessary to obtain the internal TPS net thrust as a function of the operating Mach Number and the Fan Nozzle Pressure Ratio. Due to the lack of external flow the drag forces are eliminated.

ENGINE CALIBRATION FACILITY

At DNW, the Engine Calibration Facility (ECF) became operational in 1982 [22]. An overview of the installation can be shown in Figure 1.4. The TPS unit with the pylon is installed in the front end of a pressurized tank that can be evacuated to the required pressure for the simulation of the proper ram pressure ratio of the free flow (equivalent Mach number):

$$M_e = \sqrt{\frac{2}{(\gamma-1)}\left(\left(\frac{P_{t,0}}{P_{s,tank}}\right)^{\frac{\gamma-1}{\gamma}}-1\right)} \tag{1.3}$$

The inlet upstream stagnation pressure $P_{t,0}$ and nozzle exhaust static pressure $P_{s,tank}$ can be matched to the wind tunnel while maintaining quiescent conditions in the external flow [11]. A maximum equivalent Mach number of 0.92 can be obtained, with a minimum tank pressure of 0.58 bar.

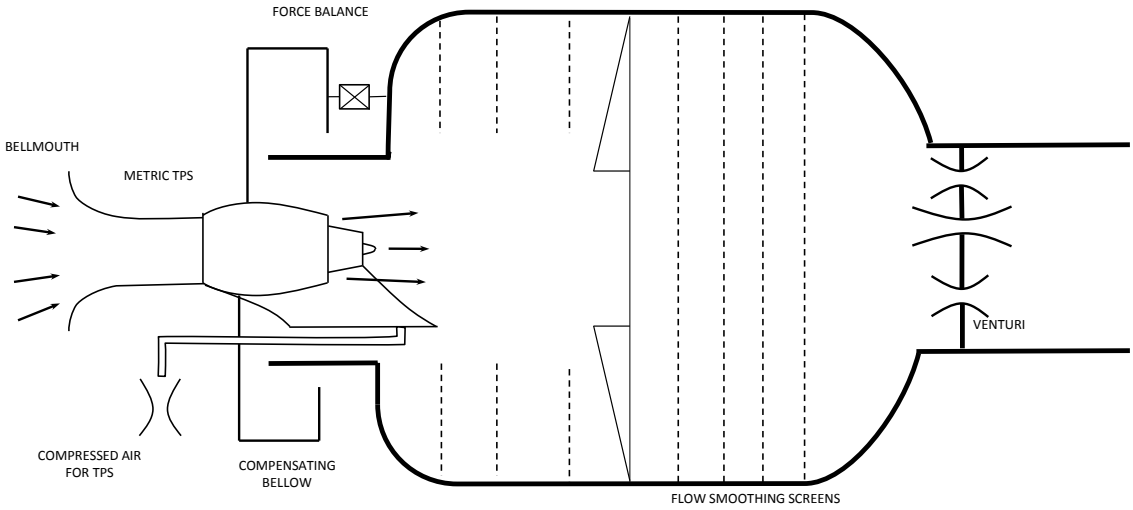

Figure 1.4: Engine Calibration Facility at DNW. Source: [11],[23],[10]

The complex assembly engine/tank consists of a flexible rubber seal that forms an airtight connection between the metric pylon/TPS, with its intake towards the environment, and the non-metric tank. Two compensating rubber seals are placed at upper and lower side of the central seal to compensate for the force due to the pressure difference. The engine turbine is powered through drive air supply line with three flexible air-coupling with two degrees of freedom to avoid interaction. A dedicated venturi is mounted in the supply line for measurement of the turbine mass flow.

A bellmouth is attached to the TPS inlet in order to measure the fan mass flow that is obtained from ambient conditions. These tank conditions are similar to the wind tunnel conditions, excepting the lack of ram drag. A break-up basket is placed 2.7 m downstream the TPS to destroy the jet momentum and to mix the warm fan air with the cold core flow. A set of four mesh screens are placed to further minimize recirculation, spread the downstream flowing air over the tank and provide uniform flow for the exhaust. However, recirculating air occurs due to the entrainment by the jet. This flow is spread by three annular mesh screens lowering the velocity near the exhaust

Downstream the tank a set of 9 venturis is placed with a sequence of areas following a binary code. For a given set of choked venturi conditions, the equivalent Mach number would strongly be influenced by the power settings. Increasing the required TPS mass flow would lead to an increase in the tank pressure, modifying the ram pressure ratio or equivalent Mach number, requiring for test data interpolations to fixed Mach numbers. DNW decided to operate the venturis at unchoked conditions in order to allow for enough mass flow to circulate the tank when the power settings of the TPS are changed, keeping constant the Mach number. Then, a venturi code is set at the desired maximum Mach number and expected total mass flow. As the fan mass flow is already measured with the bellmouth and the turbine mass flow with the dedicated venturi in the supply line, the venturis operate as a mass flow validation when the highest power conditions are achieved. In this approach equivalent Mach number is independent on RPM.

1.2.4. CURRENT THRUST/DRAG BOOKKEEPING

Due to the lack of inlet momentum or ram drag, the modified standard gross thrust is directly obtained in the calibration facility balance. This balance measurement is mainly biased by the bellmouth drag, the pressure difference over the mounting seals and the interference due to the turbine air supply.

$$F_{BAL,cal} = F^*_{G,ac} + F_{seal} + F_{BM} \tag{1.4}$$

In this equation $F^*_{G,ac}$ is the standard gross thrust. This includes the scrubbing and boattail drag as a result of the force generated by fan flow over the core cowling. The thrust angle with the nozzle axis ϕ is also taken into account.

The final objective of the calibration is the determination of the gross thrust and the inlet (fan) mass flow at any given Mach number, fan nozzle pressure ratio, fan pressure ratio and rotational speed. By measuring the flow total pressure and total temperature at the core and fan duct it is possible to relate the ideal with the real gross thrust through the velocity and discharge coefficients. By assuming that the external flow does not affect the thrust, the calibration coefficients are directly used in wind tunnel conditions to determine the net thrust from the monitored internal conditions at the TPS unit.

FAN DISCHARGE COEFFICIENT

The discharge coefficient is the ratio of the actual to ideal mass flow for a given nozzle geometry and nozzle pressure ratio. Hall [24] shows that the discharge coefficient reflects the deficit in the flow field due to the development of the boundary layer. The flow effective area is reduced by an amount equal to the displacement thickness δ^*. As a result it is equivalent to the ratio of the ideal or effective nozzle area required to pass the actual mass flow to the geometric nozzle area:

$$C_{D,fan} = \frac{\dot{m}_{fan_{ac}}}{\dot{m}_{fan_{id}}} = \frac{A_{id}}{A_{ac}} \tag{1.5}$$

For the fan discharge coefficient, the actual mass flow is obtained from the calibrated bellmouth according to its readings in pressure and temperature and the bellmouth discharge coefficient. The ideal mass flow is obtained by isentropic relations from the measured quantities at the fan duct (station 17):

$$\dot{m}_{fan_{id}} = \dot{m}_{19_{id}} = \frac{P_{t,17}A_{19}}{\sqrt{T_{t,7}}} FNPR^{\frac{-1}{\gamma}} \sqrt{\frac{2}{R}\frac{\gamma}{\gamma-1}\left(1 - FNPR^{\frac{1-\gamma}{\gamma}}\right)} \tag{1.6}$$

FAN VELOCITY COEFFICIENT

The velocity coefficient is the ratio of actual to ideal fan gross thrust considering in both cases the actual mass flow. If an ideal flexible convergent-divergent model is used, the velocity coefficient is defined as the ratio between an effective velocity $V_{19,eff}$ and ideal velocity $V_{9,id}$

$$C_{V,fan_{con-div}} = \frac{F_{G,fan_{ac}}}{C_{D,fan}\,\dot{m}_{fan_{id}}\,V_{fan_{id,con-div}}} \tag{1.7}$$

The actual modified standard fan gross thrust $F_{G_{ac}}$ is obtained by subtracting the core gross thrust to the actual gross thrust given by the balance.

$$F^*_{G,fan_{ac}} = F^*_{G_{ac}} - F_{G,core_{ac}} \tag{1.8}$$

The core gross thrust is obtained with the measured core mass flow and by assuming ideal expansion of the core velocity at the exit face.

$$F_{G,core_{ac}} = \dot{m}_{core_{ac}}\,V_{core_{id,con-div}} \tag{1.9}$$

APPLICATION TO WIND TUNNEL TESTS

Once these coefficients are determined in quiescent conditions, they can be applied to wind tunnel conditions assuming that the external flow does not affect the TPS thrust. Together with ideal conditions that are monitored in real time with the sensor probes within the TPS, the modified standard net thrust is obtained as a difference in momentum between the exhaust and the inlet:

$$F^*_{N,ac} = F^*_{G,fan} + F^*_{G,core} - F_{RAM,ac} = C_{D,fan}\,\dot{m}_{fan,id}\,C_{V,fan}\,V_{fan,id} + \dot{m}_{core,ac}\,V_{core,ac} - \dot{m}_{fan,ac}\,V_0 \tag{1.10}$$

For a given test campaign calibrations are repeated at least once, and calibration coefficient results are obtained with a repeatability better than 0.15% [22]. In addition the same probes must be used both in the calibration and in the wind tunnel tests [11]. Failed probes during the calibration are permanently removed from the data processing, and probes that fail in the wind tunnel are also removed from the wind tunnel and the calibration.

1.2.5. VALIDITY OF CURRENT ACCOUNTING

The assumption that the external flow does not affect the thrust determines the accuracy of the current testing technique. Differences between the static calibration and the wind tunnel test can strongly affect the Thrust Drag Bookkeeping method. Following previous work [2], [12], this effect may be present in engines with very high bypass ratio, and should be studied with more detail.

1.3. ENGINE/AIRFRAME INTEGRATION TESTS GLOBALLY

Due to its complexity and cost, engine/airframe integration tests have been carried out only in a few state of the art experimental facilities in Europe and USA [17]. This section focuses in the testing procedures taking place in other experimental facilities worldwide, and how they assessed the differences between static calibration and wind-on conditions due to the presence of external flow.

1.3.1. BOEING

Boeing was one of the first commercial aircraft manufacturers that used Turbofan Powered Simulators. Some of the testing insights at subsonic speeds are found in a paper by Decher of 1975 [25]. TPS units were calibrated in an engine calibration facility in a similar procedure as in DNW. The mass flow was also obtained by correlating inlet static pressure probes near the fan face (station 2) with calibrated mass flow from an installed short bellmouth. The average static inlet pressure ratio was used in wind-on conditions at low angles of attack.

After calibration isolated TPS tests were done to test the validity of thrust calculation procedure. A non metric flat plate was added near the exhaust of the engine simulating a wing to change the pressure distribution near the exhaust. In addition a blown nacelle was used to measure the effects of flow suppression in the fan flow by the freestream, from 0.3% to 0.5%.

1.3.2. DOUGLAS

Douglas used for first time TPS units for engine/airframe integration tests in 1970 to determine the installation effects of the DC-10, as it was described by Welge and Ongarato [19], [26]. The interaction of the overexpansion of the jet flow of the fan nozzle with the low pressure high velocity region under the wing was studied, as well as the influence of the external flow on the nozzle performance. Testing consisted in three phases: calibration of the engine in a test rig, isolated TPS test in presence of external flow and wing/ body/ pylon/ nacelle combination.

Static calibration was undertaken in a similar procedure as in DNW. Nozzle coefficients were recorded regarding Nozzle Pressure Ratio and RPM to account for flow swirl. In the isolated TPS testing the influence of the external flow on the fan discharge coefficient was assessed through the monitoring of the local static pressure at the nozzle exit plane. If different from the freestream static pressure, flow suppression (the reduction of mass flow due to higher local pressures at the nozzle exhaust) appeared. It was determined that the flow influences the thrust in unchoked conditions due to the increase in the local pressure at the nozzle exit plane and the contraction of the jet flow streamlines.

1.3.3. ARA

Aircraft Research Association (ARA) began testing TPS units in the UK with the commissioning of an engine calibration facility, the Mach Simulation Tank 1 (MST1) in 1979 [23]. Harris exhaustively describes in [7] and [5] the procedure undertaken for the testing.

TPS calibration is similar to the procedure carried out at DNW. Calibration data is processed according to ten different accounting methods allowing for the maximum information to be extracted. This multimethod approach maximize technical features of the calibration and minimize technical risks [5]. Isolated pylon/nacelle tests are done in wind-on conditions at low speed to determine the effect of the external flow in the engine performance. The net thrust is determined within 0.2% of accuracy at transonic conditions. Special test rigs are available to determine inlet and nozzle afterbody isolated performance performance [7]. Among other experiments it is possible to study low and high speeds the nozzle afterbody performance in order to determine the influence of the freestream on the nozzle discharge coefficient.

1.3.4. NASA

NASA has been using TPS as standard technique for engine/airframe integration testing since 1972, where a turbojet simulator for transonic speeds was manufactured and tested [27].

In 1976 Meleason and Wells [28] tested a model with four turbopowered engine simulators placed on the wing upper surface. The engine simulators were statically calibrated in the Douglas Facility. A plate that simulated the wing upper surface was attached to the nozzle and its contribution towards the drag was removed. Velocity coefficients were obtained for a range of local nozzle pressure ratios by measuring the static pressure in the nozzle exit.

In 1984 a Turbofan Powered Simulator was calibrated following a similar experimental setup as carried

out at DNW [29]. In this case, the possibility of flow suppression was investigated, due to the external flow effect in wind-on conditions which is not present during the static calibration test. Flow suppression would induce an error in the TPS thrust by reducing the effective mass flow rate. The difference between the static calibration and isolated TPS in wind-on conditions were considered negligible. Several parameters reflecting the turbomachinery performance were compared between calibration and wind tunnel to assure a consistent operation. Any discrepancy between both would require an adjustment in the operating settings.

One of the most recent engine/airframes integration experiments using TPS was carried out at NASA for the Hybrid Wing Body aircraft research in 2015 [30] as shown in Figure 1.5. The original TPS units developed by TDI to simulate the thrust of full scale turbofan engines were modified for the simulation of Ultra-High Bypass Ratio engines by increasing the fan and core nozzle area to match reference dynamic pressure and jet exhaust flow [18]. Once these modifications were validated, static calibration of the TPS was undertaken in a wind tunnel facility, in wind-off conditions. A bellmouth was attached to the inlet for the measurement of the mass flow, which was calibrated in CFD with StarCCM+. As a result of the calibration at different configurations the force and mass flow were obtained at any given RPM and fan pressure ratios.

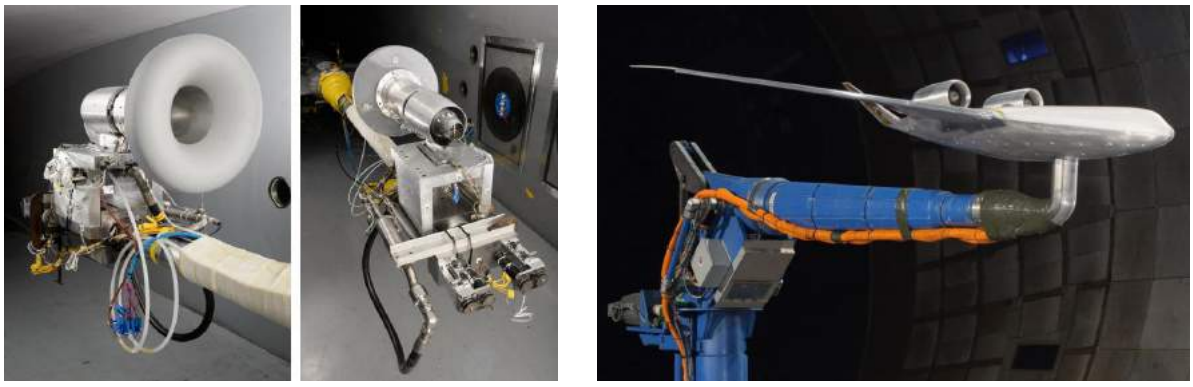

Figure 1.5: **a**: Static Calibration of TPS in the Wind Tunnel **b**: Hybrid Wing Body Wind Tunnel Model

1.3.5. ONERA

The ONERA calibration facility is different to the one present at DNW, ARA or Boeing. The nacelle is connected to the balance strut which supplies the core mass flow [31]. The fan mass flow is provided by a secondary piping which is joined to the TPS with a bellmouth. As a result, it allows for the independent control of:

- Upstream pressure of the fan $P_{t,0}$ by controlling the fan mass flow
- The TPS RPM by controlling the core mass flow
- The downstream pressure (exhaust) by adjusting a vacuum valve.

In addition the mass flow is directly measured and no bellows are required [16]. Laser speedometer and infrared measurements have been installed to investigate the flow at the nozzle exhaust during calibration.

However, two air supply systems (fan + core) are required so the total mass flow capacity has to be about four times larger for the same testing conditions as in DNW. The air supply capabilities limit the size of the TPS model.

1.3.6. CONCLUSIONS

Similarities have been found regarding the static calibration of the TPS unit at DNW with respect other international facilities. However, standard techniques taking place at NASA, Boeing and Douglas include the isolated testing of the TPS unit in wind-on conditions to determine to which extent the external flow modifies the thrust. This is not present in the current bookkeeping method as traditionally this effect has been considered low and insignificant. Nowadays, with the increase in bypass ratio, it may not be the case anymore. A modified testing approach at DNW, combining static and wind-on calibration, may be necessary.

1.4. RESEARCH QUESTIONS

This section establishes the Research Questions and introduces the outline of the next part of the report.

Based on the literature study [32] and the previously defined objectives, the research focuses on the assumption that the current TPS calibration results cannot be directly used in the wind tunnel tests. This is explained in the main hypothesis:

Hypothesis 1: *"The external flow affects the fan exhaust jet by changing the mass flow and the thrust of ultra-high bypass ratio turbofan engines operating in unchoked conditions with respect to quiescent conditions".*

To define the scope of the research the analysis focuses in the study of the TPS and TFN fan flow. The bypass flow is responsible of more than 80% of the thrust [33]. In addition the core flow is measured by the supply line and its behaviour is better understood.

In order to achieve these goals, the following research questions and sub-questions are formulated:

- What are the physical differences in the Turbofan Propulsion Simulator and Through-Flow-Nacelle fan exhaust between static calibration and wind tunnel (isolated and installed) conditions?
  - What is the origin (trigger) of these differences?
  - What is the physical interaction between the external and fan flow?
- How much do these physical differences affect the gross thrust, ram drag and net thrust at different power settings?
  - Under which conditions these differences are maximum?
  - How much do these differences compare with respect to the current instrumentation error?
- Which procedures can be improved or modified at DNW according to the identified limitations in order to increase the accuracy of engine/airframe integration tests of high bypass ratio turbofan engines?
  - What definition of thrust and drag is most appropriate to deal with the differences between calibration and wind tunnel conditions?
  - Which new instrumentation/measurement techniques should be introduced in order to improve the bookkeeping?
  - Can the use of computational tools improve the calibration and testing of Turbofan Powered Simulators at DNW?

This is a practical research aimed to follow the "diagnosis" and "design" steps of the intervention cycle. The first and seconds research questions focuses in the understanding and diagnosis of the present problem, which will lead towards the resolution of the first research goal. By properly analyzing the physical effects taking place in the testing is possible to determine and quantify the critical factors that are not properly represented in the current approach. This research question has its origin in the literature review [32], and will be further studied in the present report.

The third research question focuses on the design of an improvement based on the acquired knowledge and will lead towards the realization of the second goal. Once the limitations are understood the change of procedures can be preliminary assessed through experiments, computational or analytical tools. As TPS units are calibrated in static facilities for testing in the wind tunnel, to properly determine the effect of the external flow in engines with larger bypass is a must.

In order to answer the research questions, the limitations are introduced in Chapter 2 by assessing the differences between static calibration and wind tunnel conditions. This is followed by an alternative bookkeeping method that deal with the identified limitations. Chapter 3 details the mathematical model and quantifies difference in thrust due to these limitations with respect to the standard error introduced in the experimental approach. Chapters 4 and 5 provides an analysis through numerical methods of the exhaust of the propulsive units, that is validated through an experimental approach in Chapters 6 and 7. Finally Chapter 8 gathers the theoretical, numerical and experimental results and provides recommendations with respect to the best approach to bookkeep the thrust and drag at DNW.

2

METHODOLOGY

In this chapter limitations of the current approach are introduced by means of a theoretical analysis. First, in Sections 2.1 and 2.2 the units of study, a 6" Turbofan Power Simulator (TPS) and Ultra-High Bypass Ratio Through-flow-Nacelle are introduced. A theoretical study outlying the differences between calibration and wind tunnel conditions is established in Section 2.3, that will lead towards the identified limitations in Section 2.4. These are tackled by the introduction of a modified thrust/drag bookkeeping method in Section 2.5.

2.1. VERY-HIGH BYPASS RATIO TURBOFAN POWERED SIMULATOR

The chosen unit of study is a 6 inches Turbofan Powered Simulator (TPS) owned by DNW. The nacelle and pylon was designed by one of DNW's costumers. It represents a last generation Very High Bypass Ratio turbofan engine. The unit has been calibrated in the Engine Calibration Facility in 2015 and tested later that year in the Wind Tunnel. Figure 2.1 shows the main geometry and components of the studied TPS, together with its relative location within the wind tunnel model.

Confidential
Figure

Figure 2.1: 3D representation in CATIA of studied TPS. Source: *DNW internal Documentation, 2015*

2.1.1. PERFORMANCE MAP

From the calibration the performance characteristics of the unit are obtained. These are represented as a function of the Mach number (obtained by a difference in ram pressure in the Engine Calibration Facility) and the TPS power conditions, represented by the Fan Nozzle Pressure Ratio. Important performance parameters are:

- **Fan Pressure Ratio,** FPR: it is defined as the ratio between the fan duct total pressure $P_{t,13}$, equivalent to the fan nozzle entry station $P_{t,17}$ (currently measured in the TPS) and the engine intake $P_{t,2}$. It is an indicator of the work generated by the fan in compressing the bypass air. The Fan Pressure Ratio is usually used when attention is given to the fan performance. Mostly the TPS unit is calibrated by performing a FPR sweep (always from 1 to 1.42) at a given equivalent Mach number.
- **Corrected Fan Revolutions Per Minute,** RPM_{ISA}: The fan revolutions per minute corrected for International Standard Atmosphere (ISA) conditions are measured in the TPS. This was traditionally used for the bookkeeping of the TPS thrust and mass flow, but was later disregarded when it was possible to obtain online measurements of the Fan Nozzle Pressure Ratio (FNPR). Both are proportional to each other, as shown in Figure 2.2 b.
- **Fan Nozzle Pressure Ratio,** $FNPR$: following the definition used at DNW it is the ratio between the total pressure at the inlet fan duct, $P_{t,17}$ and the freestream static pressure, $P_{s,00}$ It is an indicator of the work generated by the fan nozzle in expanding the bypass air. It is the parameter of interest when bookkeeping exhaust systems. The total pressure at the inlet fan duct is obtained by means of the averaging of several total pressure probes at station 17.
- **Dimensionless Fan Mass Flow Rate,** $\dot{m}_{fan,NONDIM}$: the ratio between the TPS fan mass flow $\dot{m}_{fan}$ to the mass flow obtained at sonic conditions, $\dot{m}^*_{fan}$. It is proportional to the thrust of the propulsive unit and independent of the freestream conditions
- **Dimensionless Core Mass Flow Rate,** $\dot{m}_{core,NONDIM}$: the ratio between the TPS core mass flow, which is supplied externally at high pressure, and the mass flow obtained at sonic conditions, $\dot{m}^*_{core}$. It represents the required power of the propulsive unit.
- **Fan Total Temperature Ratio,** $\frac{T_{t,fan}}{T_{t,0}}$, used to compute the TPS fan performance.
- **Core Total Temperature Ratio,** $\frac{T_{t,core}}{T_{t,mat}}$, used to compute the TPS core performance.
- **Fan Discharge and Velocity Coefficients,** $C_{D,fan}$ **and** $C_{V,fan}$, obtained as a result of the calibration process.

In the wind tunnel the TPS exhaust Mach number M_{19} is important characteristic that is reproduced in order to simulate interference effects. This is proportional to the Fan Nozzle Pressure Ratio [16]. Following the scope of study, focusing on exhaust interference effects, the FNPR is chosen as an independent parameter to represent the power conditions in addition of the freestream Mach number, M_0. The previous parameters are represented from the calibration results in Figure 2.2. This performance is the basis over which the analysis is performed.

Also, as shown in Figure 2.2 a there is a direct relation between the Fan Pressure Ratio and the Fan Nozzle Pressure Ratio

$$FNPR = \frac{P_{t,17}}{P_{s,00}} = FPR\frac{P_{t,13}}{P_{s,00}} \tag{2.1}$$

As the bypass ratio is increased, by keeping constant the thrust, the acceleration of the core air must decrease, reducing the fan pressure ratio. As a result there is an inverse relation between the bypass ratio and the fan pressure ratio. Following equation 2.1 fan nozzle pressure ratio is also decreased as the bypass ratio increases.

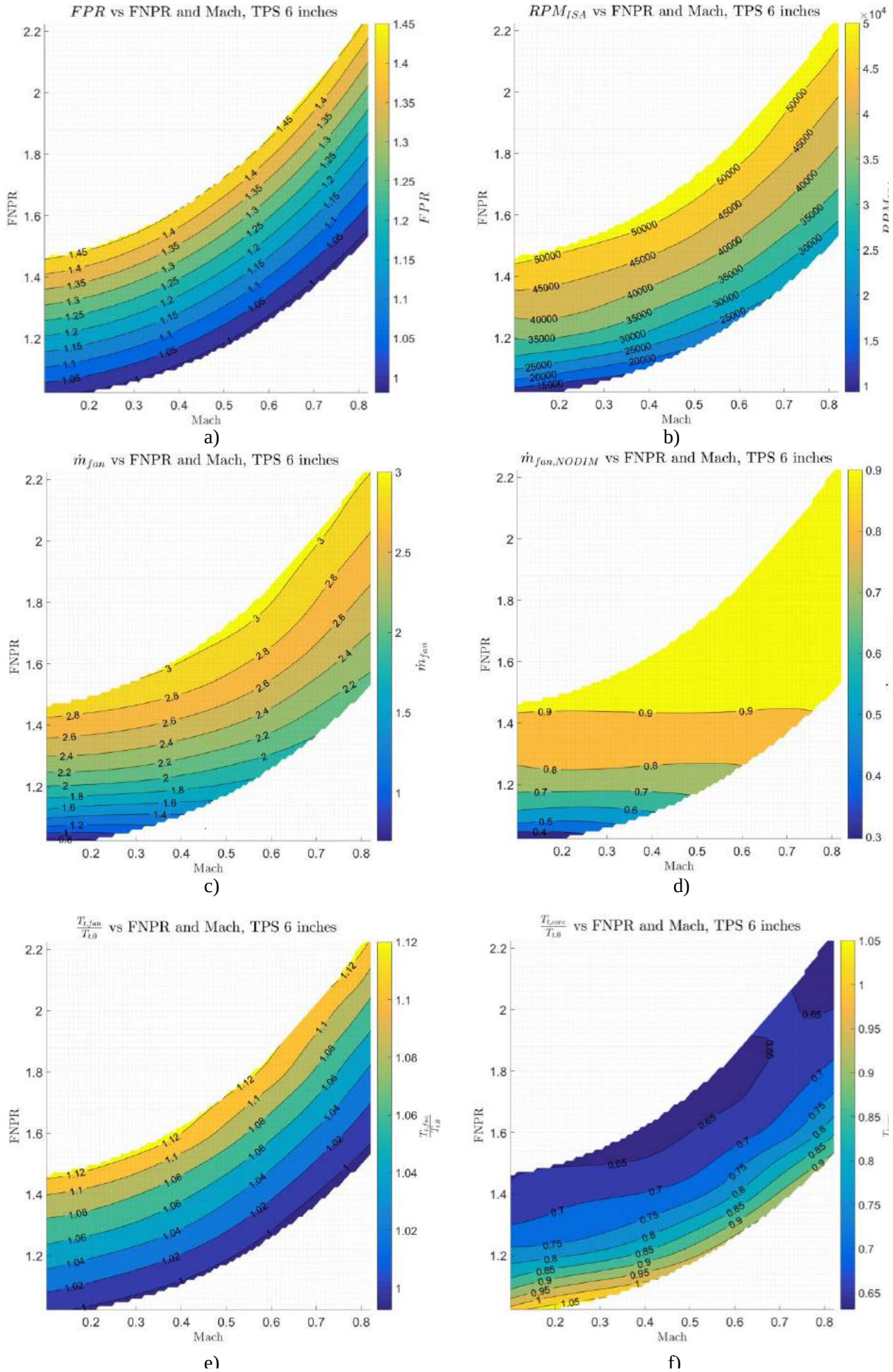

Figure 2.2: TPS Performance Map as a function of the freestream Mach number and Fan Nozzle Pressure Ratio. a: Fan Pressure Ratio b: ISA corrected Revolutions per Minute. c: ISA corrected fan mass flow d: Dimensionless fan mass flow e: Fan temperature ratio f: Core temperature ratio. Source: *DNW internal Documentation, Calibration Test Data, 2015*

2.1.2. COMPARISON WITH WIND TUNNEL

The comparison of the TPS performance between wind tunnel tests and static calibration is important to assure a consistent operation [29]. Any discrepancy between both would require an adjustment in order to account for a correct thrust calculation in the wind tunnel, at a given Mach number. Both in the wind tunnel and the calibration power sweeps (FPR 1 to FPR 1.4) are performed at Mach numbers of 0.4, 0.6, 0.78 and 0.82.

DIFFERENCE IN TPS PERFORMANCE

Figure 2.4 shows the ratio of the fan mass flow to the core mass flow for both calibration and wind tunnel. The wind tunnel requires a higher core mass flow for the same output (fan mass flow) than the calibration.

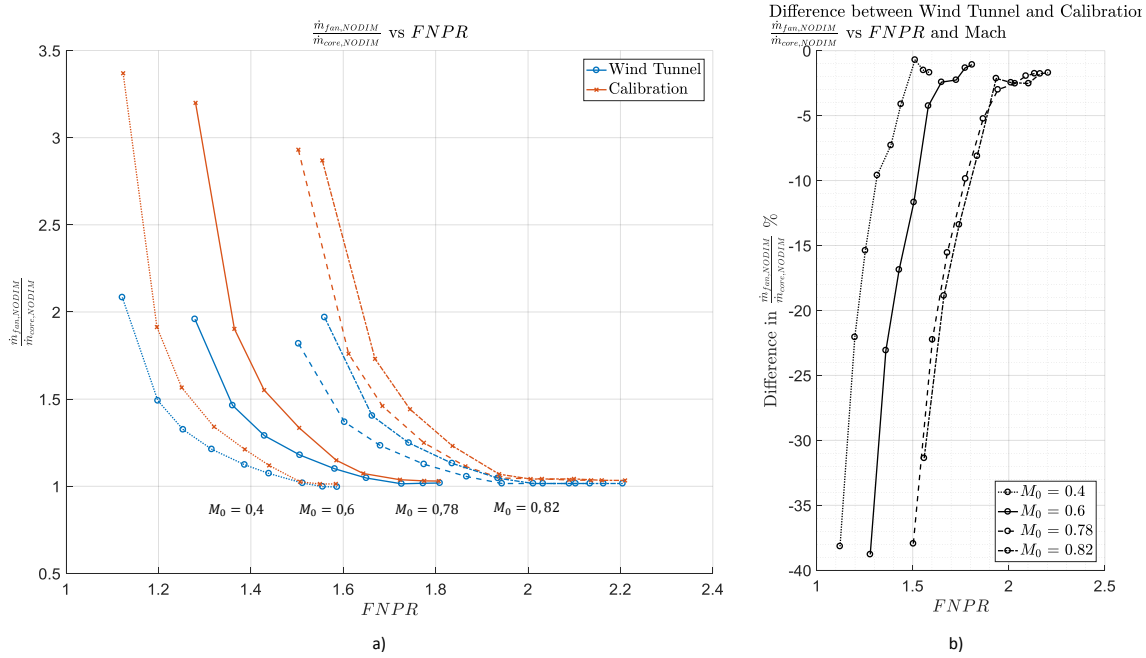

Figure 2.3: a: Ratio between the fan mass flow to the core mass flow at different Mach numbers for Calibration and Wind Tunnel Conditions b: Percentage difference in the ratio fan to core mass flow between Calibration and Wind Tunnel. Source: *DNW internal Documentation, Calibration Test Data, 2015*

Figure 2.4 shows differences in the RPM for a given conditions at the exhausts (same FNPR). RPM are slightly higher in the calibration.

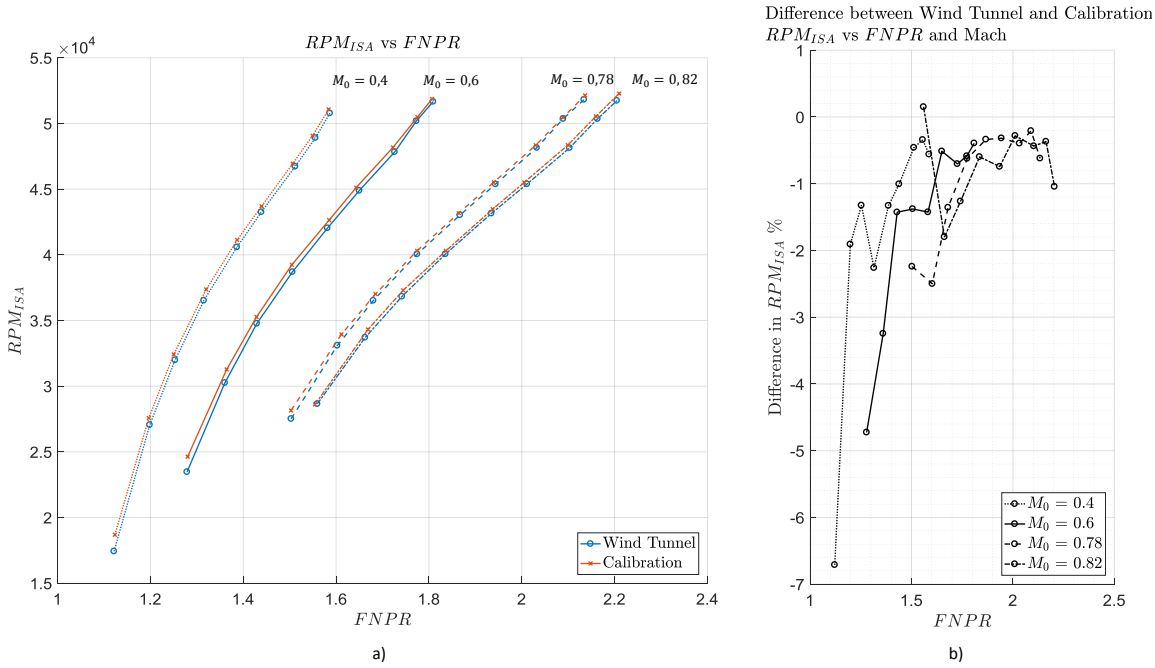

Figure 2.4: a: RPM_{ISA} vs $FNPR$ at different Mach numbers for Calibration and Wind Tunnel Conditions b: Percentage difference in RPM_{ISA} between Calibration and Wind Tunnel. Source: *DNW internal Documentation, Calibration Test Data, 2015*

These differences are higher at low power conditions, and decrease when chocked conditions are achieved at the exhaust of the fan. They are an indicator that the external flow (wind tunnel) affects the TPS performance with respect to calibration conditions.

DISTORTION

The distortion at a given section is defined as the local pressure difference with respect to the average one. Distortion patterns of the fan nozzle plane can be obtained with the total pressure rakes present at station 17. The distortion ratio is defined as:

$$DC = \frac{P_{t,i} - P_{t,avg}}{P_{t,avg}} \tag{2.2}$$

It is possible to compare the distortion patterns between wind tunnel and calibration, at different power settings. This is a standard process at DNW to identify defects in the measurement probes. It is also useful to highlight 3D effects.

Figure 2.5 show similarities in the distortion patterns at the fan and core nozzle between the wind tunnel and calibration. The analysis is done at Mach 0.78 for low, medium and high power settings. Based on this, it can be concluded that differences between static and wind on lie in the TPS performance rather than in the distortion pattern.

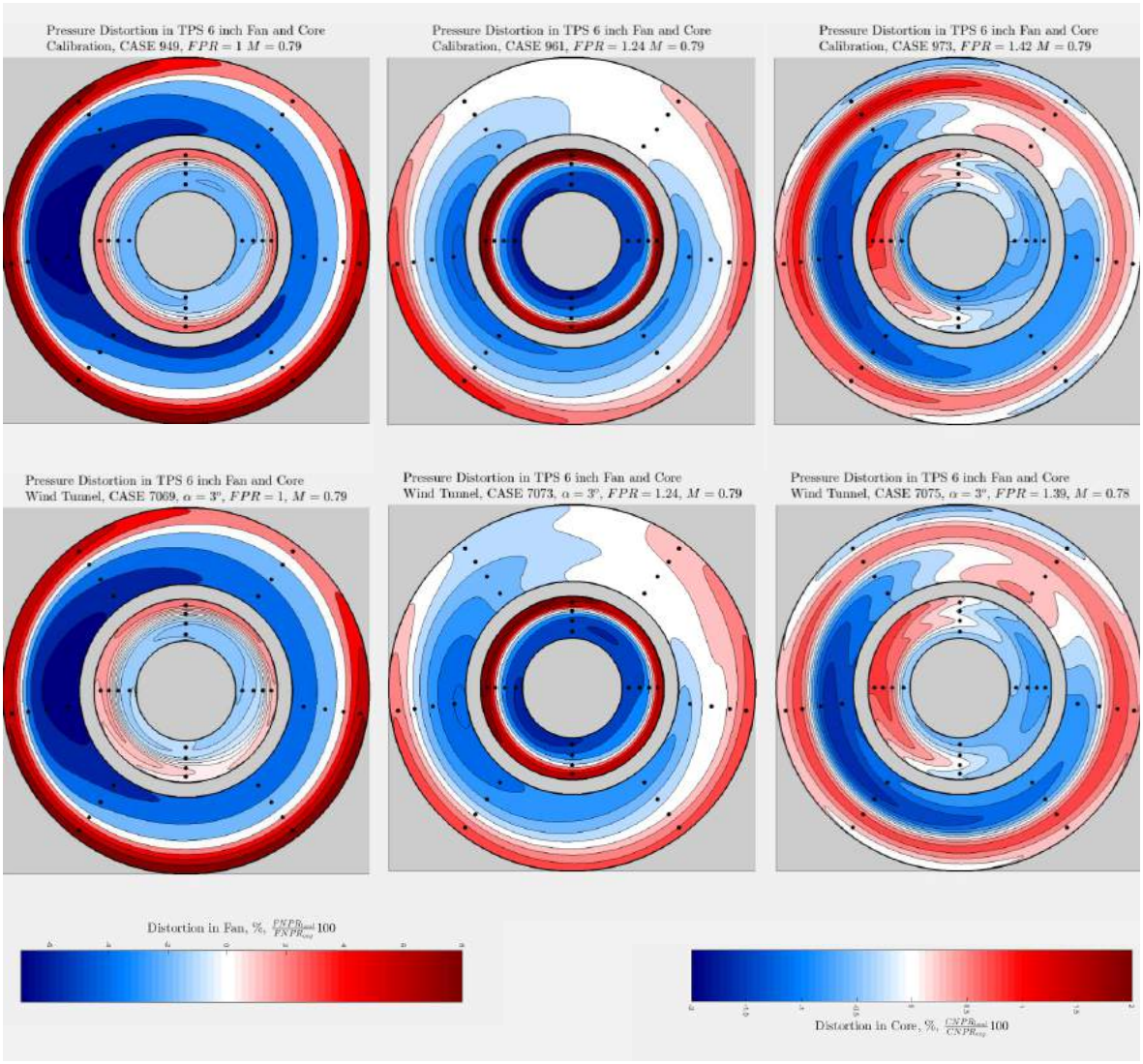

Figure 2.5: Distortion Patterns, M_0 = 0.79. Upper row: Calibration conditions. Lower row: Wind Tunnel conditions. Columns from left to right: FPR = 1 (Idle), FPR = 1.24 (medium power settings), FPR = 1.42 (high power settings). Source: *DNW internal Documentation, Calibration Test Data, 2015*

2.2. ULTRA-HIGH BYPASS RATIO THROUGH-FLOW NACELLE

The Ultra-High Bypass Ratio Through-Flow Nacelle (CRUF-TFN) is an engine nacelle model with an internal diameter of 10", as shown in Figure 2.6. It was manufactured and owned by DLR in 1994 [34] for the study of the jet drag interference effects on the ALVAST half model, in relation to the European Research Programmes DUPRIN and ENIFAIR [14].

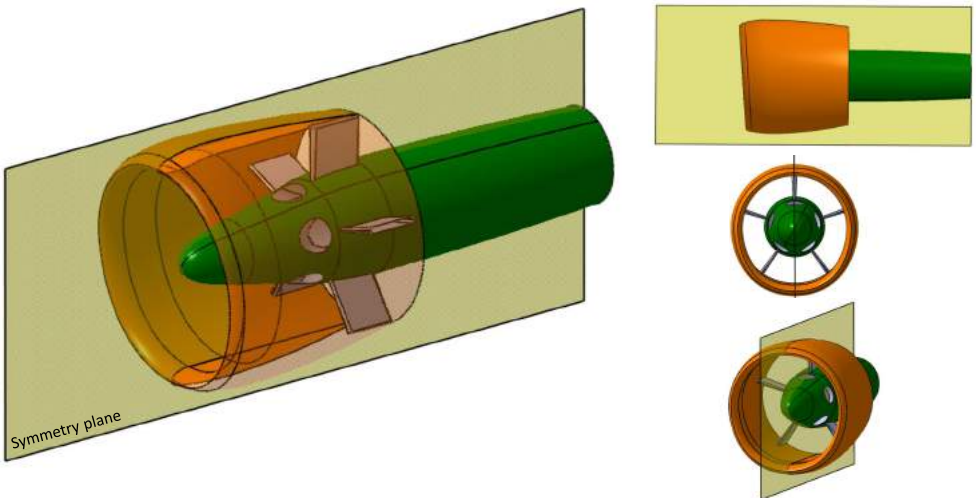

Figure 2.6: 3D views of studied CRUF Through-Flow Nacelle unit

The unit is selected because of the availability of calibration data, the possibility of testing in isolation at the German-Dutch Wind Tunnels and because its external representation of the next generation of turbofan engines.

As shown in Figure 2.6, a through flow core in enclosed in the nacelle with five inlet openings on its nose fairing. The core nozzle (station 603) is equipped with total pressure rakes and the fan nozzle (station 275) and intake duct (station 97) are equipped with static pressure taps. For the study of the fan flow, the openings in the nose fairing and the core exhaust are sealed. As a result the through flow nacelle mass flow is only the one of the fan.

2.2.1. PERFORMANCE

The Through-Flow Nacelle represents the idle conditions of the TPS. For simplification it can be analyzed as a convergent nozzle. The Fan Nozzle Pressure Ratio (FNPR) is proportional to the wind tunnel freestream flow by assuming that no total pressure losses occur in the nozzle, $P_{t,7} = P_{t,tunnel}$:

$$FNPR^{TFN} = \frac{P_{t,tunnel}}{P_{s,tunnel}} = \left(1 + \frac{\gamma - 1}{2} M_0^2\right)^{\frac{\gamma}{\gamma-1}} \tag{2.3}$$

Following this approach ideally the exhaust velocity M_{19} is equal to the freestream Mach, M_0. Losses in the fan are bookkept by means of the discharge and velocity coefficient [35] that are obtained through calibration.

2.2.2. CALIBRATION

The Through-Flow nacelle mass flow and (negative) thrust was measured in 1994 under quiescent conditions in the Engine Calibration Facility (ECF) at simulated Mach numbers $M_0 = 0.18, 0.27, 0.34$ and 0.45 [35]. The calibration process is similar as the one used for TPS. The simulated wind tunnel conditions without external flow were possible due to the pressure difference between the ECF tank (by means of suction compressors) and ambient.

The intake discharge coefficient can be obtained according to the actual mass flow, $\dot{m_{F,ac}}$ and the ideal mass flow obtained through the static pressure sensors at the intake, $\dot{m}_{I,id}$:

$$C_{D,I} = \frac{\dot{m_{F,ac}}}{\dot{m}_{I,id}} \tag{2.4}$$

The fan nozzle discharge coefficient is obtained according to the actual mass flow $\dot{m_{F,ac}}$ and the ideal mass flow obtained through the static pressure sensors at the fan exhaust, $\dot{m}_{I,id}$. In this case the core is sealed.

$$C_{D,F} = \frac{\dot{m_{F,ac}}}{\dot{m}_{F,id}} \tag{2.5}$$

The fan negative thrust or internal drag is represented by the velocity coefficient:

$$C_{V,F} = \frac{T_F}{\dot{m}_{F,id}\, V_0\, C_{D,F}} \tag{2.6}$$

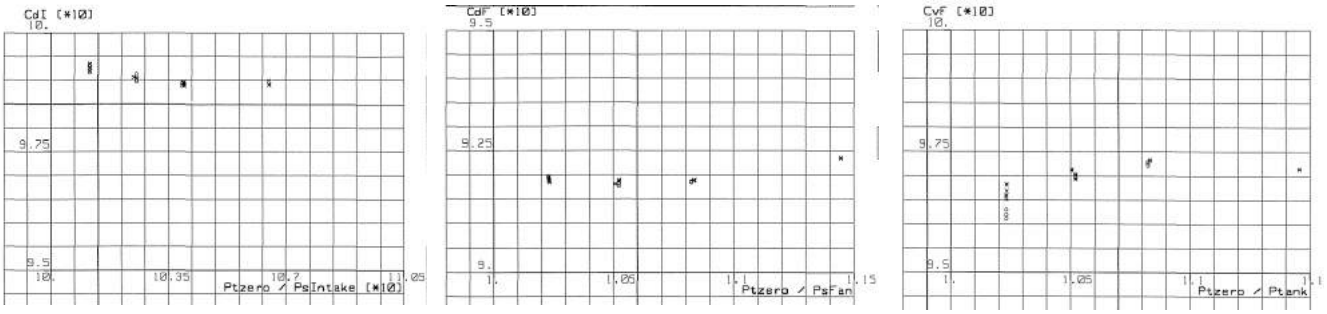

a b c

Figure 2.7: Discharge and Velocity Coefficients of the TFN obtained in static calibration, [35]

2.3. DIFFERENCES BETWEEN CALIBRATION AND WIND TUNNEL

Turbofan Powered Simulators and Through Flow Nacelles are calibrated in quiescent air in order to determine the internal losses in mass flow and gross thrust. However, Section 2.1.2 has shown a differences in the TPS performance between calibration and wind tunnel, especially for the unchocked nozzle. This is the first indicator that the external flow affects the local conditions at the exhaust. These changes are not captured by the internal instrumentation of the TPS fan and core nozzle, and could lead towards an incorrect measurement of thrust.

This section theoretically introduces the physical differences that will be studied with more detail in the numerical and experimental approach.

2.3.1. PRESENCE OF EXTERNAL FLOW

The presence of external flow itself can be enough to modify the pressure field at the exhaust nozzle. Two main reasons are identified:

DIFFERENCE IN JET ENTRAINTMENT

The difference in flow entraintment and spreading rate can change the pressure field in the exhaust. The dividing streamline between internal and external flow is modified, and the flow can generate a different exhaust momentum.

In 2005, Rossow and von Geyr [2] investigated the influence of external flow in the gross thrust to underline the limitations of the thrust drag bookkeeping. A CFD study of the isolated and installed TPS was performed and discussed the dependency of the jet development on the external flow. The higher fan spreading rate at lower Mach numbers increased the displacement effect altering the recompression of the flow at the nacelle trailing edge. This was an indicator of the influence of the external flow on the gross thrust. However, differences were qualitative and not quantitative, and the quiescent condition ($M_0 = 0$) was not evaluated. A detailed study of the exhaust flow is necessary by comparing quiescent with freestream conditions.

DIFFERENCE IN NACELLE PRESSURE FIELD

The development of the pressure field along the external nacelle in the wind tunnel is different with respect to the static calibration. With external flow pressures can be developed near the nacelle trailing edge which are different from the freestream pressure. This local pressure has an influence on the pressure in the exhaust plane.

2.3.2. PRESENCE OF WING

The pressure field of the wing can affect the conditions at the fan exhaust. The current location of the turbofan engines in commercial aircraft is under the wing, with the exhaust close the wing leading edge vertical plane [36] as shown in Figure 2.8 a.This is the region where higher than freestream pressures are developed at moderate angles of attack such as climb or cruise due to the deceleration of the flow in the airfoil lower surface.

Figure 2.8 a shows the pressure coefficient field of a representative supercritical airfoil for modern commercial aircraft at an angle of attack of 3 degrees at M = 0.22, obtained by the author by means of RANS-SST. In the region of the Fan exhaust an average pressure coefficient of 0.17 is obtained at an angle of attack of 3°. The analysis is extended at different angles of attack in Figure 2.8 b. As expected, the positive loading in the lower surface is increased with the angle of attack.

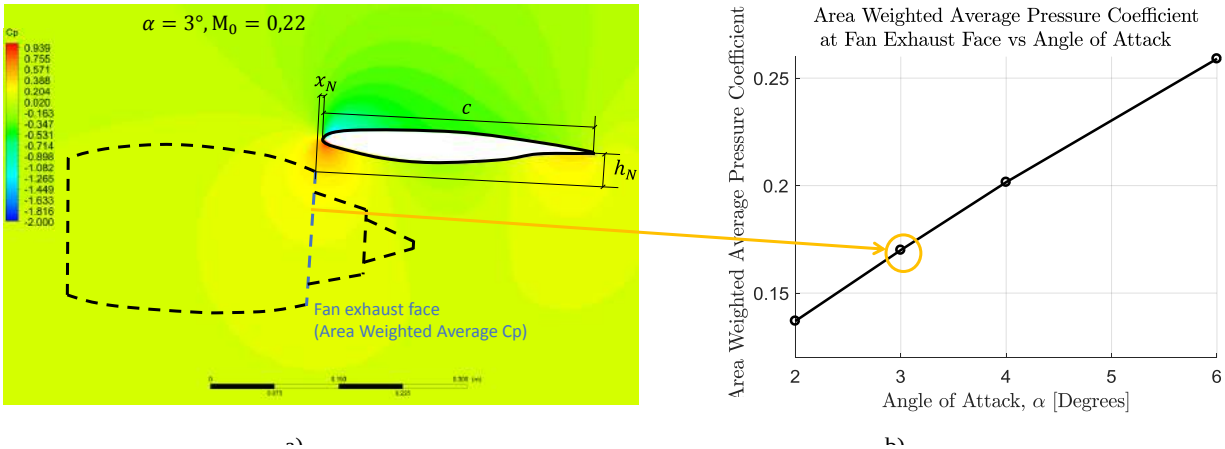

Figure 2.8: a: Pressure Coefficient field on supercritical airfoil at $M_0 = 0.3$. In dotted line, theoretical location of the engine b: Area weighted average Cp at location of fan exhaust plane

2.4. IDENTIFIED LIMITATIONS

In the Literature Review [32] several limitations have been detected that will influence the current testing approach. Among others, the most important one concerns the influence of the external flow in the static calibrated thrust. This effect has been a concern to wind tunnel specialists for more than thirty years [29]. However, only recently it is starting to represent a real problem in the accuracy of the engine/airframe integration tests.

Traditionally, High Bypass Ratio (5-6) Turbofans operate at choked conditions during cruise conditions [4]. Also Very-High Bypass Ratio Turbofan (11-13) operate with the nozzle chocked at Mach numbers higher than 0.75. In this situations the external flow has no influence in the engine thrust. However, Ultra-High Bypass Ratio Turbofans can operate their full range at unchoked conditions. In this case information can travel upstream, and the shape of the jet boundary is expected to change between static and wind on conditions. The previous section has shown a difference between the constant static pressure profile around the TPS in quiescent conditions, and the variable static pressure profile at the nozzle exit plane in presence of the wing and the external flow.

2.4.1. FLOW SUPPRESSION

The thrust drag bookkeeping method assumes perfect expansion from the nozzle to ambient conditions in the nozzle exit plane. Wolf [12] explains that discharge and velocity coefficients are defined in function of the Freestream Nozzle Pressure Ratio, or Nozzle Exhaust Pressure Ratio: $\frac{P_{t,7}}{P_{s,00}}$. However, the external flow influenced by the underwing pressures and the pylon can lead to flow suppression, which is the decrease of the nozzle mass flow rate and the increase in the exit static pressure downstream the nozzle (due to boattail), leading to a reduced local nozzle pressure ratios $\frac{P_{t,7}}{P_{s,e}}$, as shown in Figure 2.9.

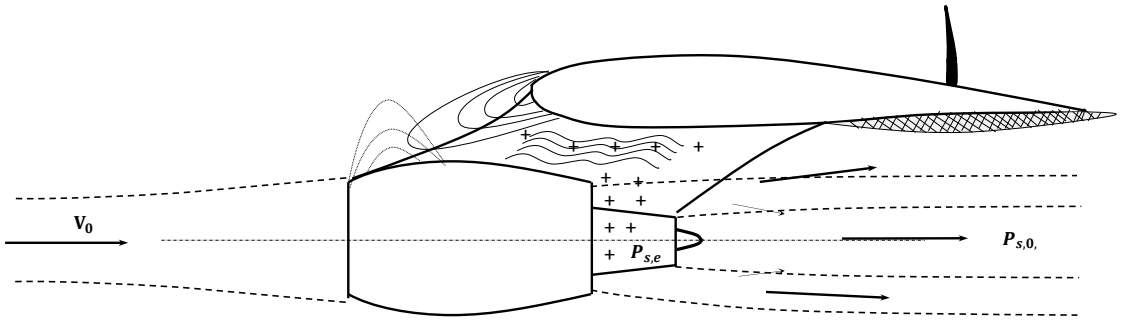

Figure 2.9: Presence of higher than freestream pressures in the fan exhaust plane

This effect is more severe at lower nozzle pressure ratios, typical for engines with higher bypass such as Very-High and Ultra-High Bypass Ratio turbofans. According to Wolf the effect of suppression diminishes as the flight speed increases and the ram pressure ratio builds up.

In relation with this phenomena, in 2005 Rossow and von Geyr [2] discussed that the post-exit force, due to the incomplete expansion of the flow at the nozzle exit plane, was not properly bookkept in the determination of the nozzle coefficients, and should be corrected for.

Following the conclusions of MIDAP [8], "the effects of external flow on nozzle flow capacity and internal thrust are important". The problem is that the nozzle gross thrust $F_{G,9}$ can not be evaluated in flight conditions (in the wind tunnel in our case). As a result, the calibrated discharge coefficient must be modified for external flow suppression due to the presence of the pressure area term in the case of unchoked conditions (lower nozzle mass flow rate and the decreased nozzle pressure ratio [16], [12]).

2.4.2. BOOKKEEPING OF SCRUBBING AND BOATTAIL DRAG

Scrubbing and boattail drag is the friction and pressure drag respectively, originated by the exhaust of the fan flow scrubbing on the core cowling and part of the pylon, and by the exhaust of the primary flow scrubbing on the external plug, as shown in Figure 2.10. It is typical of short duct turbofan nacelles and must be bookkept, according to Covert [37] and to Wolf [16], to the engine gross thrust. This is because in the engine calibration facility the gross thrust is measured already including the drag on external surfaces that is immersed in the fan and core exhaust, including the pylon. Then, the core and fan scrubbing drags are already included in the velocity coefficient.

According to Obert [38] the boattail of a nacelle indicates how tapered is the geometry of the fan and core cowl towards the exhaust nozzle [37].

The afterbody datum condition is also defined by Covert [37] as nozzle base drag, and any variation from that is called as boattail drag. Boattail drag is a throat-dependent force. The plume shape changes according to the nozzle mass flow and nozzle pressure ratio, mixing with the external flow and strongly influencing upstream conditions. As a result of the external flow over the cowling afterbody an adverse pressure gradient is generated at the nozzle/plume junction. This pressure gradient is further increased due to the expansion of the supercritical flow. Then, at the nozzle exhaust plane the boundary layer displacement increases, leading to separation in case of large boattail angles of a strong shockwave at the nozzle/plume junction [37]. This separation further increases the drag.

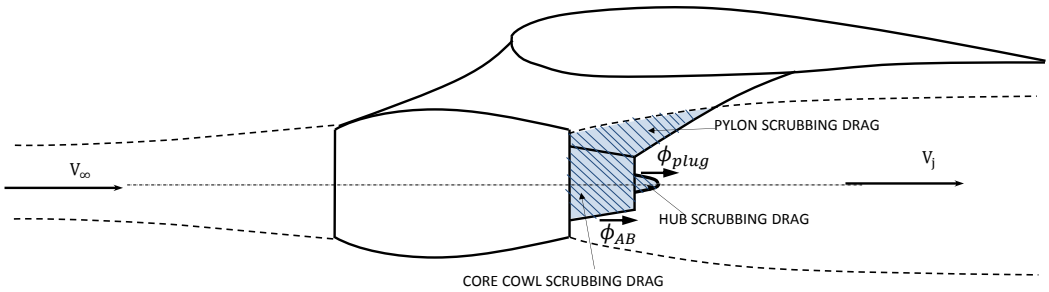

Figure 2.10: Scrubbing drag on core cow, plug and pylon

Following the guidelines of the MIDAP group [8], any forces inside the streamtube should be bookkept as thrust. Then, the afterbody ϕ_{AB} and plug ϕ_{plug} forces caused by the propulsive streams of the fan and core, should not be isolated as they are part of the gross thrust definition. However, in presence of external flow, these may change in comparison with the static testing calibration. According to the conclusions of MIDAP [8] there is an "intimate connection in the presence of external flow between D_{AB}, D_{plug}, D_{cowl} and internal flow". The current bookkeeping does not take into account the change in boattail and scrubbing drag due to the wing pressure field and external flow. This is incorrectly calibrated as a difference in drag (instead of in thrust) and should be corrected for.

2.5. MODIFIED THRUST/DRAG BOOKKEEPING

The definition of the thrust and drag is central for the aircraft performance estimation and posterior verification and evaluation of wind tunnel and flight test data [8]. In the following section a consistent and standardized structure of definitions for the different components of the thrust and the drag will be given, to deal with the presented limitations.

For simplification, the analysis is introduced for a single stream nacelle. These definitions are based on three sources: the conclusions of the Ministry-Industry Drag Analysis Panel (MIDAP) Study Group gathered in AGARD-AG-273 Technical Publication [8], the Aeronautical Research Council (ARC) in the United Kingdom [39], [40], [41] and the Society of Automotive Engineers (SAE) [42]. The Literature Study [32] offers a wide explanation of the thrust/drag bookkeeping method for dual separate flow.

2.5.1. NET GAUGE THRUST

Applying Newton's Second Law of Motion to a streamtube as shown in Figure 2.11, the total force on the fluid must be equal to the time rate change of linear momentum.

$$P_{s,1}\,A_1 + \int_{S_{tube}} P_s\,\mathrm{d}A - P_{s,2}\,A_2 = \dot{m}_2\,V_2 - \dot{m}_1\,V_1 \Rightarrow \int_{S_{tube}} P_s = \left(\dot{m}_2\,V_2 + P_{s,2}\,A_2\right) - \left(P_{s,1}\,A_1 + \dot{m}_1\,V_1\right) \tag{2.7}$$

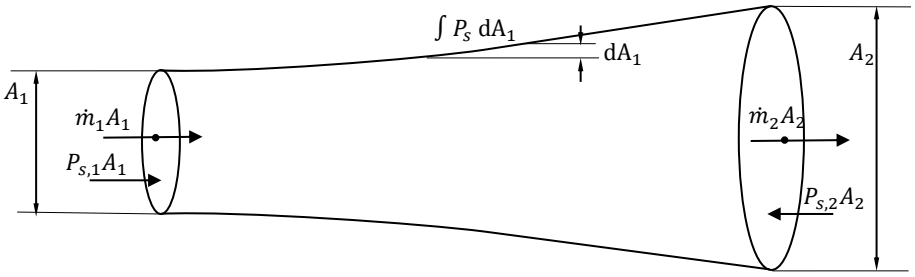

Figure 2.11: Forces acting on the defined domain. Source: *MIDAP Study Group* [8]

The gauge stream force F_G is defined as the absolute stream force relative to ambient conditions:

$$F_G = \dot{m}\,V + \left(P_s - P_{s,0}\right)A \tag{2.8}$$

Then, the gauge stream force in the streamtube is:

$$\int_{S_{tube}} \left(P_s - P_{s,0}\right)\mathrm{d}A = F_{G_2} - F_{G_1} \tag{2.9}$$

The term $F_{G2} - F_{G1}$ is defined the as "Net Gauge Thrust", the change in stream force between stations 1 and 2 which is equal to the rearward axial force on the streamtube. This definition can substitute to the alternative concept of the integral pressure times the area plus viscous effects. Both reference stations must be upstream infinity and downstream infinity to avoid potential buoyancy forces.

2.5.2. DOMAIN DEFINITION

The analysis is done on a stationary ducted body on steady stream of infinity extent aligned with the airflow. The resultant force can be obtained according to the change of the fluid momentum contained within an arbitrary surface surrounding the body [39]. The reference stations are chosen infinitely upstream 0 and downstream 00 of the ducted body (engine nacelle). In this situation, the domain can be different in three zones as shown in Figure 2.12:

- Pre-entry Streamtube: the streamtube extending from infinity upstream of the body, 0, to the nacelle entry 1. Its boundaries separate the internal from the external flow.
- Ducted body: determined by the physical boundary of the engine nacelle 1 to 9.

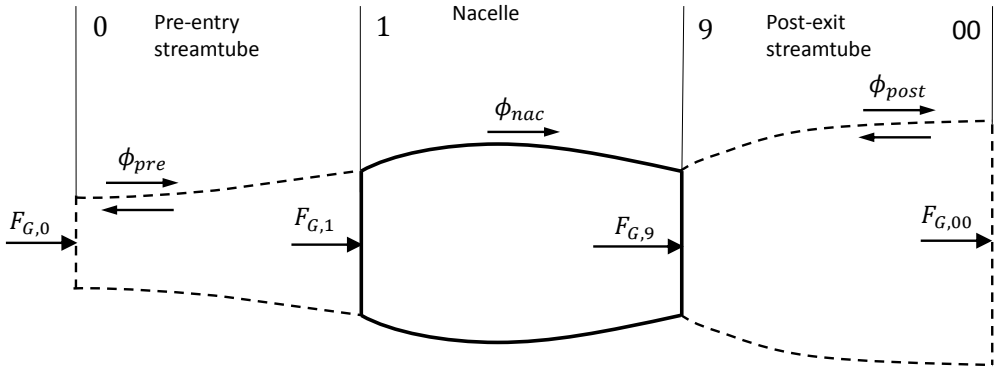

Figure 2.12: Forces acting on the defined domain. Source: *MIDAP Study Group* [8]

- Equivalent Post exit streamtube: The streamtube extends from the duct exit 9 to infinity downstream 00.In the absence of mixing, its boundaries separate the internal and external flows. The jet from the core and fan nozzles is then mixed with the external flow at the infinity downstream, where the streamtube disappears.

By defining this domain external and internal flow is separated by the streamtube in order to give a consistent definition in which the overall longitudinal forces are defined. The thrust is related with the internal flow (passes through the duct), as is the main force of interest for engine manufacturers. The external flow (passes around the body) produces the drag, force of interest for the external aerodynamicists.

No shear stress occurs between the external and internal flows along the streamtube. As a result of this definition internal and external drags are not necessarily stresses on the surfaces of the body, but are related with the imaginary boundary between internal and external flow. The internal and external forces which act on the pre-entry streamtube are balanced. As a result the streamtube can be considered as a "impervious membrane incapable of sustaining a pressure difference" [8].

2.5.3. THRUST COMPONENTS

Thrust represents the change of stream force between the entry and exit stations, the net gauge force introduced in Subsection 2.5.1. The net thrust can be divided according to the control volume of Figure 2.12:

- Pre-entry thrust: is the force parallel to the freestream originated from the pressure forces acting on the pre-entry streamtube internal surface. It is dependent on the conditions at the nacelle entry and at the undisturbed stream. Acts as a form of an external pressure near the lips of the engine intake.

$$F_{pre} = \int_1 \left(\rho_1 V_1^2 + P_1 - P_0\right) \mathrm{d}A_1 - \rho_0 V_0^2 A_0 \tag{2.10}$$

- Intrinsic thrust: is the force in the direction parallel to the freestream due to the pressure and friction forces acting on the internal surface of the duct. Depends also on the conditions at the exit, which are assumed measurable and calculable. The friction forces are measured from the stagnation point at the inlet to the nozzle exhaust.

$$F_{int} = \int_9 \left(\rho_9 V_9^2 + P_9 - P_0\right) \mathrm{d}A_9 - \int \left(\rho_1 V_1^2 + P_1 - P_0\right) \mathrm{d}A_1 \tag{2.11}$$

- Post-exit thrust: is the force parallel to the freestream caused from the pressure forces acting on the internal surface of the equivalent post exit streamtube. It relates the conditions at infinity downstream to those at the jet exit. It is only present if in the region surrounding the exit jet the static pressure distribution differs from the undisturbed freestream static pressure. It acts in the form of an external pressure near the jet exit [43]. In this case the post-exit thrust depends on combined internal and external flows.

$$F_{post} = \int_{00} \rho_{00}\, V_{00}^2 \,\mathrm{d}A_{00} - \int \left(\rho_9\, V_9^2 + P_9 - P_0\right) \mathrm{d}A_{00} \tag{2.12}$$

2.5.4. IDEAL APPROACH: OVERALL NET THRUST

By choosing the entry and exit interfaces infinite upstream (0) and infinite downstream (00) the "Overall Net Thrust" can theoretically be determined. The Overall Net Thrust is defined as "the rate of change of momentum of the fluid that flows through the engine (internal flow) between stations at infinity upstream and infinity downstream" [39]. It is the addition of pre-entry, intrinsic and post-exit thrust, the ideal approach for bookkeeping the thrust.

$$F'_N = F_{G_{00}} - F_{G_0} = \int \rho_{00}\, V_{00}^2 \,\mathrm{d}A_{00} - \dot{m}_0\, V_0 \tag{2.13}$$

If using the Overall Net Thrust as definition of Thrust, the entry interface satisfies the requirements of the bookkeeping method as it is precisely defined in terms of aircraft velocity and is the only station free of any disturbance originated by the body. In theory this definition should be used. However, the uncertainties and arbitrary nature of the conditions far downstream due to wake mixing makes in practice this definition unused.

As a result the definition of gross and net thrust depend on the integration over the internal flow at station 00 far downstream. It is necessary to relate the conditions at 00 with those at the jet exit (9). As a result, the practical definitions of the thrust depend on the accuracy of these approximations.

2.5.5. CURRENT APPROACH: STANDARD NET THRUST

The Standard Thrust is used in the current approach at DNW. Station 9 is chosen as the downstream reference station. It is assumed that there is no thrust contribution between the exhaust plane 9 and far downstream 00, by considering that the flow expands isentropically to freestream conditions at station 9. The post-exit thrust and flow suppression is then neglected. This expression is correct if the jet is discharged into a region where the local pressure is equal to P_{00}:

$$F_{N,Standard} = F_{G_9} - F_{G_0} = \dot{m}_9\, V_9 + A_9 \left(P_{s,9} - P_{s,0}\right) - \dot{m}_0\, V_0 \tag{2.14}$$

2.5.6. MODIFIED APPROACH: JONES NET THRUST

The standard thrust does not consider the post-exit force. However, this is present if in the surrounding of the jet exit the pressure differs from the freestream. It depends then of the combined internal and external flow. In order to obtain the post-exit force it is necessary to assume the pressure distribution at the exhaust plane.

The Jones thrust [39] is used for convergent nozzles that expands into a region where the local pressure is different than P_{00}. It is assumed that the jet contracts or expands isentropically and adiabatically from the exhaust to the freestream pressure P_{00} without transfer of momentum and energy through the mixing in the wake. Conditions at 00 calculated from those at 9 using the equations of mass flow continuity and energy of isentropic flow. As a result the Jones Gross Thrust can be calculated:

$$F_{G,Jones} = \int \rho_e V_e^2 \left[1 + \frac{2}{(\gamma-1)\, M_e^2}\left(1 - \left(\frac{P_{00}}{P_e}\right)^{\frac{\gamma-1}{\gamma}}\right)\right] \mathrm{d}A_e \tag{2.15}$$

The Jones Gross Thrust is equivalent to the product of the actual mass flow following the local Nozzle Pressure Ratio, NPR_{loc}, and the ideal velocity isentropically expanding to freestream conditions:

$$F_{G,Jones} = \dot{m}_9\,(NPR_{loc})\; V_9\,(NPR_0) \tag{2.16}$$

Both equations 2.15 and 2.16 propose a different bookkeeping approach that can deal with flow suppression and the post-exit force. It is considered an alternative of the Overall Net Thrust, theoretical definition of

thrust, that can be easily measured. In order to take into account boattail and scrubbing drag, the Modified Jones Gross Thrust is introduced:

$$F^*_{G,Jones} = F_{G,Jones} - D_{scrubbing} - D_{Boattail} \tag{2.17}$$

Equation 2.17 consistent definition of thrust is introduced for the bookkeeping of the turbofan thrust.

2.6. CONCLUSIONS

In the presented chapter the units of study, a very high bypass ratio TPS and TFN have been introduced. Differences in the performance of the TPS have been found between calibration and wind tunnel conditions, especially at low power settings. A possible explanation is the influence of the external flow on the TPS exhaust. This influence is neglected by the current bookkeeping approach. In the past, traditional high bypass ratio engines operated at chocked conditions. The shift towards very-high bypass ratio engines not only reduces the fan nozzle pressure ratio, but also reduces the distance of the engines to the aircraft wing.

Following these problems it has been found that the external flow and wing pressure field can change the static pressure at the fan exhaust plane. In unchocked conditions, flow suppression is originated. The TPS suffers a decrease of the fan mass flow and exhaust velocity. The boattail and scrubbing drag are also affected with respect to the calibration conditions. These two effects change of the TPS thrust leading towards an improperly bookkeeping of the aircraft installation drag.

A possible solution lies in the definition of thrust. The current approach neglects the thrust contribution from the nozzle exhaust (station 9) to infinite downstream (00). This simplification is not valid when the exit pressure differs from the freestream. By expanding the flow from the exhaust to 00 without any transfer of energy of momentum it is possible to relate conditions at 00 from those at 9. As a result the Jones Thrust must be used in the new bookkeeping method, together with the accounting of the boattail and scrubbing drag.

Once these limitations have been defined, the proposed bookkeeping method will be evaluated in the following chapters by means of a theoretical, numerical and experimental approach.

3

PARAMETRIC ANALYSIS

This chapter quantifies with more detail the described limitations by implementing the modified bookkeeping method into a mathematical model in Section 3.1. This analysis will be the reference for the numerical and experimental studies. The obtained differences due to the modified bookkeeping method are compared with respect to the current instrumentation error by means of an exhaustive error propagation analysis in Section 3.2.

3.1. MATHEMATICAL MODEL

In this section the influence of flow suppression in the TPS performance is obtained. The influence of boattail and scrubbing drag are strongly dependent on the geometry. These will be evaluated separately in the numerical and experimental study.

The effect of flow suppression on the TPS can be modelled by increasing the static pressure at the fan exhaust plane at a given power condition (Fan Nozzle Pressure Ratio) and freestream Mach number. The following section describes the equations used to determine the TPS thrust according to the modified bookkeeping method introduced in the Section 2.5.

3.1.1. SETTING UP OPERATING CONDITIONS

The first step in the theoretical analysis is the definition of the operating conditions (independent variables).

MACH NUMBER

The freestream static pressure $P_{s,0}$ is fixed to 101300 Pa, while the freestream total pressure is modified in order to meet the required Mach number according to the 1-dimensional isentropic expansion equation:

$$P_{t,0} = P_{s,0}\left(1 + \frac{\gamma - 1}{2}M^2\right)^{\frac{\gamma}{\gamma-1}} \tag{3.1}$$

This makes the simulation of the TPS at any given freestream velocity possible.

POWER CONDITIONS

The power conditions are directly changed by modifying the freestream Fan Nozzle Pressure Ratio $FNPR_0$, and setting the fan total pressure accordingly, $P_{t,fan} = P_{t,17}$, according to the fixed freestream static pressure:

$$FNPR_0 = \frac{P_{t,17}}{P_{s,0}} \tag{3.2}$$

SUPPRESSION LEVEL

In order to maintain a dimensionless suppression level, the pressure at the fan exhaust face $P_{s,e}$ is modified by means of the pressure coefficient, $C_{P,fan}$. When the pressure is equal to the freestream pressure the pressure coefficient is zero. This is then increased following from the analysis of the airfoil in isolation in Section 2.3.2.

$$C_P = \frac{P_{s,e} - P_{s,0}}{\frac{1}{2}\rho V_0^2} = \frac{2}{\gamma M_0^2}\left(\frac{P_{s,e}}{P_{s,0}} - 1\right) \tag{3.3}$$

Following equation 3.3 it is possible to solve for $P_{s,e}$, the local pressure at the fan exhaust and obtain the local fan nozzle pressure ratio. Figure 3.1 a shows the variation of $FNPR_{loc}$ according to the freestream power settings $FNPR_0$ and Mach number M_0.

$$FNPR_{loc} = \frac{P_{t,17}}{P_{s,e}} \tag{3.4}$$

3.1.2. EFFECT OF SUPPRESSION IN TPS PERFORMANCE

The following subsection is a direct application of the Modified Thrust/Drag Bookkeeping Method, introduced in Section 2.5. Once the Mach number, Power Conditions and Suppression Level has been determined, it is possible to quantify the error in the key performance parameters.

CHANGE IN TPS FAN MASS FLOW

With the local nozzle pressure ratio the ideal mass flow is obtained, assuming perfect expansion and no losses between the nozzle measurement station, 17, and the exhaust face, 19, where $P_{s,e}$ is present:

$$\dot{m}^e_{fan_{id}} = \dot{m}_{19_{id,e}} = \frac{P_{t,17}A_{19}}{\sqrt{T_{t,7}}} FNPR_{loc}^{\frac{-1}{\gamma}} \sqrt{\frac{2}{R}\frac{\gamma}{\gamma-1}\left(1 - FNPR_{loc}^{\frac{1-\gamma}{\gamma}}\right)} \quad \text{if } FNPR_{loc} < 1.89 \tag{3.5}$$

When the local nozzle pressure ratio is higher than the critical nozzle pressure ratio, chocked conditions occur and equation 3.5 is no longer valid. The mass flow is fixed and it does not depend on the local flow conditions.

$$\dot{m}^{*e}_{19_{id}} = \frac{P_{t,17}A_{19}}{\sqrt{T_{t,17}}}\left(\frac{2}{\gamma+1}\right)^{\frac{1}{\gamma-1}} \sqrt{\frac{2}{R}\frac{\gamma}{\gamma-1}} \quad \text{if } FNPR_{loc} \geq 1.89 \tag{3.6}$$

The original mass flow (according the current bookkeeping method) can be obtained by substituting in equations 3.5 and 3.6 the local Nozzle Pressure Ratio, $FNPR_{loc}$ by the freestream Nozzle Pressure Ratio, $FNPR_0$, obtained in equation 3.2.

CHANGE IN TPS FAN EXHAUST VELOCITY

The Velocity at the fan exhaust plane is also reduced:

$$V^e_{fan_{id}} = V_{19_{id}} = \sqrt{\frac{2\gamma R T_{t,17}}{\gamma-1}\left(1 - FNPR_{loc}^{\frac{1-\gamma}{\gamma}}\right)} \tag{3.7}$$

The Jones thrust assumes the expansion of this velocity to freestream conditions, V_0, by substituting in equation 3.7 the local Nozzle Pressure Ratio, $FNPR_{loc}$ by the freestream Nozzle Pressure Ratio, $FNPR_0$, from equation 3.2.

Figure 3.1 b-e shows the difference in mass flow and exhaust velocity between the existing approach at DNW and the proposed method taking into account flow suppression. The analysis is done at different Mach numbers, M_0, and Power Settings, $FNPR_0$, for a pressure coefficient (suppression level) of 0.3. The graphs show the differences both in absolute number and in relative error. As the suppression level (pressure coefficient at the exhaust plane) is increased, these differences are proportionally increased.

The absolute reduction in mass flow and velocity has higher influence at low Fan Nozzle Pressure Ratios. Regarding the influence of the Mach number, the absolute difference increases at high Mach numbers, as both mass flow and exhaust velocity are also higher. However, the relative difference in mass flow is dominant at low Mach numbers and low power settings.

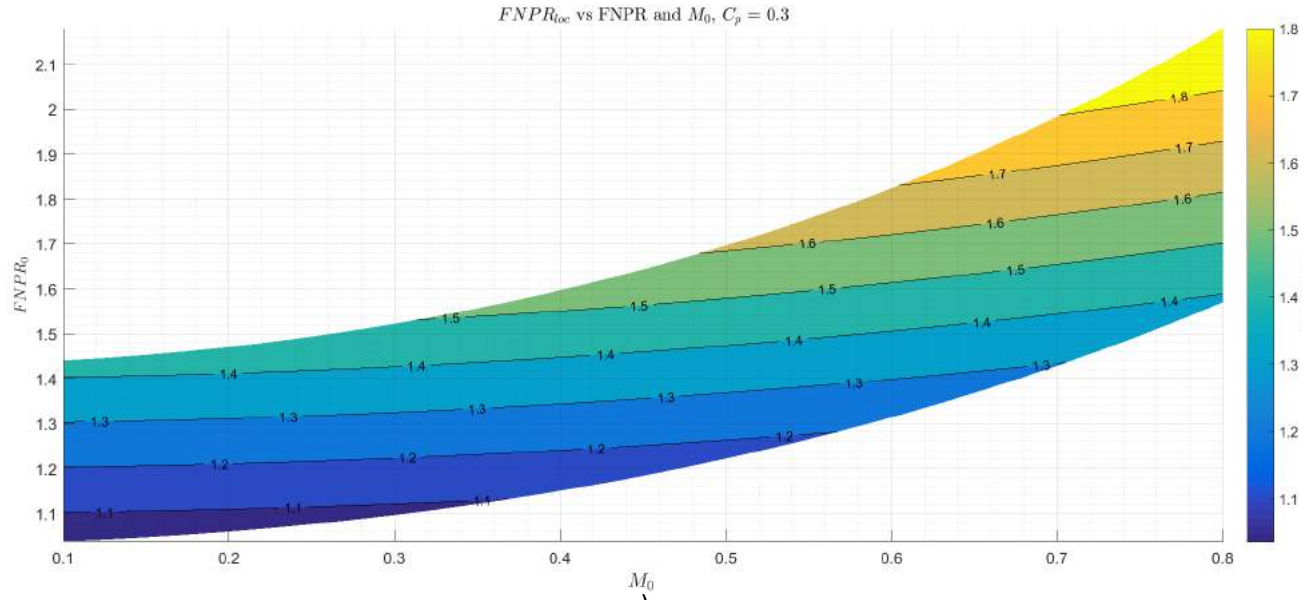

a)

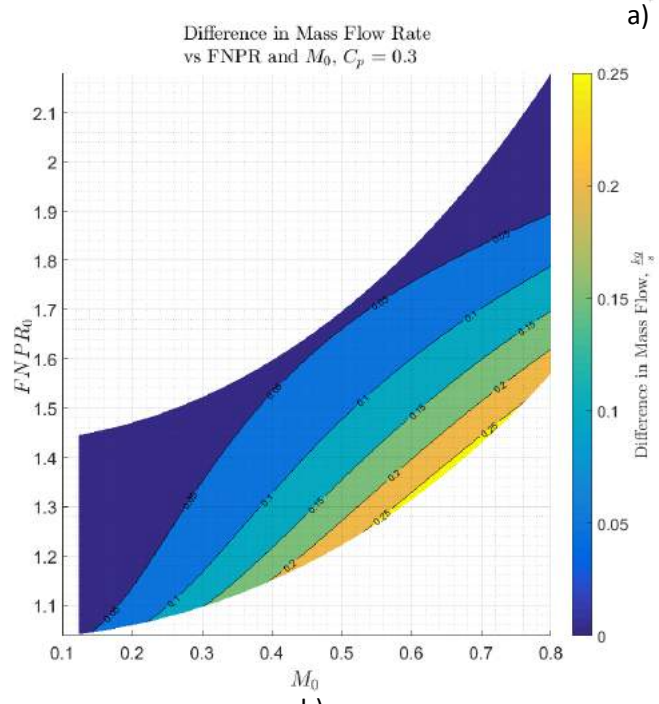

b)

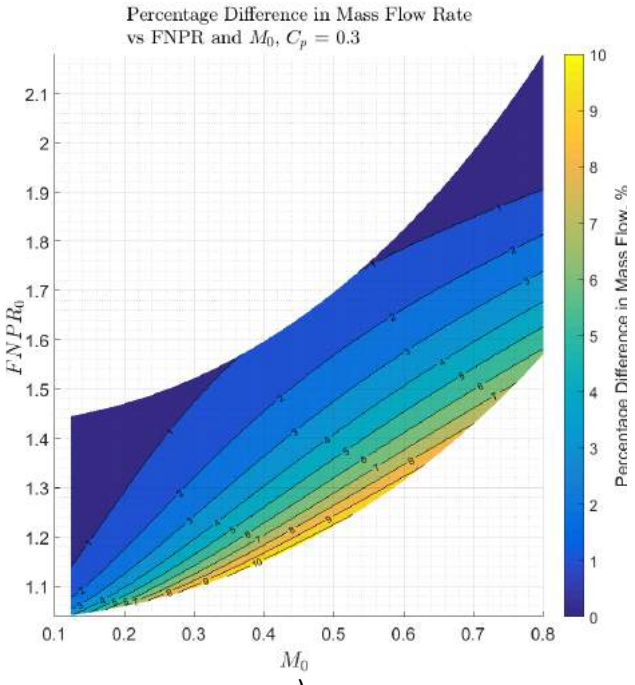

c)

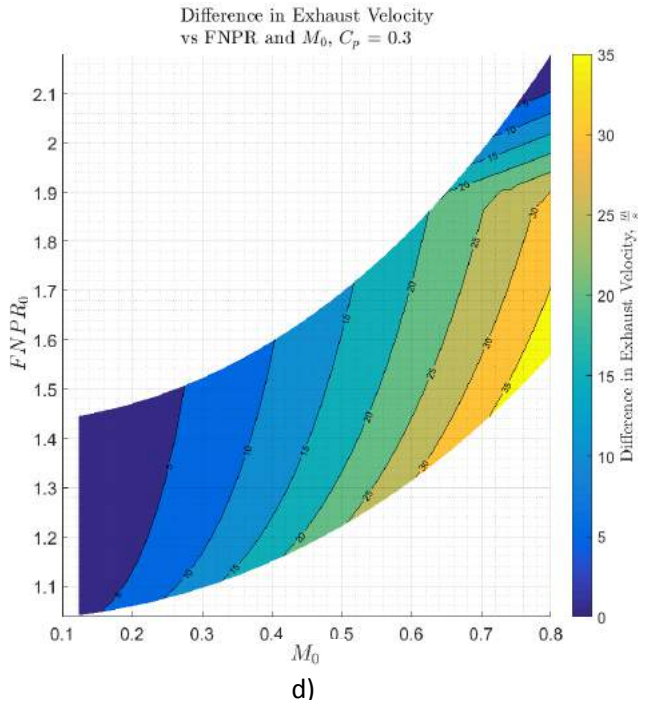

d)

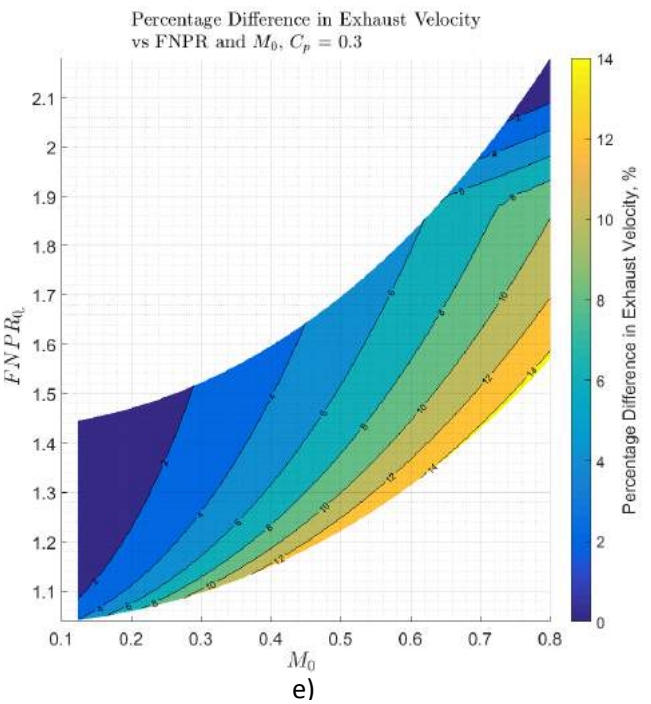

e)

Figure 3.1: Difference between existing and proposed approach, vs freestream Mach number, M_0 and freestream Fan Nozzle Pressure Ratio $FNPR_0$ in: **a**: local Fan Nozzle Pressure Ratio, $FNPR_{loc}$ **b**: Absolute difference in fan mass flow rate, $\dot{m}_{fan,id}$, $[kg/s]$ **c**: Relative difference in mass flow rate, $p\%$] **d**: Absolute difference in fan exhaust velocity, V_{fan}, $[m/s]$ **e**: Relative difference in fan exhaust velocity

The white areas of the graph are unfeasible regions. For example, it is not possible to reach very low Fan Nozzle Pressure Ratios at high Mach numbers as the total pressure of the flow, $\frac{P_{t,0}}{P_{s,0}}$ is already high.

CHANGE IN TPS FAN GROSS THRUST

Following the Jones definition of thrust, the ideal Fan Gross Thrust is defined as the momentum of the reduced mass flow, $\dot{m}^e_{fan_{id}}$ expanded to freestream conditions (00). This is different to the standard gross thrust currently bookkeept at DNW which does not consider the reduction in mass flow:

$$F^{JONES}_{G,fan} = \dot{m}^e_{fan_{id}} V^0_{fan_{id}} \qquad \text{and} \qquad F^{STD}_{G,fan} = \dot{m}^0_{fan_{id}} V^0_{fan_{id}} \tag{3.8}$$

Then, the difference in gross thrust due to flow suppression is equal to:

$$\Delta F_G = V^0_{fan} \left(\dot{m}^0_{fan} - \dot{m}^e_{fan} \right) \tag{3.9}$$

CHANGE IN TPS RAM DRAG

The same approach is followed with the ram drag:

$$F^{JONES}_{RAM} = \dot{m}^e_{fan_{id}} V_0 \qquad \text{and} \qquad F^{STD}_{RAM} = \dot{m}^0_{fan_{id}} V_0 \tag{3.10}$$

And its difference:

$$\Delta F_{RAM} = V_0 \left(\dot{m}^0_{fan} - \dot{m}^e_{fan} \right) \tag{3.11}$$

CHANGE IN TPS FAN NET THRUST

As a result the net thrust is the momentum difference between the exhaust (gross thrust) and intake (ram drag):

$$F^{JONES}_{N,fan} = F^{JONES}_{G,fan} - F^{JONES}_{RAM} \qquad \text{and} \qquad F^{STD}_{N,fan} = F^{STD}_{G,fan} - F^{STD}_{RAM} \tag{3.12}$$

$$\Delta F_{NET} = \left(\dot{m}^0_{fan} - \dot{m}^e_{fan} \right) \left(V^0_{fan} - V_0 \right) \tag{3.13}$$

The absolute and relative differences in gross thrust, ram drag and net thrust have been calculated at different Mach numbers and freestream local pressure ratios, as shown in Figure 3.2. Absolute differences in gross thrust and ram drag are most important at high Mach numbers and low power settings. Regarding the net thrust, the maximum differences between old and new calibration approach shift towards medium Mach numbers and medium power settings, as shown in Figure 3.2 f. Figure 3.3 shows the absolute error in dragcounts useful for the determination of the error in the bookkeeping of drag.

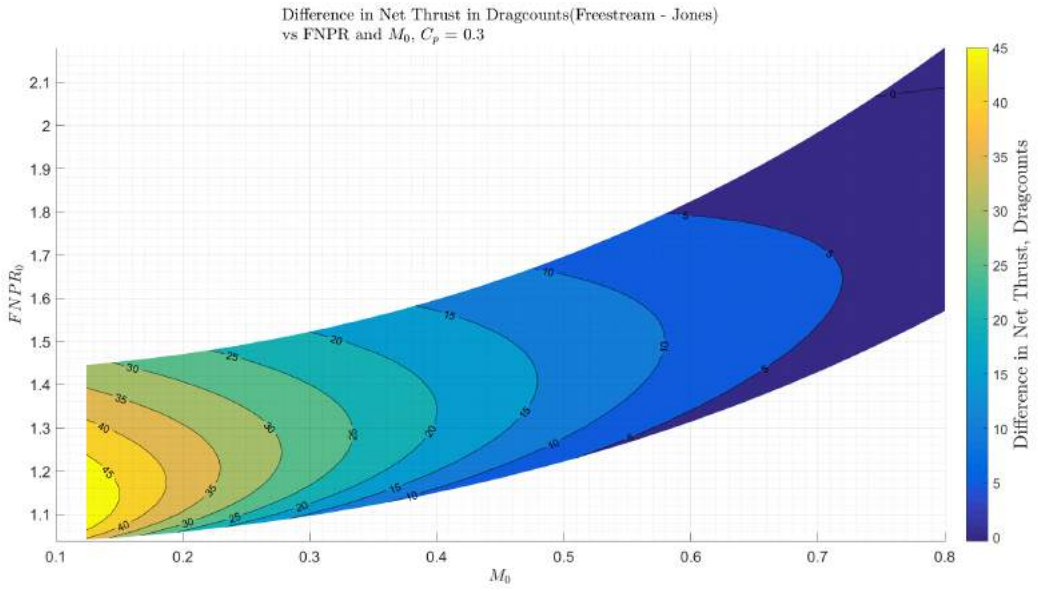

Figure 3.3: Absolute difference in fan net thrust due to bookkeeping error [$dragcounts$]

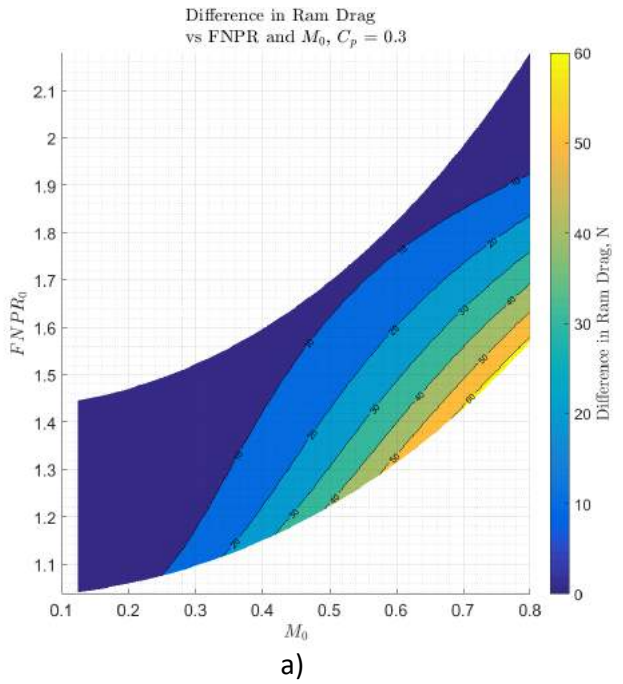

a)

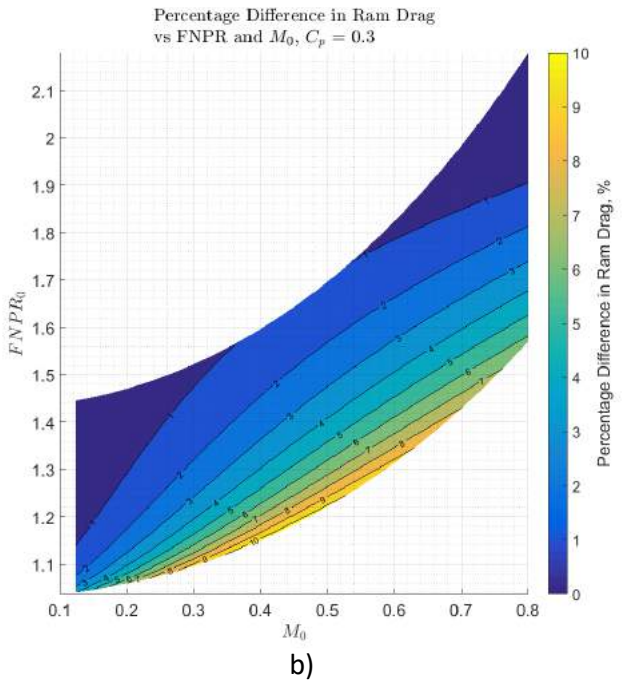

b)

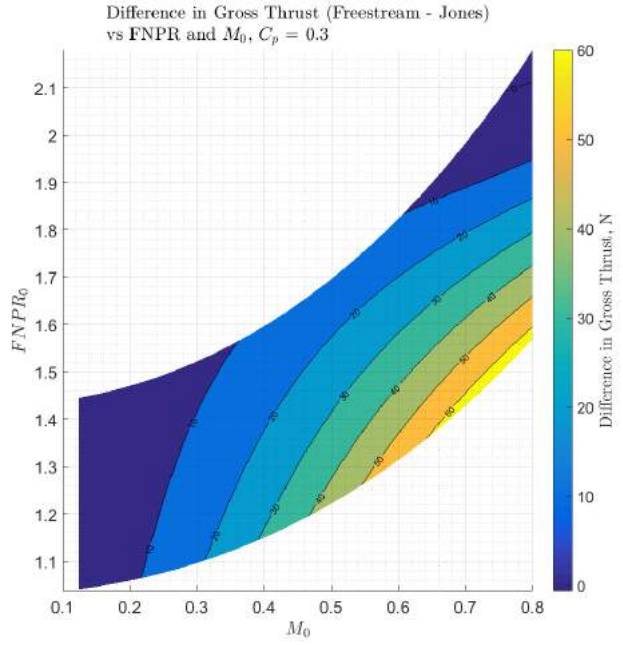

c)

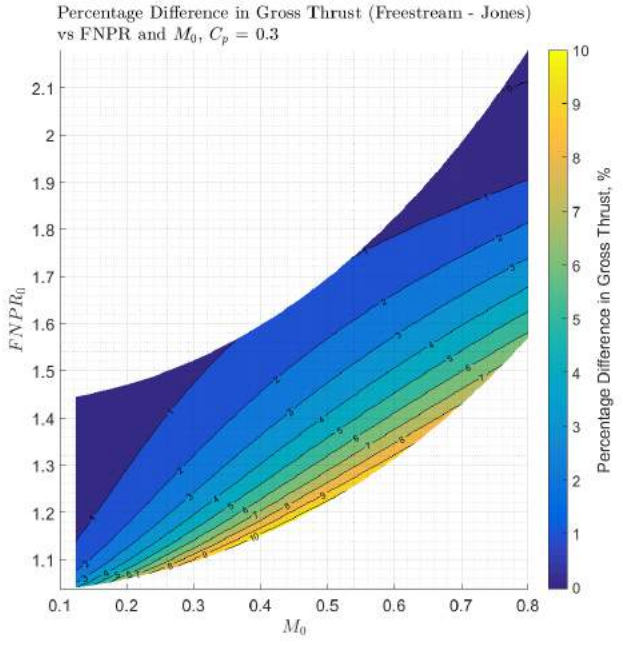

d)

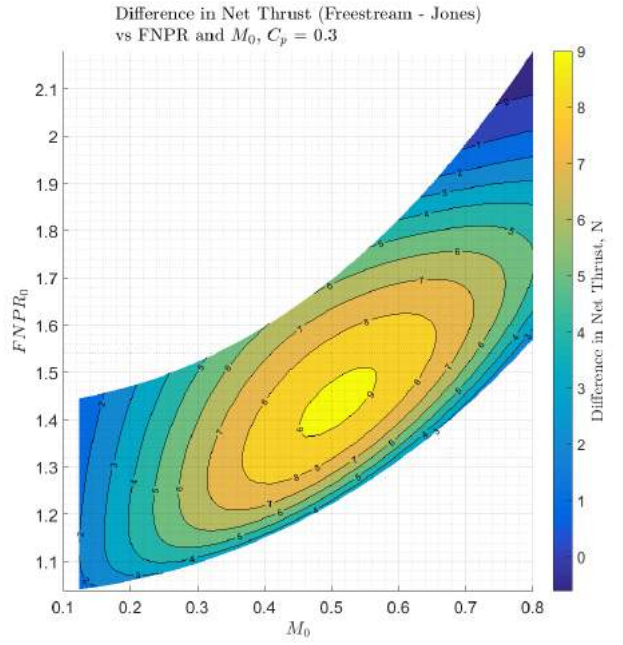

e)

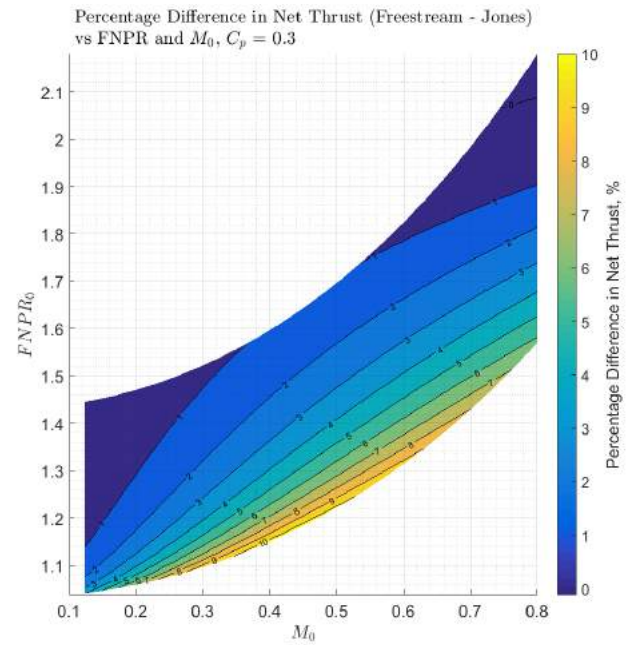

f)

Figure 3.2: Difference between existing and proposed approach, vs Mach number, M_0 and Fan Nozzle Pressure Ratio $FNPR_0$ in: **a**: Absolute difference in fan ram drag, [N] **b**: Relative difference in fan ram drag, [%] **c**: Absolute difference in fan gross thrust, [N] **b**: Relative difference in fan gross thrust, [%] **d**: Absolute difference in fan net thrust, [N] **e**: Relative difference in fan net thrust, [%]

3.1.3. EFFECT OF SUPPRESSION IN TFN PERFORMANCE

A similar analysis is done for the Through-Flow Nacelle, representing idle conditions. In this case the unit is unpowered, and the Fan Nozzle Pressure Ratio depends only on the freestream conditions, as it has been previously introduced. Also, the local nozzle pressure ratio is slightly different:

$$FNPR_0^{TFN} = \frac{P_{t,tunnel}}{P_{s,tunnel}} = \left(1 + \frac{\gamma - 1}{2} M_0^2\right)^{\frac{\gamma}{\gamma-1}} \quad \text{and} \quad FNPR_{loc}^{TFN} = \frac{P_{t,tunnel}}{P_{s,e}} \tag{3.14}$$

Figure 3.5 a shows that the increase in the exhaust pressure coefficient modifies the local Fan Nozzle Pressure Ratio from its original value (dotted line).

The decreased mass flow and exhaust velocity due to flow suppression follow equations 3.5 and 3.7. Also the decreased gross thrust and ram drag follow equations 3.8 and 3.10. As shown in Figure 3.5 the maximum decrease in velocity and mass flow is at high Mach numbers and suppression levels.

According to equation 3.12, the TFN exhaust velocity expanded to freestream conditions V_{fan}^0 should be equal to freestream velocity, V_0, and ram drag and gross thrust cancel each other. As a result, both the Jones and the Standard Net Thrust are equal to zero, when ideal conditions are used. However, this is no longer valid when losses are taken into account, as will be shown in Section 5.2 (the CFD study of the TFN).

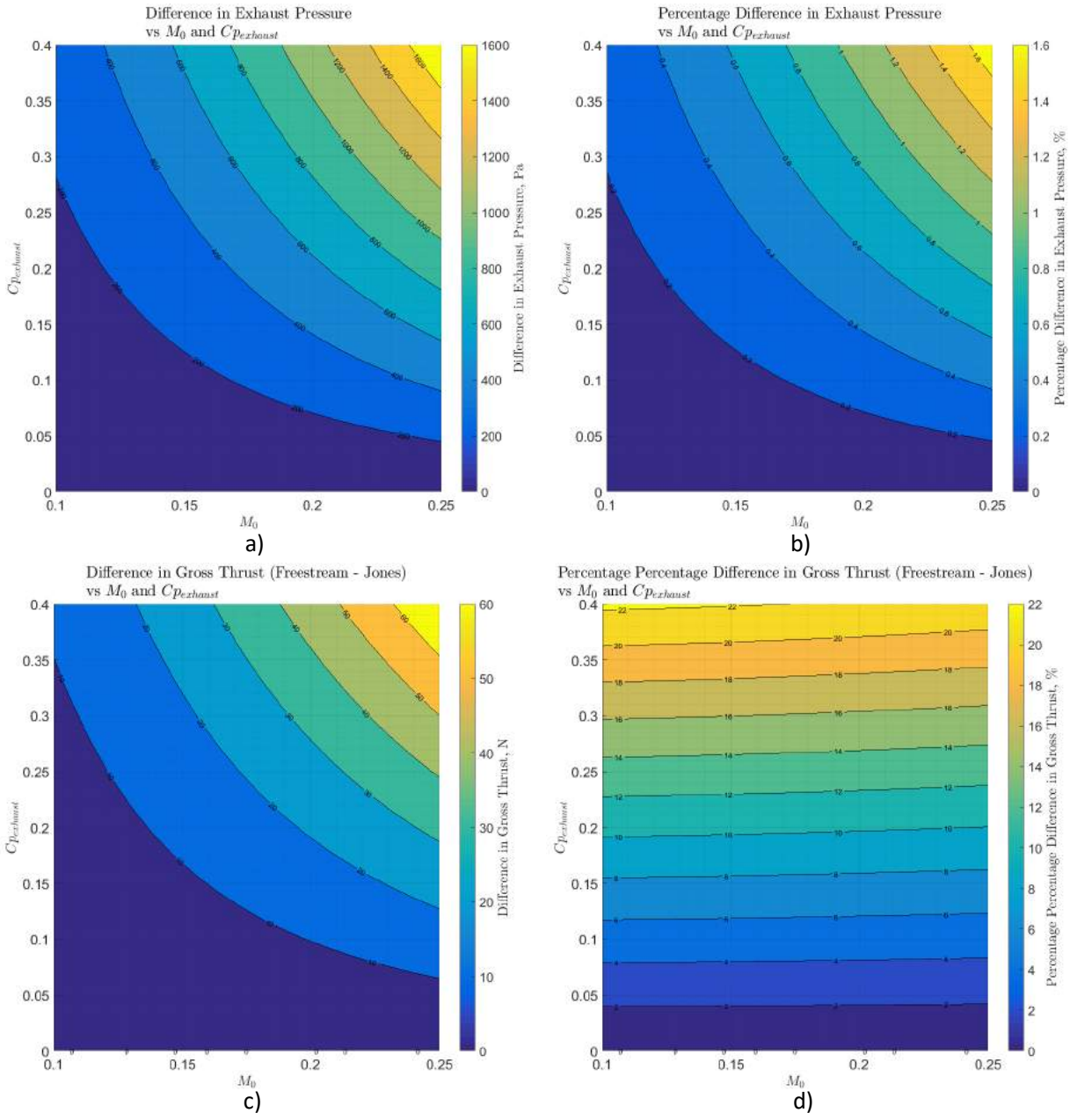

Figure 3.4: Difference between existing and proposed approach, vs freestream Mach number, M_0 and suppression level C_P for TFN in: **a**: Absolute difference in fan exhaust static pressure, $[Pa]$ **b**: Relative difference in fan exhaust static pressure, [%] **c**: Absolute difference in fan gross thrust, $[N]$ **d**: Relative difference in fan gross thrust

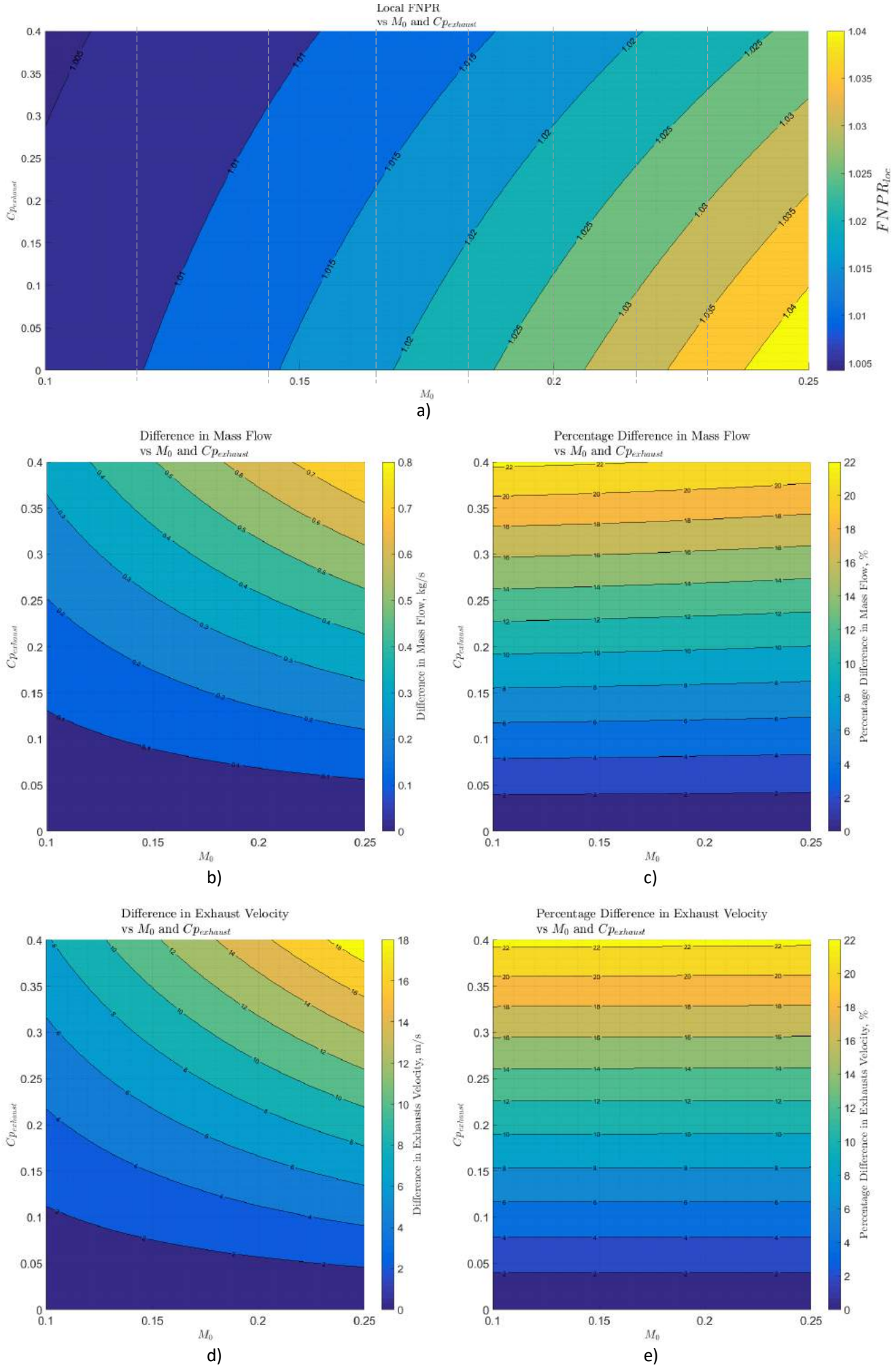

Figure 3.5: Difference between existing and proposed approach, vs freestream Mach number, M_0 and suppression level C_P for TFN in: **a**: local Fan Nozzle Pressure Ratio, $FNPR_{loc}$ **b**: Absolute difference in fan mass flow rate, $\dot{m}_{fan,id}$, $[kg/s]$ **c**: Relative difference in mass flow rate, p%] **d**: Absolute difference in fan exhaust velocity, V_{fan}, $[m/s]$ **e**: Relative difference in fan exhaust velocity, [%]

3.1.4. EFFECT OF BOATTAIL AND SCRUBBING DRAG IN TPS PERFORMANCE

In a similar manner the boattail and scrubbing drag can be monitored and added to the thrust contribution.

BOATTAIL DRAG

By measuring and integrating the static pressure in the fan and core cowling it is possible to determine the pressure forces acting in the x direction. It is expected that the pressure distribution at the fan cowling is directly proportional to the exhaust pressure, $P_{s,e}$. The net pressure force in axial direction depends on the shape of the boattail, so boattail drag could have a negative sign by acting in the direction and sense of thrust.

SCRUBBING DRAG

The scrubbing or friction drag is directly proportional to the velocity of the surface of the core cowling, as its value depends on the boundary layer shape [44]. With flow suppression, the reduction in exhaust velocity is expected to decrease the scrubbing drag.

3.2. ERROR PROPAGATION ANALYSIS

Once the mathematical model has been created, it is necessary to compare the order of magnitude of the bookkeeping error with respect to the current instrumentation error present at the experimental facility. To do so, a detailed analysis must take into consideration the error propagation of all the steps in the TPS testing: from the calibration to the wind tunnel testing. As the net thrust is subtracted from the model balance force in order to estimate the model drag, the uncertainty of thrust is directly related to the uncertainty of drag.

3.2.1. MODEL

The model follows Figure 3.6. The parameters in brackets are the factors (input values), independent of each other and measurable at DNW by sensors (prone to error). An initial baseline at a given Power Conditions and freestream Mach Number is selected, equivalent to the perfect case where measurement and physical values are equal (no measurement error is present). Any variation from the baseline condition of the response due to measurement error can be detected and traced back to the factors.

According to how the factors are modified (one by one or all at the same time by following a sequential approach or randomly) it is possible to perform different studies. The final objective is always to compare the final response (usually gross or net thrust) with respect to the baseline one.

The process is divided in three interconnected stages:

- Bellmouth Calibration: Temperatures and pressure measurements of the ambient and internal bellmouth and mass flow of the calibrated venturi tanks are the input parameters, and the output is the Bellmouth Discharge and Velocity Coefficients.
- TPS Calibration: During the calibration of the propulsive unit two components are present: the bellmouth and the TPS itself. As a result this stage is divided into:
  - Bellmouth: The input is the output from the previous section (bellmouth calibration coefficients) as well as the bellmouth internal measurements of pressure and temperatures and ambient conditions. The output is the calibrated mass flow, which is assumed according to the bookkeeping procedure to be the actual fan mass flow at the TPS calibration.
  - TPS unit: The input is the previously obtained calibrated fan mass flow, the core mass flow (dedicated sonic venturi), the balance force reading, the tank pressure and the internal total temperature and total pressure measurements from the core and fan probes. The output is the TPS discharge and velocity coefficients.
- Wind Tunnel conditions: the input is the output of the calibration phase (TPS velocity and discharge coefficients), internal readings of the TPS probes and wind tunnel conditions (total and static pressure). The output is the gross and net thrust of the TPS engine.

The model automatically calculates and visualizes the error in TPS net thrust obtained wind tunnel conditions as a result of an error in any measured (input) parameter. For simplification, flow suppression is not considered (or it is corrected for), so the analysis lies in the instrumentation error. For further insight of the role of each parameter the effects of the calibration measurements on the discharge and velocity coefficients are also calculated.

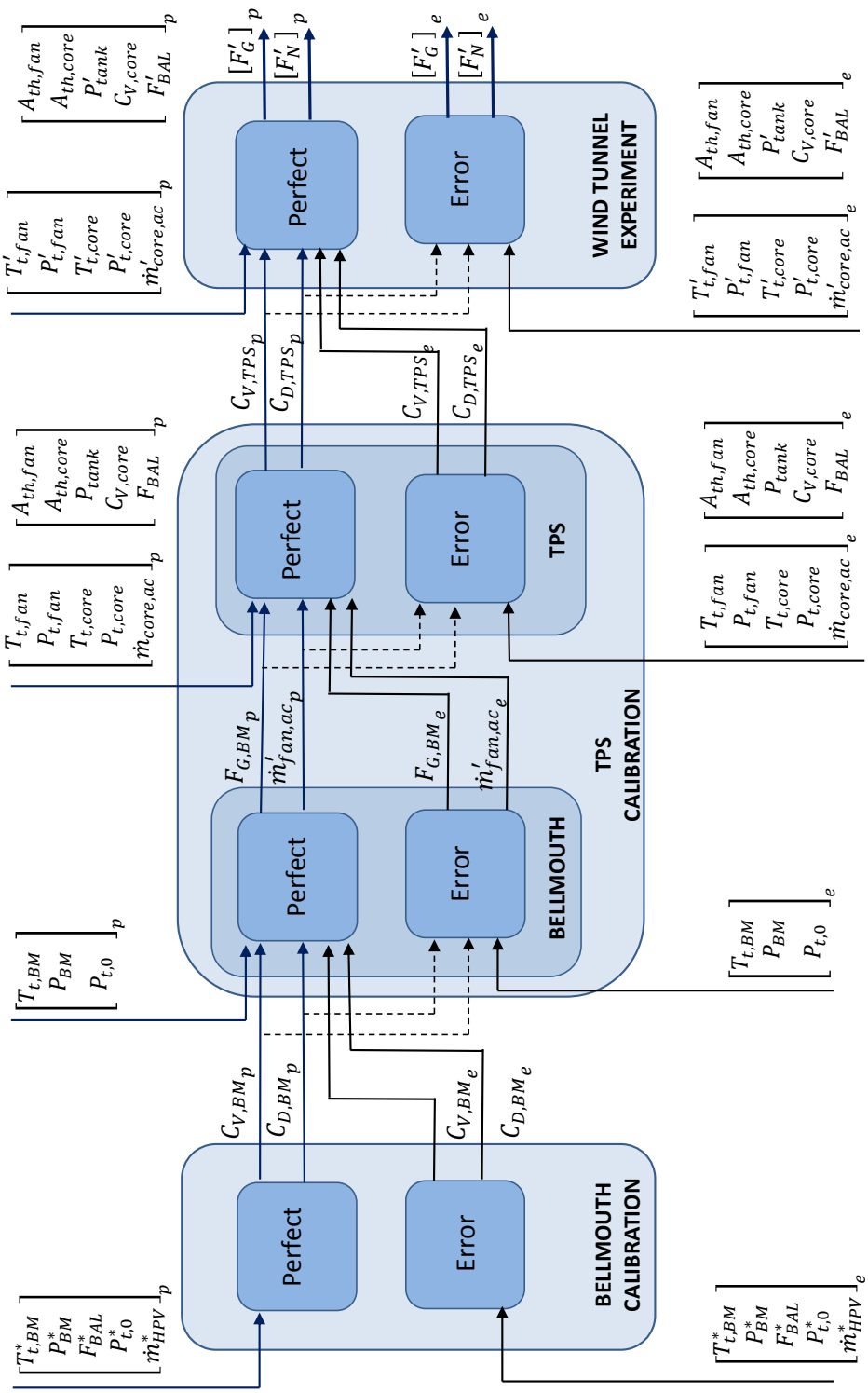

Figure 3.6: Sensitivity Analysis Model: inputs and outputs through bellmouth and TPS calibration and wind tunnel tests

3.2.2. SENSITIVITY ANALYSIS: ONE FACTOR AT A TIME

Once the model is built, a sensitivity study can be also used to determine which parameters are the most critical towards the determination of thrust.

One Factor at a time is the simplest approach consisting on changing one parameter every time and measuring the effect on the output [45]. A baseline approach is defined as the "ideal condition" obtained from actual experimental data and parameters are changed one by one keeping the others at their nominal value. Then the **Main Effect**, defined as the response change due to a change in the level of an individual variable, is obtained.

This approach does not take into account simultaneous variation of inputs variation, assuming that interactions do not occur in the model. That means that the factors affect the responses additively to the output [46]. However, this represents a first order of magnitude towards more sophisticated analysis.

RESULTS

The effects on Ram Drag, Gross Thrust and Net Thrust due to a 0.1% variation in the parameters at bellmouth calibration, TPS calibration and wind tunnel conditions is shown in Figure 3.7 for a single condition: $FPR = 1.24$ and $M_0 = 0.1$. The main parameters affecting the Net Thrust, F_N, are:

- Ambient total pressure during calibration, $P_{t,0}$ and during Wind Tunnel Test, $P'_{t,0}$
- Balance Calibration Force, F_G.
- Fan external Pressure at Calibration, $P_{fan,e}$. and in Wind Tunnel conditions $P'_{fan,e}$. Only in wind tunnel conditions this factor is relevant as the external flow can modify it. It is shown that when the external pressure in wind-on conditions increases and it is not measured, the thrust is considerably reduced.

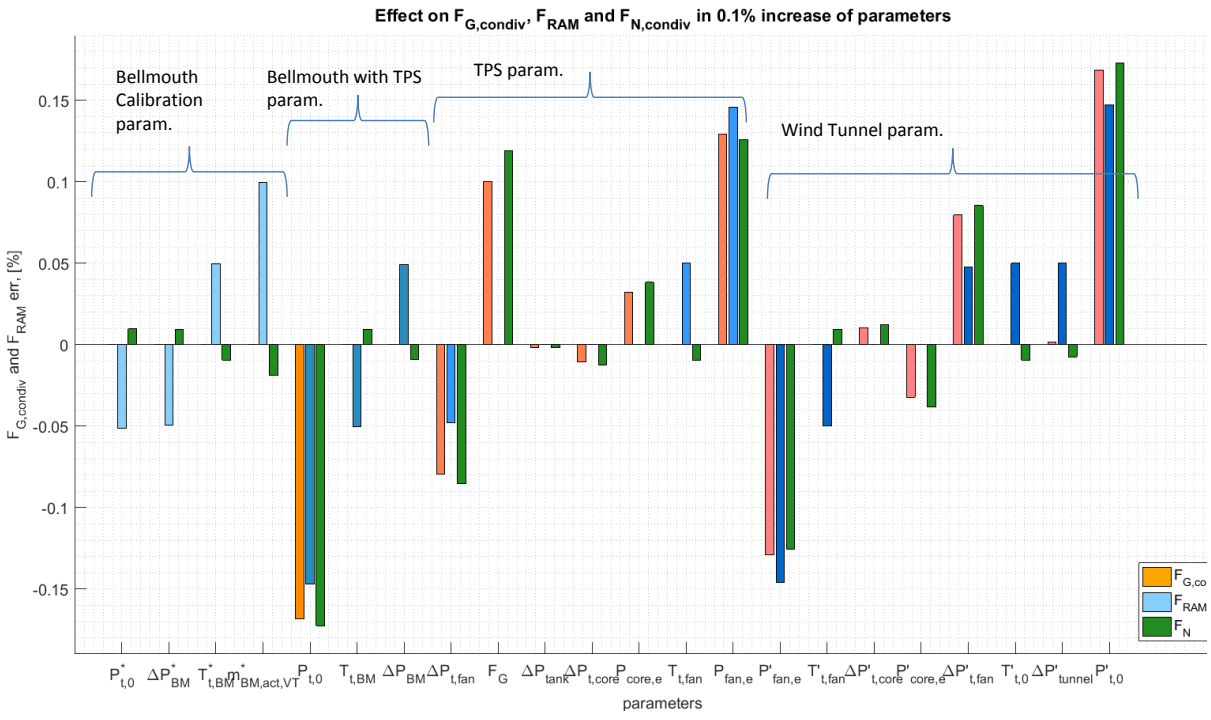

Figure 3.7: Effect of Gross Thrust, Net Thrust and Ram Drag in 0.1% in variation of parameters, Unchoked conditions

3.3. MONTE CARLO ANALYSIS

To estimate the total contribution of the combined testing technique to the final error the Monte Carlo Method is used. This is achieved by randomly sampling the error of the input parameters and studying its total propagation to the net thrust.

3.3.1. INPUT PARAMETERS

The error of the 22 input parameters is assumed to to follow a normal distribution, with mean μ 0, and standard deviation σ, according to the sensor requirements. As a result of this approach only random error is modelled, and it is assumed that the bias error is zero.

Table 3.1: DNW instrumentation error according to standard approach

Error	T_t [K]	P_t [Pa]	ΔP_s [Pa]	F_G [Pa]
μ	0	0	0	0
σ	0.5	100	20	1

3.3.2. SINGLE CASE

The Monte Carlo analysis is done simulating the calibration and testing conditions at $M_0 = 0.6$ and $FPR = 1.3$ (moderate power settings). Figure 3.8 a shows the convergence history of the standard deviation of the output parameter, the net thrust, as a function of the number of performed simulations. The number of simulations is set to 100000 as it provides a good trade-off between computation time and accuracy.

The histogram of the relative error of the net thrust, provided by the propagation model, is shown in Figure 3.8 b. Following the input distributions, the output also follows a normal distribution with mean error μ_{Error,T_N} of 0. As a result the standard deviation of the net thrust, σ_{Error,T_N}, is the parameter of interest to evaluate the error of the testing approach.

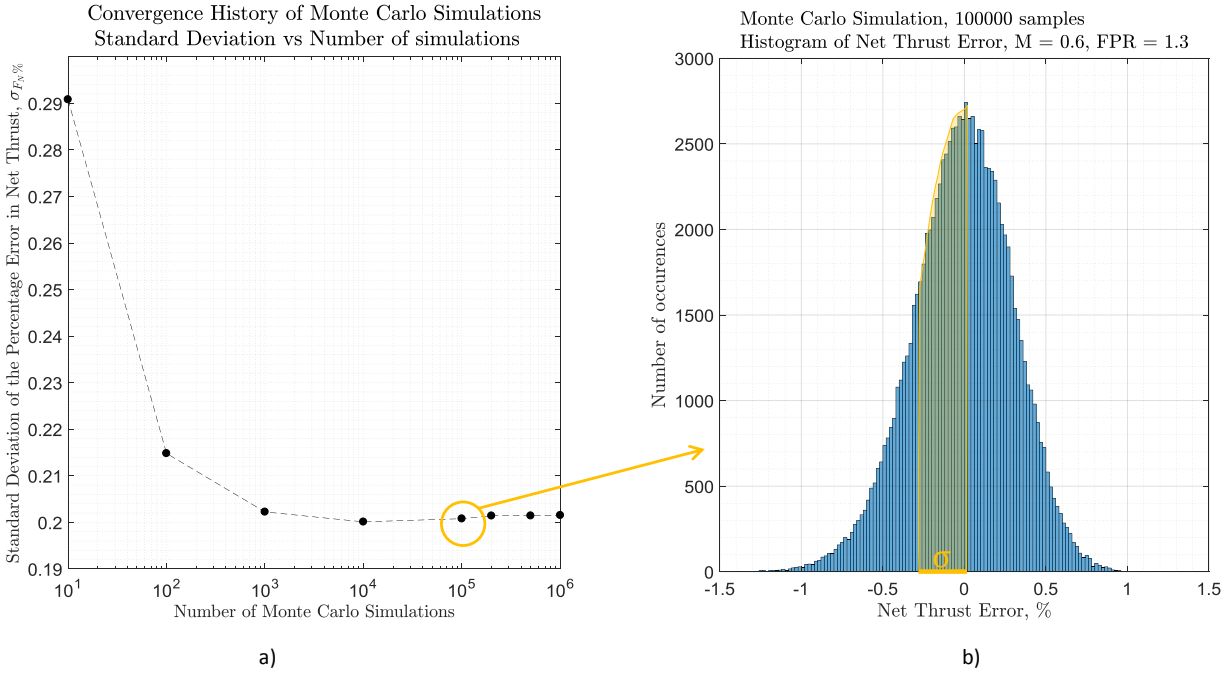

Figure 3.8: a: Convergence history of the standard deviation of the relative error in the Net Thrust vs the number of simulations. b: Histogram of relative error of net thrust at M_0 0.6 and FPR 1.3, 10^5 simulations

This method allows the estimation of the relative and absolute error of the net thrust at any given freestream velocity and power condition.

3.3.3. EXTENDED ANALYSIS

The above analysis is extended along the performance envelope of the TPS unit: from low ($M = 0.1$) to high ($M = 0.82$) speeds, and from low ($FPR = 1$) to high ($FPR = 1.42$) power settings. This allows to compare under which conditions the instrumentation error is maximum. In this case it is assumed that flow suppression, if present, is corrected for by measuring the exhaust static pressure and applying the modified bookkeeping method, introduced in Section 2.5. Then, only the instrumentation error is being investigated.

In Figures 3.9 a and b the standard deviation map of the relative and absolute error of the net thrust at different power settings and freestream velocities is shown. The analysis is obtained by performing the Monte Carlo simulations in a uniform grid of 30x30 points. As shown in the sensitivity analysis, the error is mainly affected by the balance (with an standard deviation of 1 N) and the total pressure measurement.

Following Figure 3.9 b, the relative instrumentation error is dominant at low power settings and low Mach numbers (the TPS net thrust is reduced under those conditions). The absolute error is higher at high Mach numbers and low power settings, as shown in Figure 3.9 b. The errors follows the expected order of magnitude assumed at DNW.

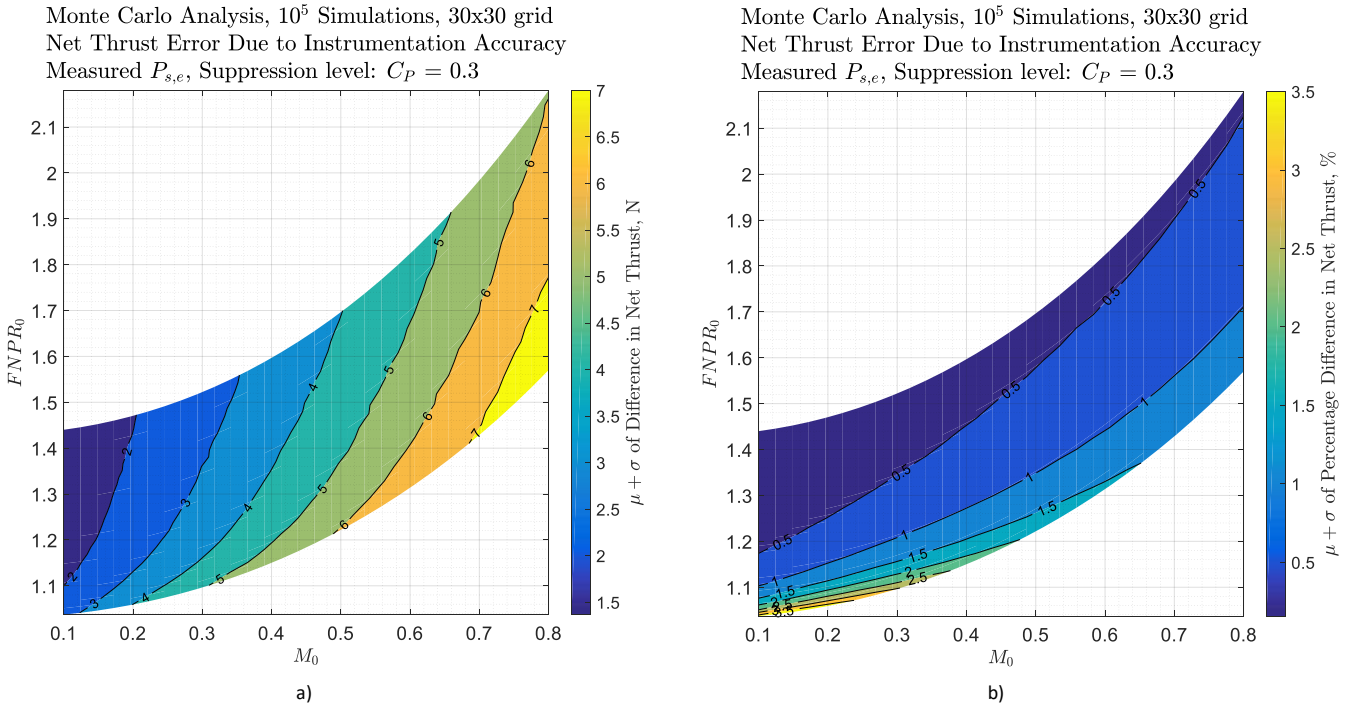

Figure 3.9: TPS Net Thrust error in the wind tunnel due to instrumentation accuracy along freestream Mach number and FNPR. a: Absolute error, %. b: Relative error, N

3.3.4. COMPARISON WITH FLOW SUPPRESSION

In Figure 3.10 the previous analysis of Figure 3.9 is compared with the case when flow suppression is not corrected for (current bookkeeping method). In this new case the incorrect bookkeeping error is added to the baseline instrumentation error. In both cases higher than freestream pressures are present in the fan plane ($C_P = 0.3$). The difference between both surfaces is then the difference in bookkeeping. Note that the Fan Pressure Ratio is chosen instead of the Fan Nozzle Pressure Ratio as Y axis, for a better visualization.

Figure 3.10 a shows the absolute error in thrust. The difference between current and proposed approach is higher at high Mach number and medium power settings. However, when looking at the relative error, Figure 3.10 a, the relative difference is higher at low power settings and high Mach numbers.

In conclusion, the bookkeeping error is one order of magnitude higher than the instrumentation error. The analysis shows that it is necessary to correct for flow suppression. With the new bookkeeping, the testing technique error falls within the minimum accuracy requirements for the TPS testing.

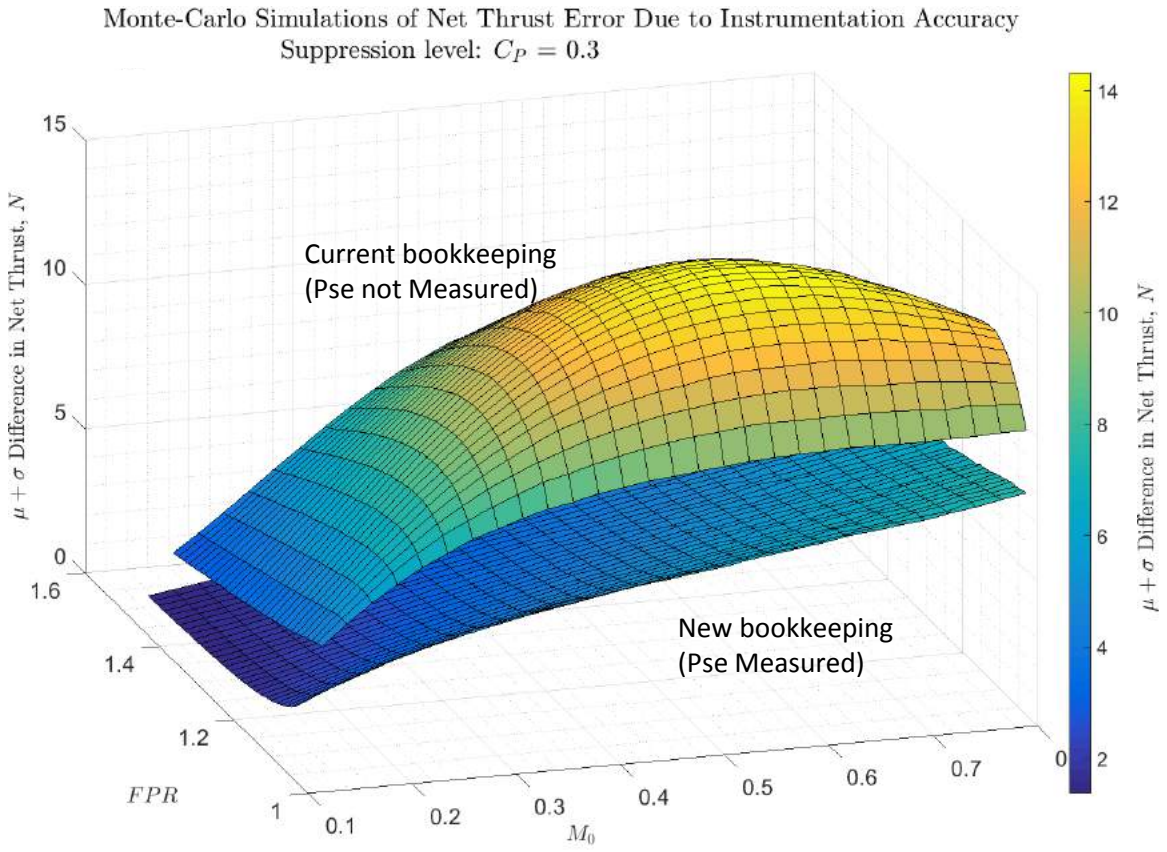

a)

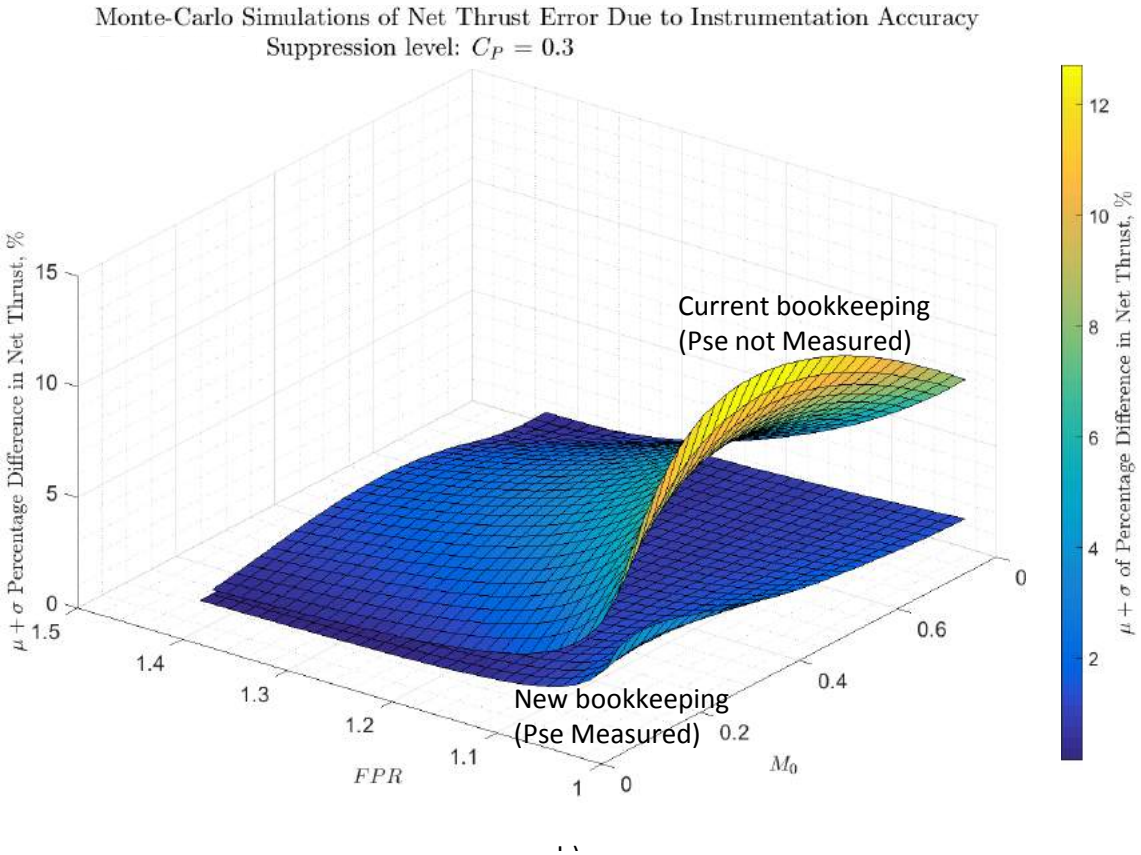

b)

Figure 3.10: Comparison between instrumentation error (new bookkeeping) and error due to flow suppression (current bookkeeping) along power settings and freestream Mach number. a: Absolute error, N. b: Relative error, %

3.4. CONCLUSIONS

Following the identified limitations, the effect of flow suppression can be preliminary quantified according to the average pressure coefficient at the fan exhaust plane, freestream Mach number and power settings. For the TPS, the incorrect bookkeeping decreases the absolute fan mass flow, gross thrust, ram drag and fan exhaust velocity at low power settings and at high Mach numbers. This decreases the net thrust specially at medium power settings and medium Mach numbers. In the TFN, the effect is more present as the Mach number increases.

This error is compared with the standard instrumentation error by means of an error propagation study together of a Monte Carlo analysis. It is concluded that flow suppression produces a bias error one order of magnitude higher than the standard error and should be corrected for. The proposed error propagation model can be used to evaluate which parameters are critical in the measurement process and which combination allows for a minimized error.

4

NUMERICAL METHODS

The use of Computational Fluid Dynamics for the analysis of engine/airframe integration has rapidly increased in the last years [47]. The complex flow phenomena acting in the engine/pylon/wing interface and the high accuracy requirements were two of the main drawbacks that kept CFD away from the detailed analysis of installation effects. Nowadays, thanks to the increase in computational power, to the availability of public experimental data for validation and to the derivation of new methods for the post-processing of the flow field [48], computational methods allow for the detailed analysis of internal and external intake and exhaust flow. According to Harris [7], the best path leading to good installation performance is the combination of CFD plus experimental studies.

The physical differences between the engine calibration facility and wind tunnel are studied in this chapter through Computational Fluid Dynamics. First the proposed approach is validated in Section 4.1 by means of available experimental data. Then the TPS exhaust flow at different power settings with and without external flow is modelled with focus in the exhaust system. Following the same procedure it is possible to study the Through-Flow Nacelle (the reference condition) at different blockage conditions.

The meshes are created in ICEM CFD ® following the blueprints of the studied configuration or available CAD models. ANSYS® FLUENT is the chosen CFD solver because of reputation solving internal and external flow, the availability of documentation and the possibility of manually post-processing the results.

4.1. VALIDATION: AIAA 1ST PROPULSION AERODYNAMICS WORKSHOP

For the validation of the numerical approach an axisymmetric nozzle (single stream flow) is modelled and simulated through CFD. Its solution will be compared with available numerical and experimental data. Then the TPS and TFN exhaust flow will be analyzed following the same numerical approach.

In 2012 the American Institute of Aeronautics and Astronautics held the first Propulsion Aerodynamics Workshop with the main objective of evaluating and improving the state-of-art nozzle performance prediction [47], [49]. Experimental data of convergent conical nozzles at different nozzle pressure ratios obtained in the 70s [50] was used for the validation and verification of CFD code. One of the presented cases was the determination of the thrust and discharge coefficients through two-dimensional axisymmetric nozzles at different convergence angles.

4.1.1. GEOMETRY

The geometry consists of a 15 degrees axisymmetric nozzle.

4.1.2. DOMAIN

For simplification, the domain is assumed to be axisymmetric. This allows to model and compute only an infinitesimal wedge in 2D that is rotated along the axis of symmetry. Following the steps of [49] and [47] the domain is extended 25 nozzle diameters in the radial direction, and 100 nozzle diameters in the axial direction.

4.1.3. MESH

The geometry needs to be divided in finite elements across which the differential equations are discretized and locally solved. An structured grid is used. Cells have similar typology, the number of connectors with the neighbor's cells are equal for all of them and the cells are almost orthogonal, in the direction of the flow. This improves and accelerates the solution and accuracy of the solver with respect to unstructured grids, reducing the computational memory. In addition the number of elements, its location and its local density can be better defined for the given problem.

Three different meshes are created: baseline (0.12 M cells, $y^+ = 50$), refined (0.16 M cells, $y^+ = 4$) and hyper-refined (0.2 M cells, $y^+ = 1$). The difference is mainly in the number of elements in the exhaust nozzle and its surroundings.

Figure 4.1 shows the blocking approach. 46 Blocks are created in order to properly capture flow phenomena, with special refinement in the nozzle exhaust plane and in the shear layer between internal and external flow. An iterative process is necessary (solution is calculated once, and refinement is done in the region with larger velocity gradients). As a result of the large gradients in the y direction the mesh is stretched in the x direction.

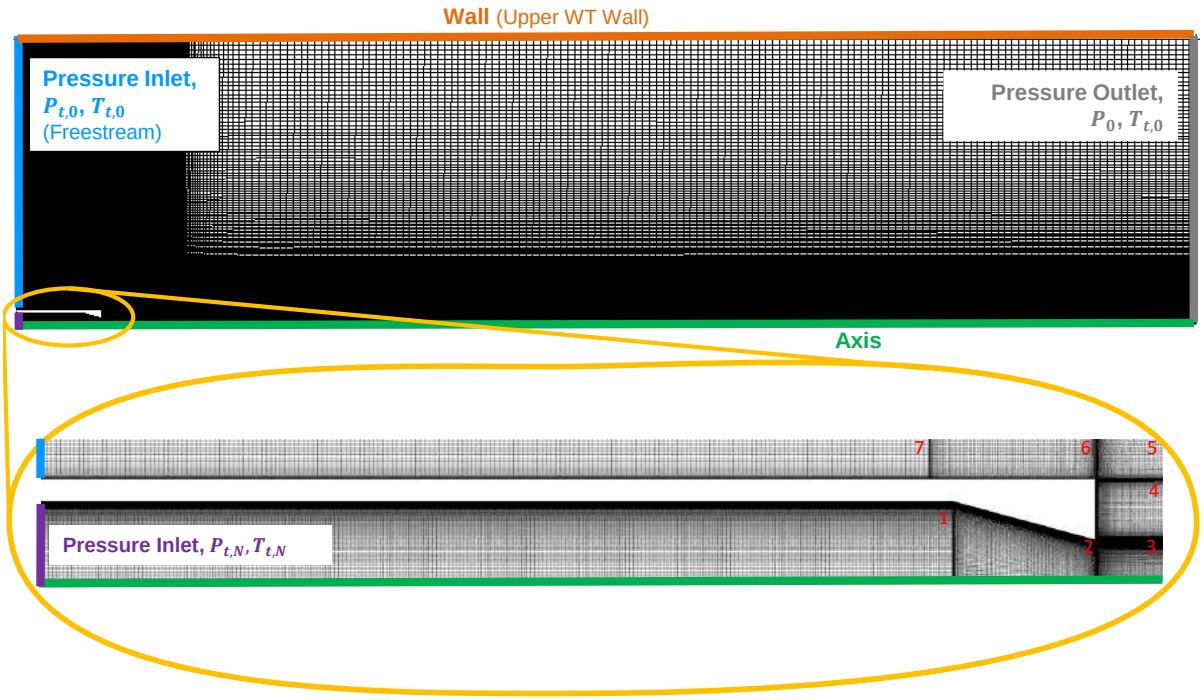

Figure 4.1: Refined mesh of Nozzle in isolation, with the boundary conditions. Zoom in of the Nozzle configuration. In red, the block numbers.

4.1.4. BOUNDARY CONDITIONS

The boundary conditions are set to represent the experimental conditions. These consist of:

- Freestream Pressure outlet: the static pressure P_0 is defined at the outlet of the domain, far downstream as 101300 Pa.
- Freestream Pressure Inlet: The freestream total temperature $T_{t,0}$ and total pressure $P_{t,0}$ are defined. The latter one is set according to the freestream static pressure to define the freestream Mach number M_0 by following isentropic flow equations:

$$\frac{P_{t,0}}{P_0} = \left(1 + \frac{\gamma - 1}{2} M_0^2\right)^{\frac{\gamma}{\gamma-1}} \tag{4.1}$$

The nozzles were tested under quiescent conditions ($M_0 = 0$). However, to guarantee good convergence stability, following the indications of some participants of the workshop [47], [51], a freestream Mach number of 0.01 is set.

- Nozzle Pressure Inlet: the nozzle total pressure $P_{t,nozzle}$ and total temperature $T_{t,nozzle}$ are set at the measurement plane (station where the rakes are placed), according to the required Nozzle Pressure Ratio (NPR). This is defined as:

$$NPR = \frac{P_{t,nozzle}}{P_0} \tag{4.2}$$

- Upper wall: The upper boundary, placed far away of the area of influence, is set as wall to converge and stabilize the solution
- Axis: the domain is axisymmetric along the X axis.

4.1.5. STUDIED CASES

Four different power settings have been computed, following the experimental approach:

- Unchocked conditions, NPR = 1.4
- Just chocked conditions, NPR = 2
- Chocked conditions, NPR = 2.5
- Chocked conditions, NPR = 3

By simulating both chocked and unchocked conditions it is possible to test if the proposed numerical approach can be chosen to model the exhaust of the turbofan power simulator unit.

4.1.6. SOLUTION METHODS

A steady state solution is obtained, where the time marching proceeds until a steady state solution has been reached. It follows an implicit formulation, as in each variable the unknown value in the cell is computed by relating the exiting and unknown value of neighboring cells.

A density-based solver is chosen. The governing equations of continuity, momentum and energy are solved simultaneously. The governing equations for additional scalars are solved in sequence. As these equations are non-linear, several iterations of the solution loop are performed. The continuity equation is used to obtain the density field. Also, a second Order Upwind Spatial Discretization following the Roe-FD Flux type is chosen.

The turbulence is modelled by RANS. Two different turbulence models are compared:

- Spalart-Allmaras: it is a RANS (Reynolds Average Navier Stokes) model that solves the transport equation for a modified eddy viscosity. It is mainly used for aerodynamic applications where separation is not relevant. It is chosen because of its versatility and relatively low computational code.
- Shear Stress Transport: it uses a blending function to gradually transition from the standard $k-\omega$ model near the wall to a high Reynolds number version of the $k-\epsilon$ model outside of the boundary layer. The turbulent viscosity formulation accounts for the transport effects of the turbulent shear stress. It is chosen because of its capability to properly simulate both internal and external flows: on one hand the boundary layer, important in the wall near the fan exhaust plane, and on the other on the shear layer between the plume and freestream flow.

Under these conditions it is possible to accelerate the solution on highly-stretched anysotropic meshes. In order to capture boundary layer effects and flow entraintment the mesh has large aspect ratio cells near wall and the shear layer. In this regions large gradients are expected to be found in the radial direction. Traditionally, the implicit solution method has slow convergence due to small local time steps and slower local rate change of the solution. By accelerating the solution an optimum time step based on the maximum characteristic length of the cell is chosen [52]. As a result the local CFL number is proportional to the cell aspect ratio. The new time step accelerates the solution convergence in cells with Y+ near 1.

4.1.7. CONVERGENCE

Ideally the solution is reached when the discrete conservation equations are obeyed in all cells to a specified solution. As it is not possible determine when the final solution is reached, a convergence criteria is set based on the stability of the solution (it does not change) with subsequent iterations. The convergence criteria is based on:

- Monitoring the residual history, with special attention to the momentum, energy and velocity residuals. Generally, a qualitative convergence is indicated by a decrease in the residuals by three to four orders of magnitude.
- Monitoring the conservation of mass flow along the nozzle. The mass surface integral in the entry and exhaust nozzle face is obtained and compared in each iteration. To achieve convergence the difference in mass flow rate must be smaller than 0.05 %.
- Monitoring the momentum equation along the nozzle. The momentum difference between the entry and exhaust should be the same as the pressure and friction forces inside the nozzle. The momentum imbalance should be smaller than 0.1%.

$$\int_{A_e} \left(P_{A,e} - P_0 + \rho V^2\right) \mathrm{d}A_e - \int_{A_i} \left(P_{A_i} - P_0 + \rho V^2\right) \mathrm{d}A_i = \int_{int} \left(\tau + P_{s,int} - P_0\right) \mathrm{d}A_{int} \tag{4.3}$$

Once the three criteria are set, the solution is assumed to be converged. This is achieved approximately after 5000-8000 iterations according to the case.

4.1.8. POSTPROCESSING

Nozzle coefficients are the main indicators that will be compared with the experiment for the validation of the numerical approach.

The discharge coefficient is obtained as the ratio of the real mass flow, numerically integrated at the nozzle exit, and the ideal mass flow assuming uniform, parallel exit flow at unchoked or choked conditions.

$$C_d = \frac{\dot{m}_{ac}}{\dot{m}_{id}} = \frac{2\pi \int_0^{r_{exit}} \rho\, u\, r\, \mathrm{d}r}{\rho_{id}\, A_{nozzle}\, U_{id}} \tag{4.4}$$

Two different velocity coefficients are obtained.

$C_{v,exit}$ is defined as the velocity coefficient of the nozzle exit plane. F_{exit} is the pressure and pressure force integrated along the nozzle exhaust plane. It represents the internal performance of the nozzle.

$$C_{v,exit} = \frac{F_{exit}}{F_{id}} = \frac{\int_0^{r_{exit}} \left(\rho\, u^2 + (P - P_0)\right) r\, \mathrm{d}r}{U_{id} \int_0^{r_{nozzle}} \rho\, u\, r\, \mathrm{d}r} \tag{4.5}$$

The velocity coefficient $C_{v,total}$ is defined as the ratio of the net thrust and ideal thrust with actual mass flow. It represents the internal performance of the nozzle together with aerodynamic forces acting on the nozzle surfaces (base drag) due to the low external flow speed [47], [49].

$$C_{v,total} = \frac{F_{net}}{F_{id}} = \frac{\int_0^{r_{nozzle}} \left(\rho\, u^2 + (P - P_0)\right) r\, \mathrm{d}r}{U_{id} \int_0^{r_{nozzle}} \rho\, u\, r\, \mathrm{d}r} \tag{4.6}$$

As the base drag is included in the experiment data, the second definition is used as velocity coefficient for the validation, and the first one will be used for the study of the TPS and TFN.

4.1.9. VALIDATION RESULTS

This section validates the grid strategy, the numerical solver settings, the selection of the turbulent model and the post-processing technique by comparing the obtained solution with respect experimental and numerical results available in literature.

MESH INDEPENDENCE STUDY

Figure 4.3 colortudelftb shows the mesh independence study for the discharge and velocity coefficient for unchocked nozzle, NPR = 1.4. It is shown how the result is practically independent from the refined to the hyper-refined mesh, with a relative change smaller than 0.5 %. As a result the refined mesh (0.15 M cells) is chosen. This is a similar mesh size as employed by the participants [53] to the workshop.

QUALITATIVE ANALYSIS

Figure 4.2 show the velocity field for RANS and SST. Qualitatively, differences between both turbulence model are present along the nozzle exhaust plane and shear layer.

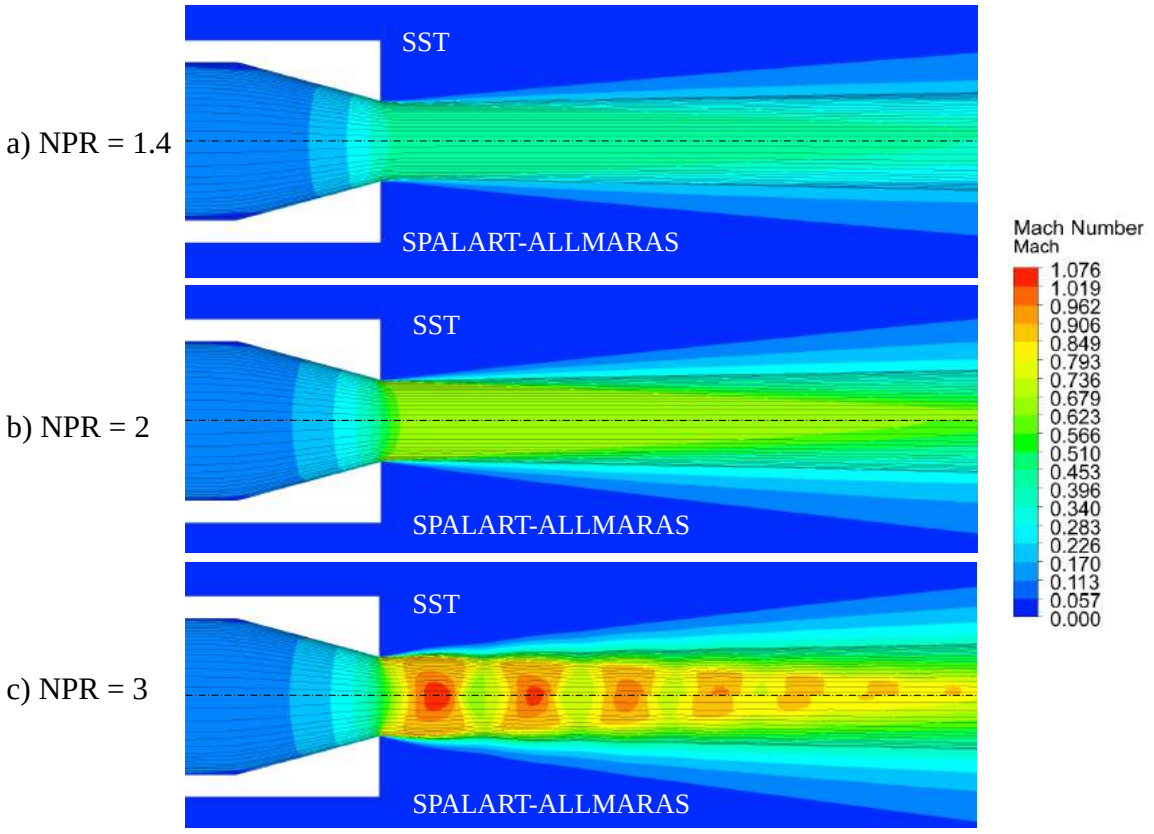

Figure 4.2: Mach contours of nozzle exhaust at different NPR and Turbulence models. **a**: NPR = 1.4, **b**: NPR = 2, **c**: NPR = 3

QUANTITATIVE ANALYSIS

Figures 4.3 a and c compare the discharge and velocity obtained with Spalart-Allmaras and SST, with respect to experimental results and CFD simulations from participants of the Workshop. SST turbulence model reproduces better the boundary layer losses by achieving a discharge coefficient closer to the experiment. Spalart-Allmaras also follows the experimental trend but overestimates the losses of the mass flow and velocity.

As shown in Figure 4.3 d, the differences in the discharge coefficient between the computed SST model and the experiment decrease from 0.5% at low power settings till 0.08 % at high power settings. Differences in the velocity coefficient are of the same order of magnitude but reversed sign. Differences are of the same order of other participants of the workshop such as NASA and Tsinghua University. As a result, the presented approach is validated.

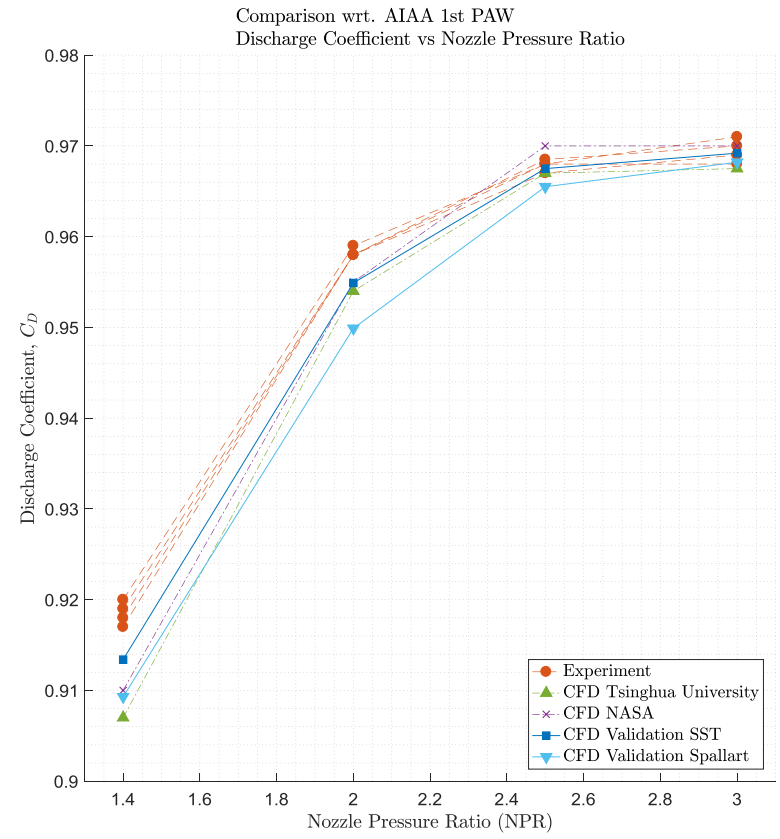

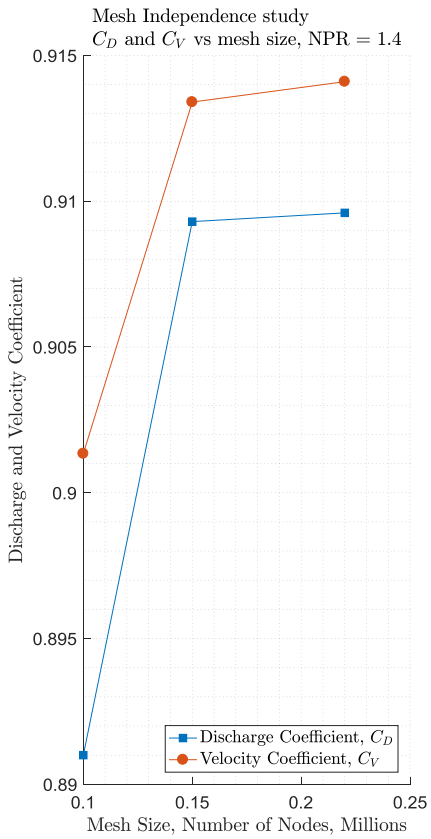

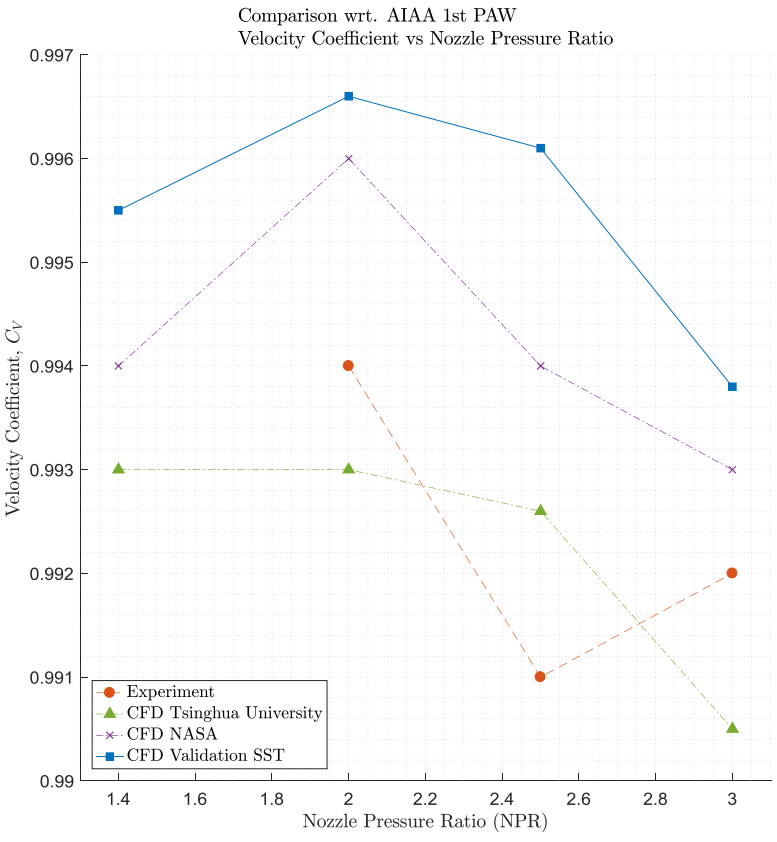

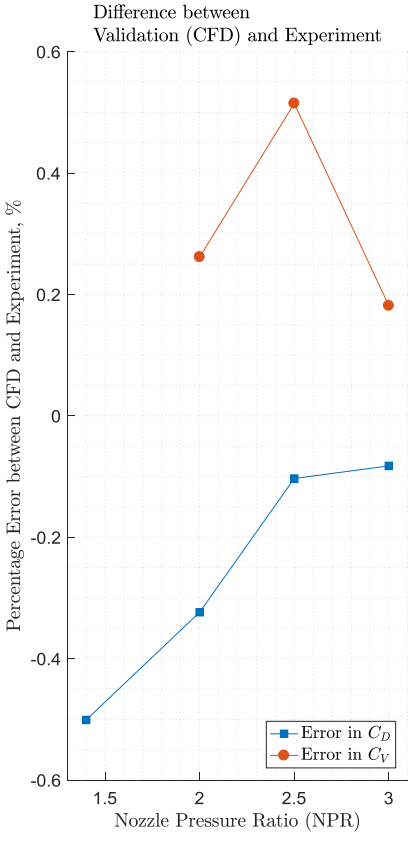

Figure 4.3: Validation of CFD Results. *Source: AIAA [50]* **a**: Discharge Coefficient vs NPR obtained from: Experiment, participants of the AIAA workshop and computed SST and Spalart-Allmaras **b** Mesh Independence study, C_D and C_V vs mesh size for SST model, **c**: Velocity Coefficient vs NPR obtained from: Experiment, participants of the AIAA workshop and computed SST **d**: Relative difference between computed solution in SST and experimental approach along NPR

4.2. TURBOFAN POWERED SIMULATOR

In this section the methodology followed for the numerical analysis of the presented TPS exhaust, with and without external flow, is explained. The TPS exhaust configuration, as most of commercial turbofan engines, consists of a Dual Separate Flow (DSF) Nozzle. Fan and core flows are separate until the turbofan exhaust. Then, the same methodology that was used for the analysis of the conical nozzle can be used, assuming the fan and core two different nozzles that exhaust at freestream conditions.

The TPS exhaust is affected by manufacturing tolerances, assembly imperfections and uncertainty from turbulent flow with swirl generated by the fan and and core, which are unique to each TPS nacelle instrumentation as a whole. As a result the objective is neither to compare numerical results with the calibration neither to present a substitute of the calibration process. This is expected to be necessary in the future to characterize the propulsive unit with the required degree of accuracy.

The objective is to compare the TPS exhaust in quiescent (no freestream air) with wind on conditions to understand the differences and limitations of the current approach that states that the thrust is not affected by the external flow. That is also the reason of several simplifications in the modelling approach that will be explained below.

Looking at previous work, the most recent took place in the AIAA 2^{nd} Propulsion Integration Workshop [51], [54]. The exhaust flow of a turbofan was analyzed without external flow, but in this case experimental data was not available. Also only quiescent conditions were simulated, and no analysis was done in the influence of external flow in the turbofan performance. This previous study is used for guidance o the solver settings, together with the validation of Section 4.1.

4.2.1. GEOMETRY

The cross section geometry of the TPS has been extracted from the CAD representation of the analyzed TPS, as previously shown in Figure 2.1. It is axisymmetric with respect to the axis of rotation, so half of the geometry is represented. As the exhaust system is of interest, only the second half of the turbofan is represented, from the nacelle maximum curvature till the exhaust. Fan and core nozzle start at the location of the measurement rake, where boundary conditions are placed. The final geometry is shown in Figure 4.4. This approach was also followed in the AIAA Workshop which simplifies the modelling approach.

Despite only fan effects are of interest, the core flow must be properly included in order to properly simulate interference effects.

4.2.2. DOMAIN

The domain is extended 320 fan radius downstream and 80 fan radius upward. This is important in order to remove any influence from the boundary conditions in the solution.

4.2.3. MESH

Following the validation, three different structured meshes have also been constructed: the baseline, a refined and an hyper-refined. A multi-block distribution is followed as shown in Figure 4.4, where the cells are refined closer to the fan and core exhaust nozzle. One iteration was necessary in order to refine the shear layer between fan and external flow. The computations were run once and in the region of larger velocity gradients, the blocking was refined. In addition blocks are aligned with the fan and core flow for larger accuracy. The hyper-refined mesh was chosen to perform the calculations with 0.41 million cells.

4.2.4. BOUNDARY CONDITIONS

The boundary conditions follow from the validation:

- Freestream Outlet: the freestream static Pressure is selected according to the ECF Tank static Pressure.
- Freestream Inlet: the total pressure and total temperature is selected according to freestream conditions. In case of calibration conditions, the total pressure will be similar to the static pressure, with a freestream Mach number of 0.01
- Fan Nozzle Entry (fan measurement station): the total pressure and total temperature are selected according to the FNPR and $T_{t,fan}$ at testing conditions, obtained by the rakes at the measurement plane.

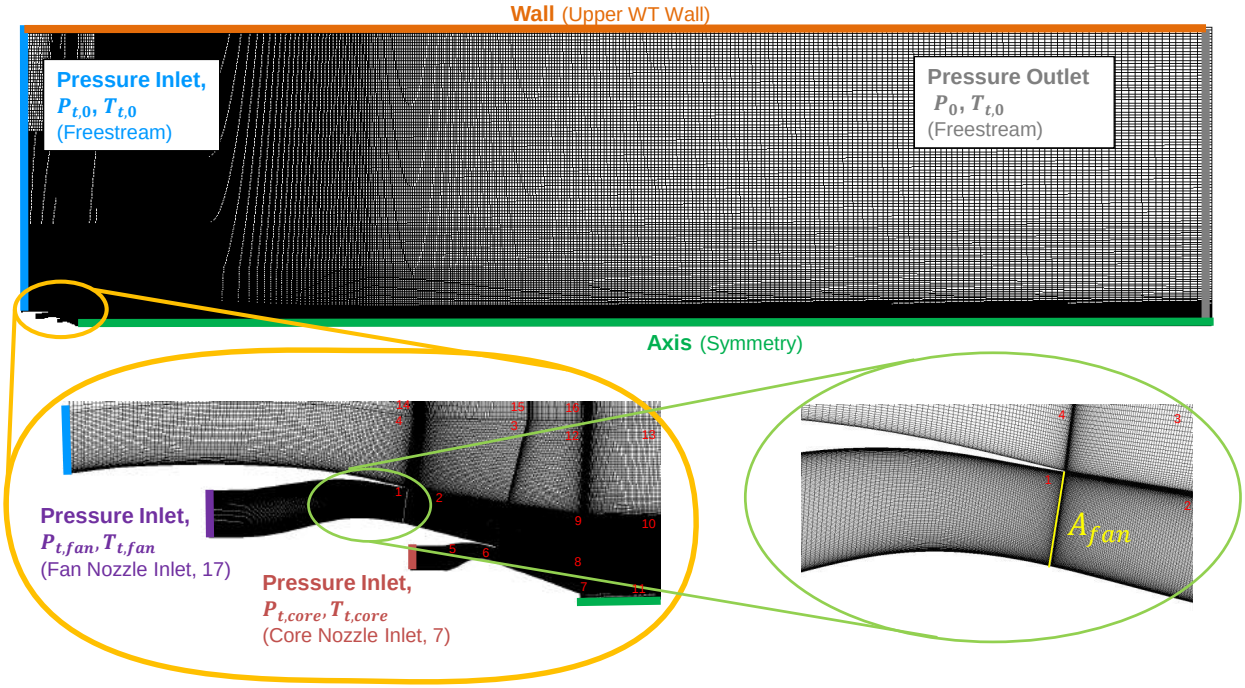

Figure 4.4: Refined mesh of TPS in isolation, with the boundary conditions. Zoom in of the TPS configuration. In red, the block numbers.

- Core Nozzle Entry (core measurement station): the total pressure and total temperature are selected according to the CNPR and $T_{t,core}$ at testing conditions, obtained by the rakes at the measurement plane.
- Upper wall: the upper boundary is placed far away from the region of interest and is set to wall for stabilization of the solution.
- Axis of symmetry: the lower boundary is the X axis of symmetry along which the domain revolves.

4.2.5. SOLUTION METHODS

Following the validation, the steady state solution is obtained by solving the equations with an implicit method through the density based solver. The turbulence is modelled in RANS-SST, with a Second Order Upwind Spatial Discretization.

4.2.6. DESIGN MATRIX

Figure 4.5 shows the analyzed configurations in CFD. The objective is to understand the physical differences between calibration and wind tunnel operating conditions. As a result the analysis is repeated for each point according to the calibration $M_0 = 0,01$. Two different approaches are followed for the selection of the configurations:

- Reproduction of TPS Calibration and Wind tunnel Testing: several cases are chosen according to the calibration and wind tunnel tests that took in 2015. This general approach can be used to analyze the influence of the external flow in the thrust. Also, the comparison of the numerical with the calibration serves as a benchmark for the robustness of the CFD method. The points are represented in Figure 4.5 as red dots, and chosen to range from unchocked to unchocked nozzle.
- Mach sweeps: the freestream Mach number is changed from $M = 0.4$ to $M = 0.82$ at a given power setting (FNPR). Results are compared with the calibration ($M_0 = 0.01$) to understand the effect of the Mach number on the TPS performance. This study is repeated at different FNPR to map the TPS performance in the operating envelope and understand influence of external flow with the power effects. The points are represented in Figure 4.5 as blue dots. In this case, some results reside outside of the performance map, leading to negative thrust. However, the physics are still valid and the analysis provides information regarding the flow at the exhaust.

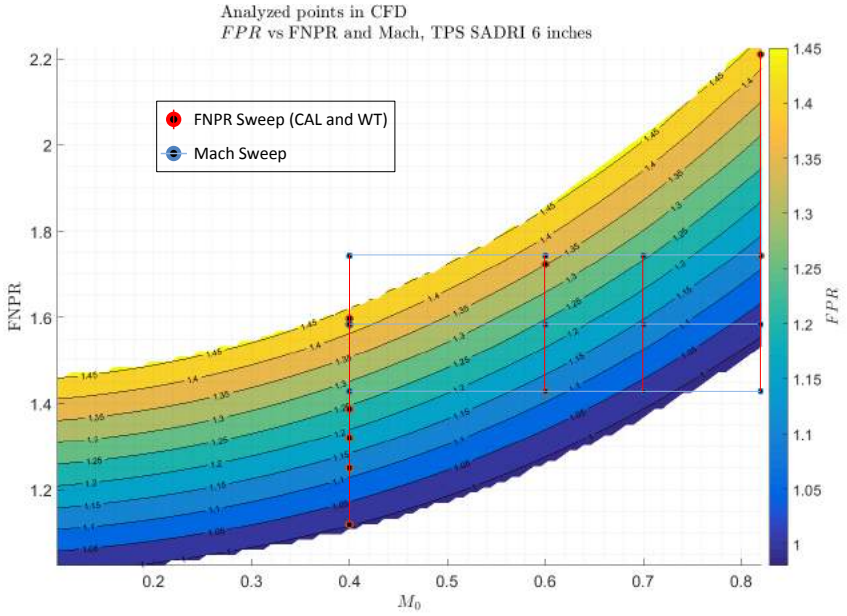

Figure 4.5: Analyzed points on CFD overlaid over TPS performance map, wind tunnel conditions. All points are repeated in equivalent calibration conditions ($M_0 = 0.01$).

4.2.7. POSTPROCESSING

Following DNW standard procedure the fan exhaust plane and core exhaust plane are chosen perpendicular to the core cowling and the plug respectively, as shown in Figure 4.4. As a result the flow exhausts with θ angle of 8 degrees at the fan and 5 degrees for the core. In the case of the exhaust momentum, the component in the x direction is the one of interest for the thrust.

The discharge and velocity coefficient are obtained following the same approach as with the validation, with n_{fan} the number of elements in the fan exhaust plane:

$$C_{D,fan} = \frac{\dot{m}_{fan,ac}}{\dot{m}_{fan,id}} = \frac{\int_{A_fan} \rho \bar{V} \, \mathrm{d}\bar{A}}{\rho_{id} A_{fan}} = \frac{\sum_{i=1}^{n_{fan}} \rho_i \bar{V}_i |\bar{A}_i|}{\rho_{id} A_{fan}} \tag{4.7}$$

$$C_{V,fan} = \frac{F_{G,fan,ac}}{F^*_{G,fan,id}} = \frac{\int_{A_fan} \left(\rho \bar{V} \bar{V} + P - P_0\right) \mathrm{d}\bar{A}}{\dot{m}_{fan,ac} V_{fan,id}} = \frac{\sum_{i=1}^{n_{fan}} \left(\rho_i \bar{V}_i \bar{V}_i + P_i - P_0\right) \bar{A}_i}{\dot{m}_{fan,ac} V_{fan,id}} \tag{4.8}$$

Velocity and pressure profiles are obtained at several stations away from the fan exhaust plane. In addition, the area-weighted average of the pressure at the fan exhaust plane is numerically obtained.

$$P_{fan,e} = \frac{1}{A} \int_{A_{fan}} P \, \mathrm{d}A_{fan} = \frac{1}{A_{fan}} \sum_{i=1}^{n_{fan}} P_i |A_i| \tag{4.9}$$

Then, the pressure coefficient at this location (suppression level) can be calculated:

$$C_{P,fan} = \frac{P_{fan,e} - P_0}{\frac{1}{2} \rho V_0^2} \tag{4.10}$$

The mass-weighted average of the exhaust velocity is obtained at the fan exhaust plane:

$$V_{fan,e} = \frac{\int_{A_{fan}} |V| \rho \bar{V} \, \mathrm{d}\bar{A}}{\int_{A_{fan}} \bar{V} \, \mathrm{d}\bar{A}} = \frac{\sum_{i=1}^{n_{fan}} |V_i| \rho \bar{V}_i \, \mathrm{d}\bar{A}_i}{\sum_{i=1} \bar{V}_i \, \mathrm{d}\bar{A}_i} \tag{4.11}$$

Boattail and scrubbing drag are obtained by integration in the axial direction of the pressure and shear stress in the core cowling:

$$D_{boattail} = \int_{A_{core,cowling}} (P - P_0) \, cos(\theta) \, \mathrm{d}A = \sum_{i=1}^{n_{boattail}} (P_i - P_0) \, cos(\theta_i) \, \mathrm{d}A_i \tag{4.12}$$

$$D_{scrubbing} = \int_{A_{core,cowling}} |\tau| \, cos(\theta) \, \mathrm{d}A = \sum_{i=1}^{n_{boattail}} |\tau_i| \, cos(\theta_i) \, \mathrm{d}A_i \tag{4.13}$$

4.3. BLOCKAGE REPRESENTATION

The pressure field of the wing can be represented as a blockage: as the flow is decelerated in the wing lower surface, it is possible to design a surface that stagnates the flow and increases the static pressure in the longitudinal direction [55], as shown in Figure 4.6

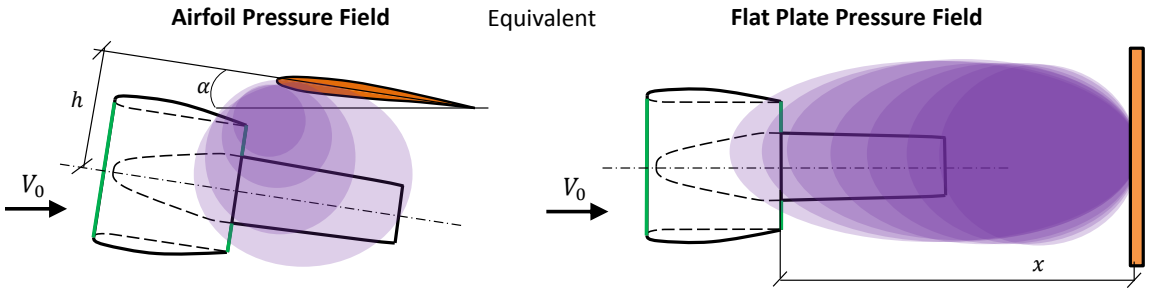

Figure 4.6: Equivalent pressure field between airfoil and flat plate on fan exhaust face

4.3.1. RANKINE HALF-BODY

A first representation of this is achieved in potential flow through the Rankine Half-Body [56]. By superposing an uniform stream of constant speed V_0 and a source of constant strength Λ it is possible to simulate the flow field of around a body, as shown in Figure 4.7.

In red it is shown the streamline that separates external from internal flow defining the Rankine Half body. Stagnation point S is obtained at the axis of the body. In black dotted line it is represented the location of the TFN fan exhaust.

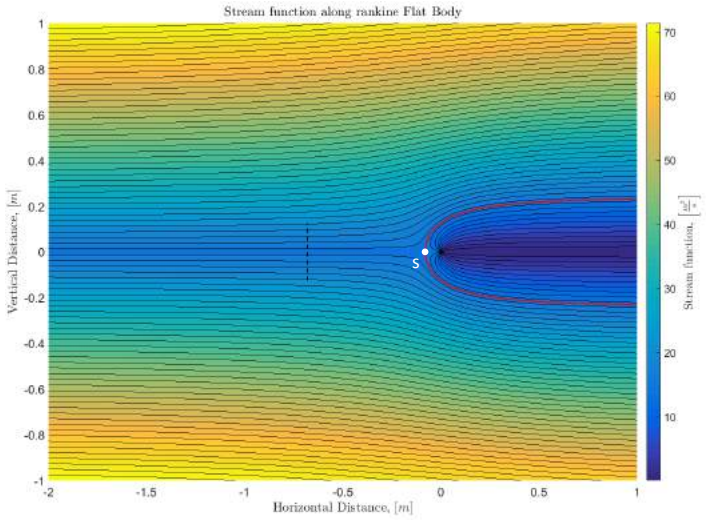

Figure 4.7: Streamline field generated by a Rankine Half Body, in freestream flow, $V_{x,0} = 60\frac{m}{s}$

The potential and stream functions are defined as:

$$\phi_P = V_{x,0}\, x + \frac{\Lambda}{4\pi} ln\left(x^2 + y^2\right) \tag{4.14}$$

$$\psi_P = \frac{\Lambda}{2\pi} atan\left(\frac{x}{y}\right) + V_{x,0}\, y - V_{y,0}\, x \tag{4.15}$$

It is possible to fix source strength Λ so the half body has thickness $D_{Rankine}$.

$$\Lambda = D_{Rankine}\, V_0 \tag{4.16}$$

The velocity field is then:

$$V_x = \frac{\Lambda}{2\pi}\frac{x}{x^2+y^2} + V_{x,0} \tag{4.17}$$

$$V_y = \frac{\Lambda}{2\pi}\frac{y}{x^2+y^2} \tag{4.18}$$

$$|V| = \sqrt{V_x^2 + V_y^2} \tag{4.19}$$

Neglecting compressibility, the pressure field along the centerline can be calculated.

$$C_P = 1 - \frac{|V|}{V_{x,0}} \tag{4.20}$$

4.3.2. VERTICAL FLAT PLATE

The physical equivalence of the Rankine Half Body is a vertical circular flat plate. This is modelled in isolation following the previous approach, at freestream Mach number of 0.22. According to the radius it is possible increase the static pressure at any given longitudinal distance. This will be placed together with the through-flow nacelle in order to understand suppression effects.

4.4. THROUGH-FLOW NACELLE

In order to study idle conditions, the flow-through nacelle is investigated numerically, with and without the blockage previously introduced. Results from the simulation will be used to better define an experiment that will validate the proposed thrust/drag bookkeeping method.

4.4.1. GEOMETRY

The cross section is created in CATIA from blueprints available from the calibration report [35]. The freestream air flows only through the fan duct as the core is blocked. In this case both intake and exhaust must be modelled. The model is assumed to be axisymmetric along the x axis.

4.4.2. DOMAIN

The domain is extended 140 and 87 fan radius upstream and downstream respectively. The upper wall is placed far away in order to avoid interference effects. The blockage is located at different longitudinal distances from the fan exhaust.

4.4.3. MESH

The structure mesh is divided in 102 blocks, with special attention to the refinement of the fan intake and exhaust. The external nacelle is surrounded by a c-mesh. The converged mesh consists of 0.37 million cells.

4.4.4. BOUNDARY CONDITIONS

Due to the nature of the through flow nacelle the boundary conditions are simplified in this case to:

- Freestream inlet: Total pressure and total temperature are set.
- Freestream outlet: static pressure is set. The freestream Mach number is obtained from isentropic relations
- Upper wall
- Axis of symmetry, through which the domain revolves

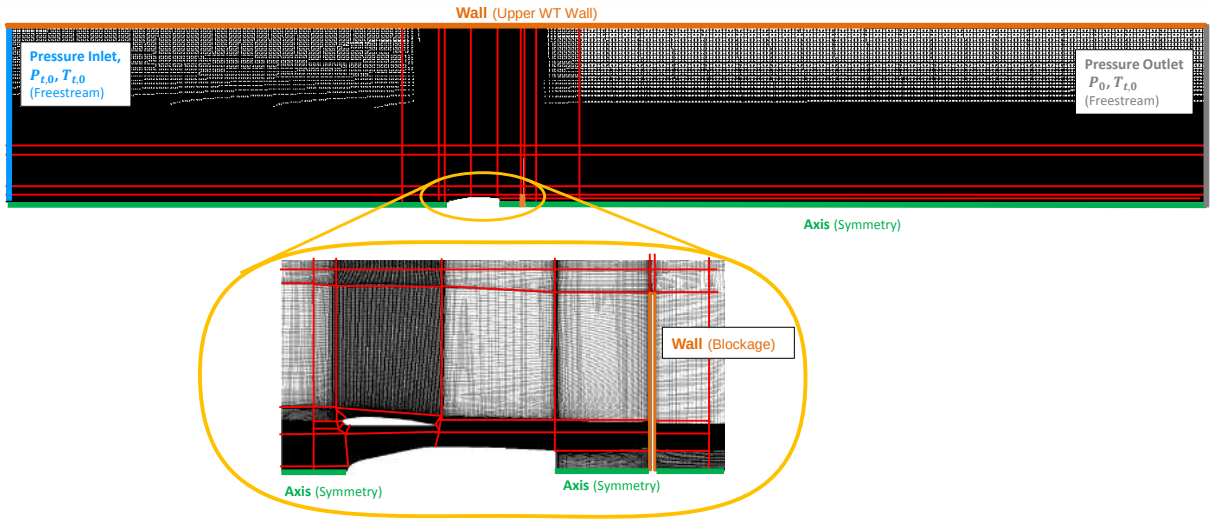

Figure 4.8: Refined mesh of TFN in isolation, with the boundary conditions. Zoom in of the TFN geometry. In red, the blocking structure.

4.4.5. SOLUTION METHODS

The steady state solution is obtained by solving the equations with an implicit method through the pressure based solver. The turbulence is modelled in RANS-SST, with a Second Order Upwind Spatial Discretization.

4.4.6. DESIGN MATRIX

The effect of a blockage at different locations is studied. The objective of the CFD is to understand the influence of the flat plate on the fan flow and boattail drag. As a result the simulated cases involv the isolated configuration and a combination of flat plate distance to the fan and size to achieve the desired suppression level, as shown in Table 4.1. The largest flat plate radius and the closest distance to the fan exhaust introduces the highest suppression effect.

Table 4.1: My caption

CASE	Flat Plate Radius [mm]	Flat Plate Distance to Fan [mm]	Description
1	-	-	Isolated TFN
2	0.25	100	Low Suppression
3	0.25	0.6	Medium-Low Suppression
4	0.25	0.5	Medium-High Suppression
5	0.5	0.6	High Suppression

4.4.7. POSTPROCESSING

The fan discharge and velocity coefficient are obtained as explained in Section 4.2.7. The flow exhaust angle is 0 degrees. In addition the boattail and scrubbing drag are obtained according to equations 4.12 and 4.13 respectively.

4.5. CONCLUSIONS

A validated numerical approach has been introduced for the analysis of the TPS and TFN exhaust flow in calibration and wind tunnel conditions. The approach follows the definition of an axisymmetric domain by means of a multi-block approach. The converged meshes are refined in the fan and core exhaust plane, core cowling and shear layer between internal and external flow.

By means of a second order upwind discretization scheme, the equations of the fluid are numerically solved modelling the turbulence in RANS-SST. The density-based solver is selected for the TPS, and the pressure-based solver for the TFN. In this second case, a vertical flat plate is located downstream to stagnate the flow and simulate the higher than freestream pressures that are present in the installed configuration.

5

NUMERICAL RESULTS

In this chapter the results from the numerical study are detailed and placed into the context of the research. The analysis is done in Section 5.1 for the TPS (powered conditions) and in Section 5.2 for the Flow-Through Nacelle (idle conditions). The analysis is compared with the theoretical model introduced in Section 3.1 and will provide insight regarding the proposed bookkeeping method and the design of the experiment.

5.1. TURBOFAN POWERED SIMULATOR

This section introduces and analyzes the numerical results of the TPS exhaust according to Section 4.2.

5.1.1. COMPARISON WITH ENGINE CALIBRATION FACILITY

A first step to evaluate the accuracy and consistency of the results is by comparing the values of the discharge and velocity coefficient obtained at quiescent conditions (Mach 0.01) with those obtained at the Engine Calibration Facility. The objective of this numerical analysis is not to reproduce the results of the ECF, but to evaluate the differences between the calibration and wind tunnel conditions, this first analysis serves as a benchmark of the solver.

Figure 5.1 a shows the discharge coefficient vs the nozzle pressure ratio at different simulated Mach numbers for both numerical and experimental approaches. Despite the simplifications, differences between both procedures range from -1.6% at low power settings, till -0.2% at chocked conditions. The increase of the discharge coefficient with the power settings is the same trend followed at the validation, with the numerical approach in this case also overestimating the mass flow losses. Also, as in the case of the conical nozzle, difference between numerical and experimental approach are reduced as the power settings increases. With a FNPR of 2.21, the chocked flow (where shockwaves are present) fixes the mass flow and reduces the numerical error. However, the current simplified model can not explain the difference in trend.

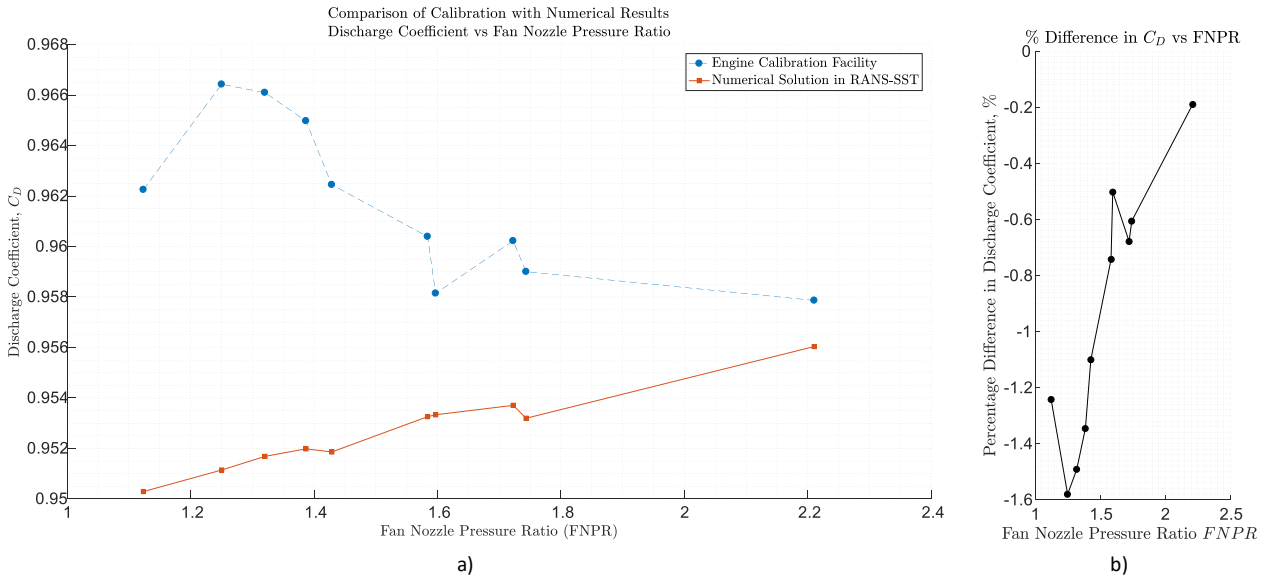

Figure 5.1: **a**: Discharge Coefficient vs FNPR for experimental calibration of TPS unit in the ECF and numerical calculations. *Source: DNW TPS Calibration Report* **b**: Relative Difference in the Discharge Coefficient between experimental and numerical calculations

5.1.2. INFLUENCE OF MACH NUMBER AND POWER CONDITIONS

The following subsection compares the TPS fan exhaust performance between calibration and wind tunnel conditions. The analysis will provide insight regarding the development of a new bookkeeping approach.

Figures 5.2 and 5.3 compare the Mach and pressure fields of the TPS at a FNPR = 1.74, at different freestream conditions from $M_0 = 0.01$ (Calibration) to $M_0 = 0.82$ (Wind tunnel, cruise). The differences increase with Mach number. The shear layer (interface between the exhaust plume and freestream flow) decreases in size with the external velocity as the difference in velocities between plume and free air is decreased. As a result the flow spreading rate, the exchange in velocity between the plume and the medium, decreases with the freestream Mach number. This changes the development of the fan exhaust jet and increases the static pressure in the fan jet, as shown in Figure 5.3. These higher than freestream pressures are stronger with the Mach number.

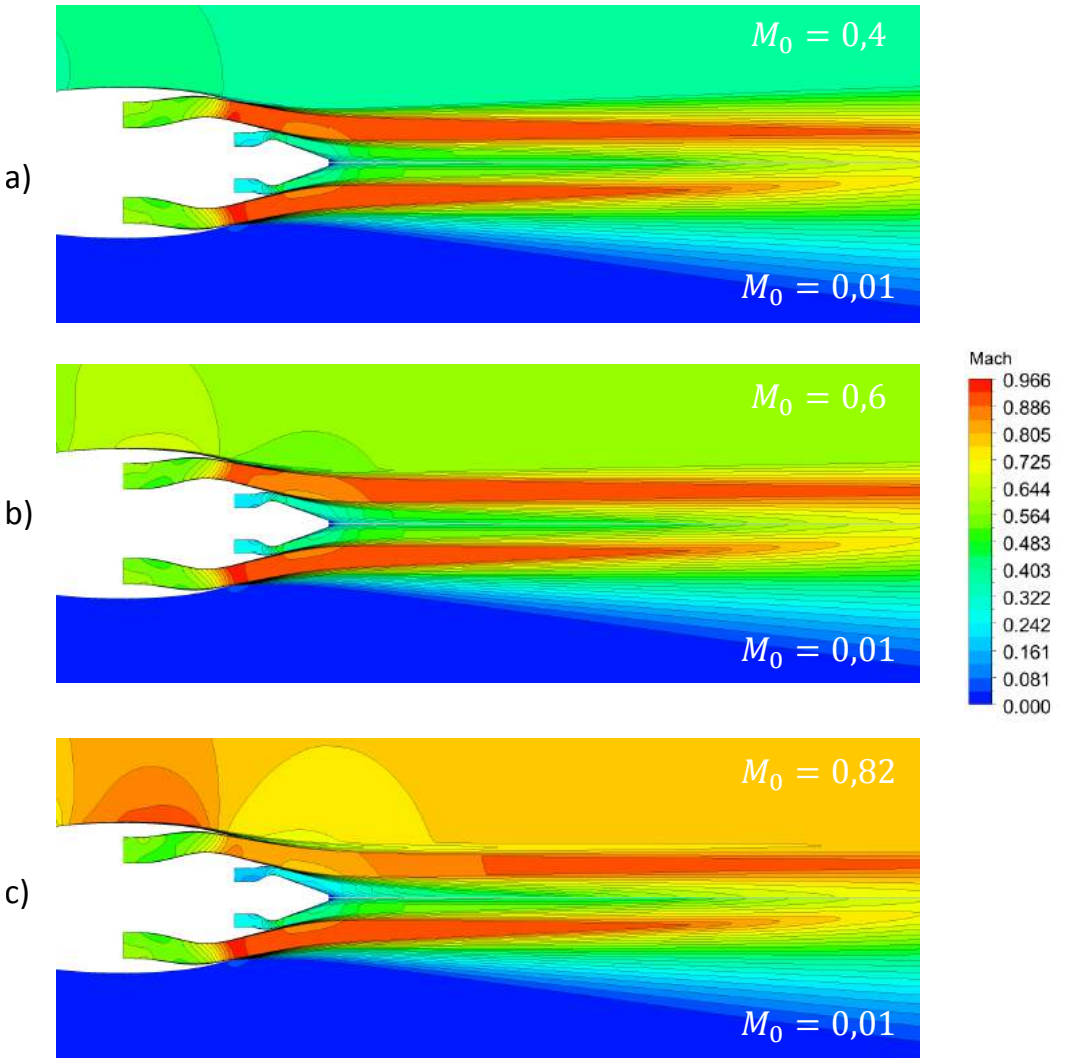

Figure 5.2: Mach field of TPS exhaust with and without external flow, at $FNPR = 1.74$. **a**:$M_0 = 0.4$ and $M_0 = 0.01$ **b**: $M_0 = 0.6$ and $M_0 = 0.01$ **c**: $M_0 = 0.82$ and $M_0 = 0.01$

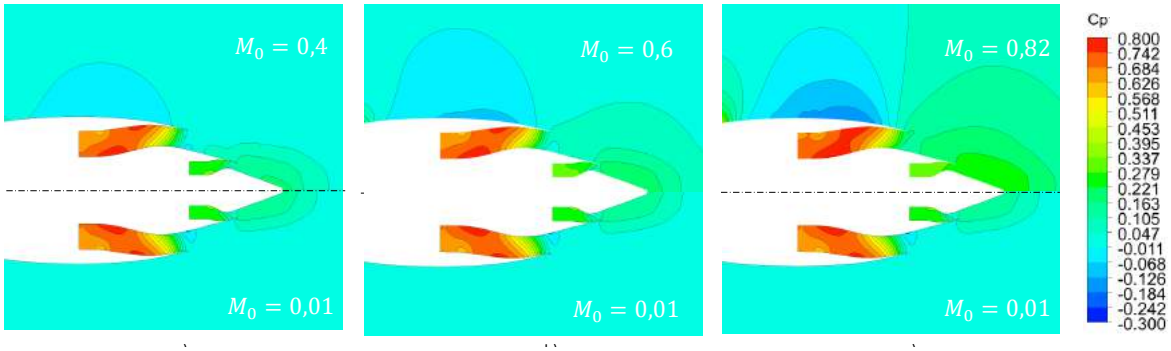

Figure 5.3: Pressure Coefficient field of TPS exhaust with and without external flow, at $FNPR = 1.74$. **a**: $M_0 = 0.4$ and $M_0 = 0.01$ **b**: $M_0 = 0.6$ and $M_0 = 0.01$ **c**: $M_0 = 0.82$ and $M_0 = 0.01$

As shown in Figure 5.4 the freestream Mach number linearly increases the pressure coefficient at the fan exhaust plane, which is numerically obtained from the CFD solution according to equations 4.9 and 4.10. This pressure increase is practically speaking independent of the power settings. Its origin is the difference in spreading rate and it triggers the decrease in fan mass flow and exhaust velocity.

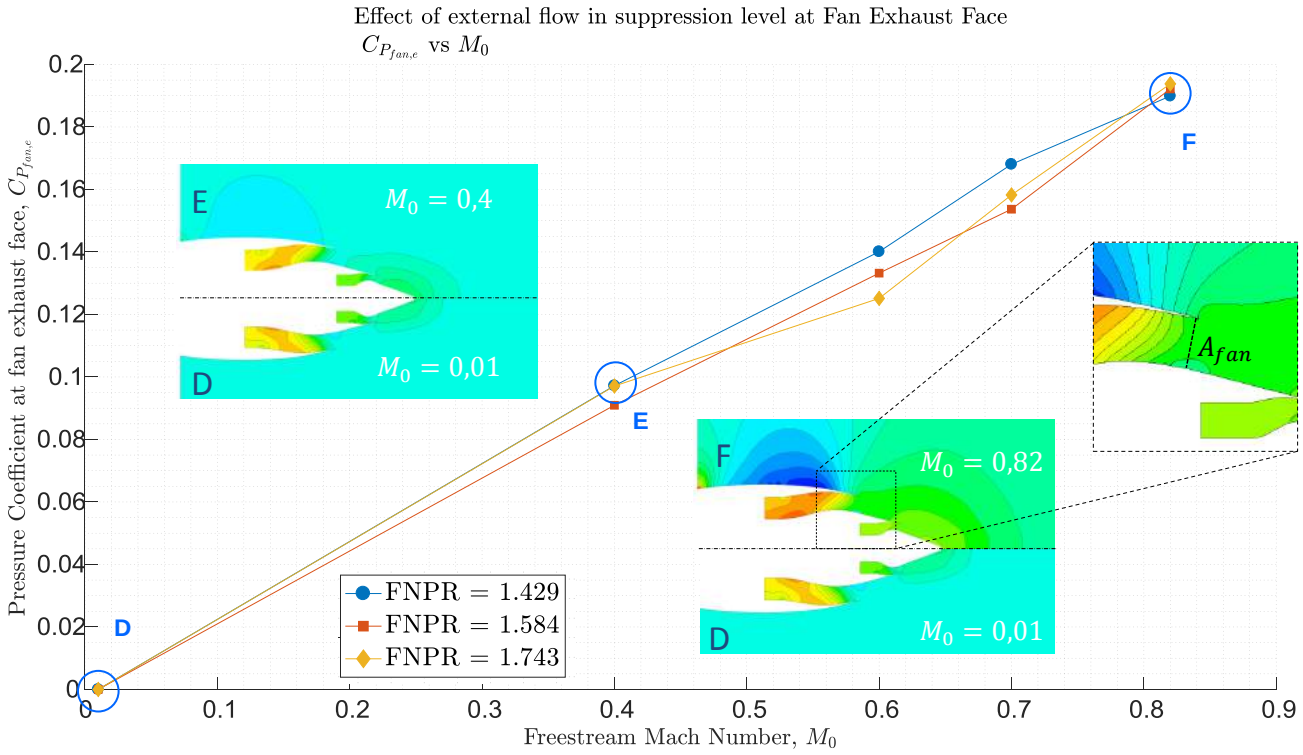

Figure 5.4: Influence of Freestream Mach on the Average Pressure Coefficient and the fan exhaust face

Figure 5.5 shows the decrease in fan mas flow a and exhaust velocity b due to the freestream Mach number from Calibration $M_0 = 0.01$ to transonic $M_0 = 0.82$. The analysis is done at given power settings: $FNPR = 1.429$, $FNPR = 1.584$ and $FNPR = 1.743$. It is shown that the effect of suppression is higher at low power settings and only increases with the Mach number.The decrease in exhaust velocity M_{fan} suppose a problem as this is generally the simulation parameter with respect to the full scale aircraft. The TPS power settings should be increased in order to reach the desired M_{fan}.

The ideal mass flow and exhaust velocity has also been calculated following the mathematical model of Section 3.1, represented by the dotted line. It accounts for the external pressure $C_{P,fan}$ obtained in the CFD fan exhaust plane. The equivalence between theory and numerical results validate the proposed CFD analysis. The offset between both represent the velocity and discharge coefficient. Note how the offset in the mass flow is higher than in the velocity, corresponding to the lower discharge coefficient with respect to the velocity coefficient.

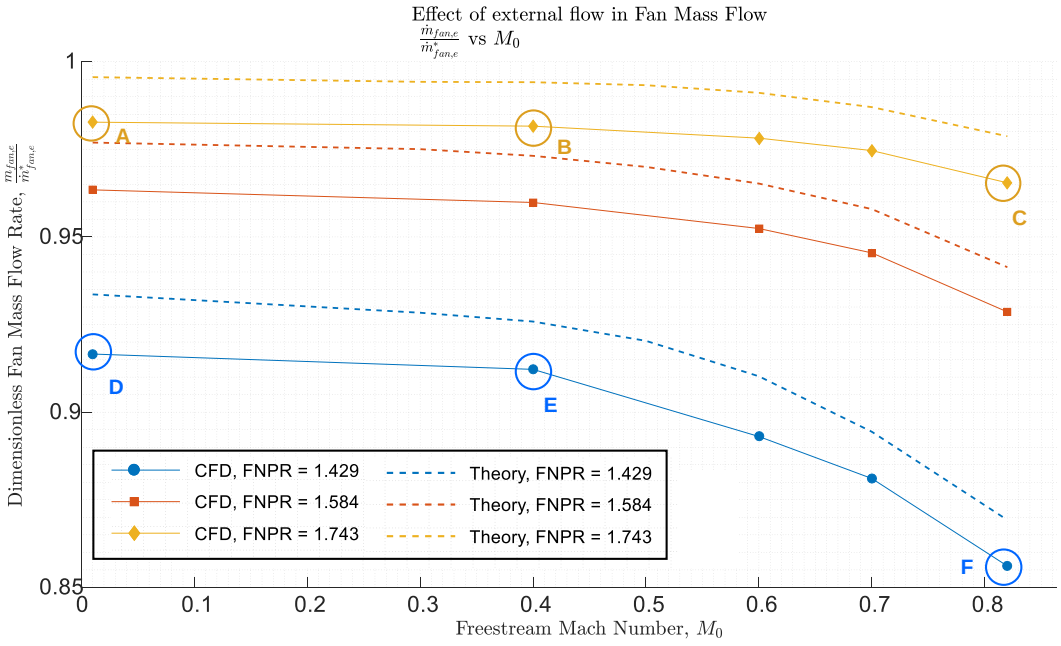

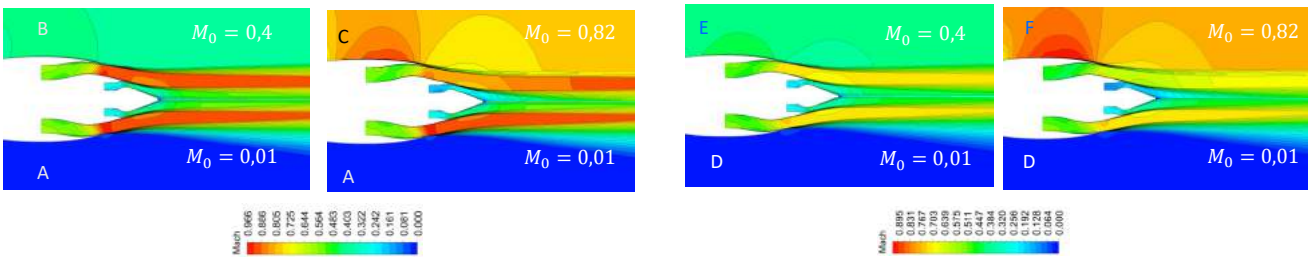

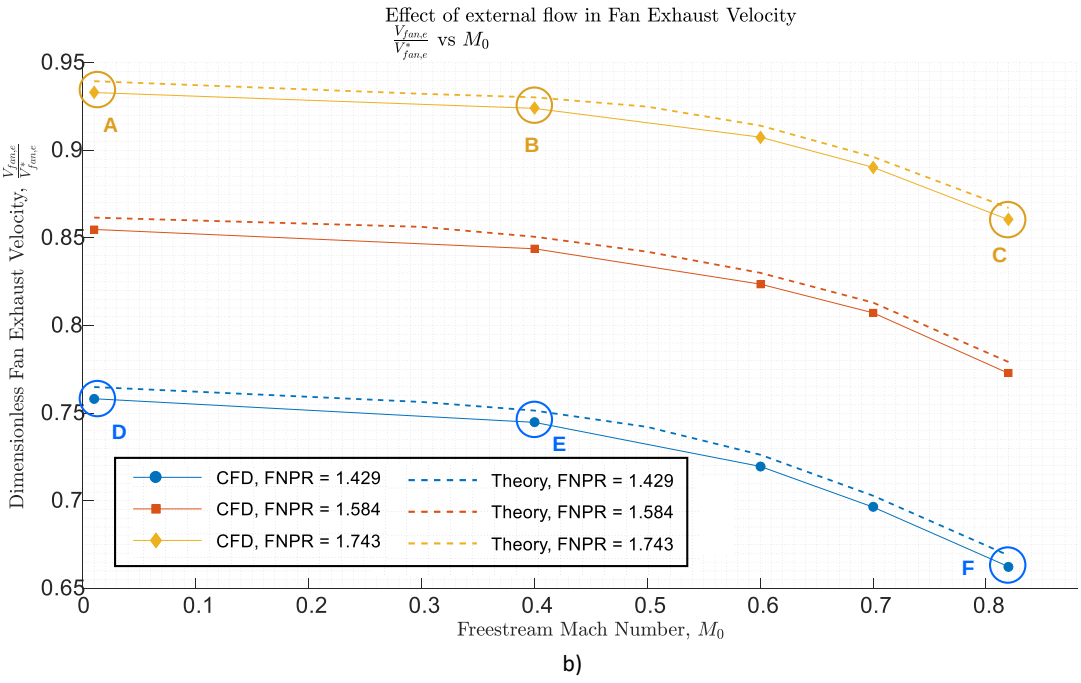

Figure 5.5: Influence of Freestream Mach and Power settings on conditions at the fan exhaust plane. **a**: Fan mass flow vs freestream Mach number at different power settings ($FNPR$) **b**: Fan exhaust velocity vs freestream Mach number at different power settings ($FNPR$)

5.1.3. CHANGE IN BOOKKEEPING METHOD

Once the physics at the exhaust has been understood, the next step is to find the best bookkeeping approach.

CHANGE IN DISCHARGE COEFFICIENT

Figure 5.6 a shows in blue the CFD discharge coefficient according to static calibration ($M_0 = 0.01$).

$$C_{D,fan}^{0,CAL} = \frac{\dot{m}_{fan,ac}^{CAL}}{\dot{m}_{fan,id}^{0}} \tag{5.1}$$

In orange, the CFD discharge coefficient is shown for the same configurations but for wind tunnel conditions, $M_0 = 0.4, 0.6 and 0.8$, following the current bookkeeping approach.

$$C_{D,fan}^{0,WT} = \frac{\dot{m}_{fan,ac}^{WT}}{\dot{m}_{fan,id}^{0}} \tag{5.2}$$

The current bookkeeping method assumes that the ideal mass flow $\dot{m}_{fan,id}^{0}$ is the same during the calibration and in wind tunnel conditions, as a it calculated according to the freestream fan nozzle pressure ratio, $FNPR_0$. However, with freestream flow the TPS fan mass flow, $\dot{m}_{fan,ac}$ is decreased due to flow suppression, as it has been explained in previous sections. The proposed approach is to calculate the wind tunnel ideal fan mass flow in function of the local fan nozzle pressure ratio $FNPR_{loc}$. The discharge coefficient obtained with this new mass flow is represented in green, and is equivalent to the obtained in calibration conditions:

$$C_{D,fan}^{e,WT} = \frac{\dot{m}_{fan,ac}^{WT}}{\dot{m}_{fan,id}^{e}} = C_{D,fan}^{0,CAL} \tag{5.3}$$

In the wind tunnel, the actual mass flow must be obtained according to the discharge coefficient obtained in the calibration, $C_{D,fan}^{0,CAL}$, and the ideal mass flow accounting for flow suppression, $C_{D,fan}^{e,WT}$:

$$\dot{m}_{fan,ac}^{WT} = C_{D,fan}^{0,WT} \quad \dot{m}_{fan,id}^{e} \tag{5.4}$$

CHANGE IN VELOCITY COEFFICIENT

The same occurs with the velocity coefficient, as shown in Figure 5.6 b. When corrected for the reduced mass flow, the value obtained in CFD for wind tunnel conditions shifts back to the original obtained in calibration conditions. The exhaust velocity is considered to be expanded to freestream conditions in both cases. Then, the fan momentum (gross thrust) should be obtained as:

$$F_{G,fan,ac} = C_{V,fan}^{0,WT} \quad \dot{m}_{fan,ac}^{WT} \quad V_{fan,id}^{0} \tag{5.5}$$

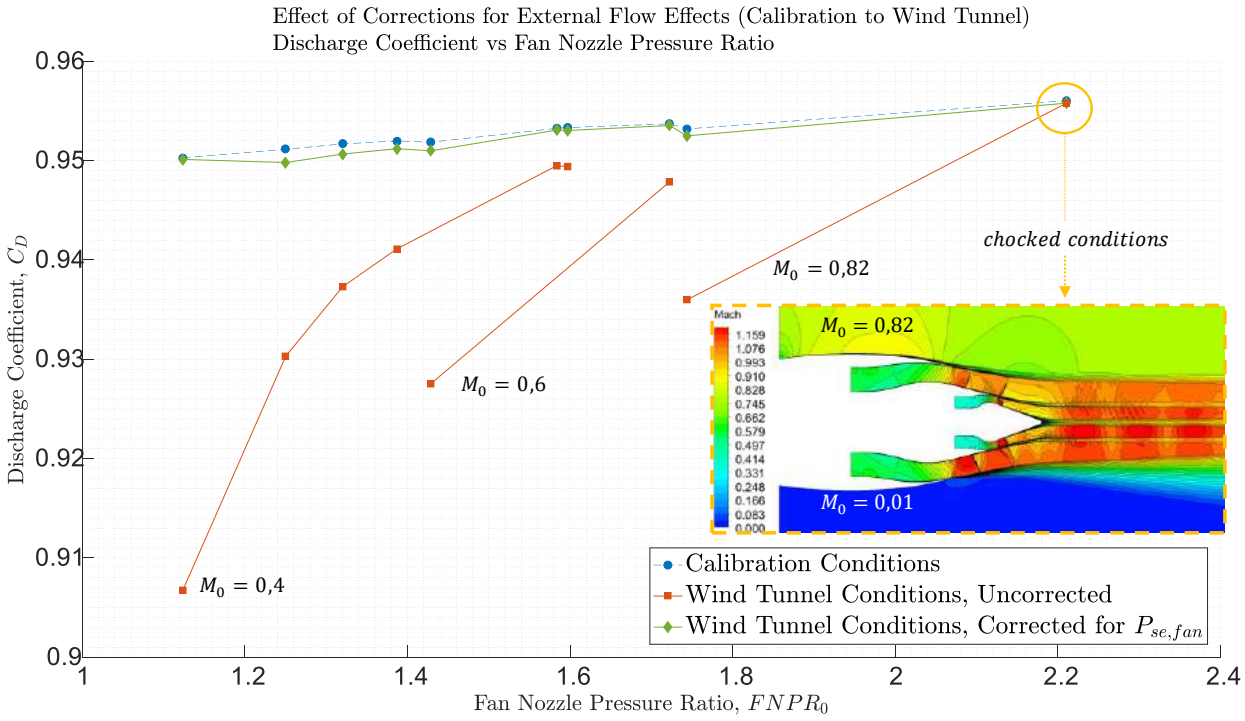

a)

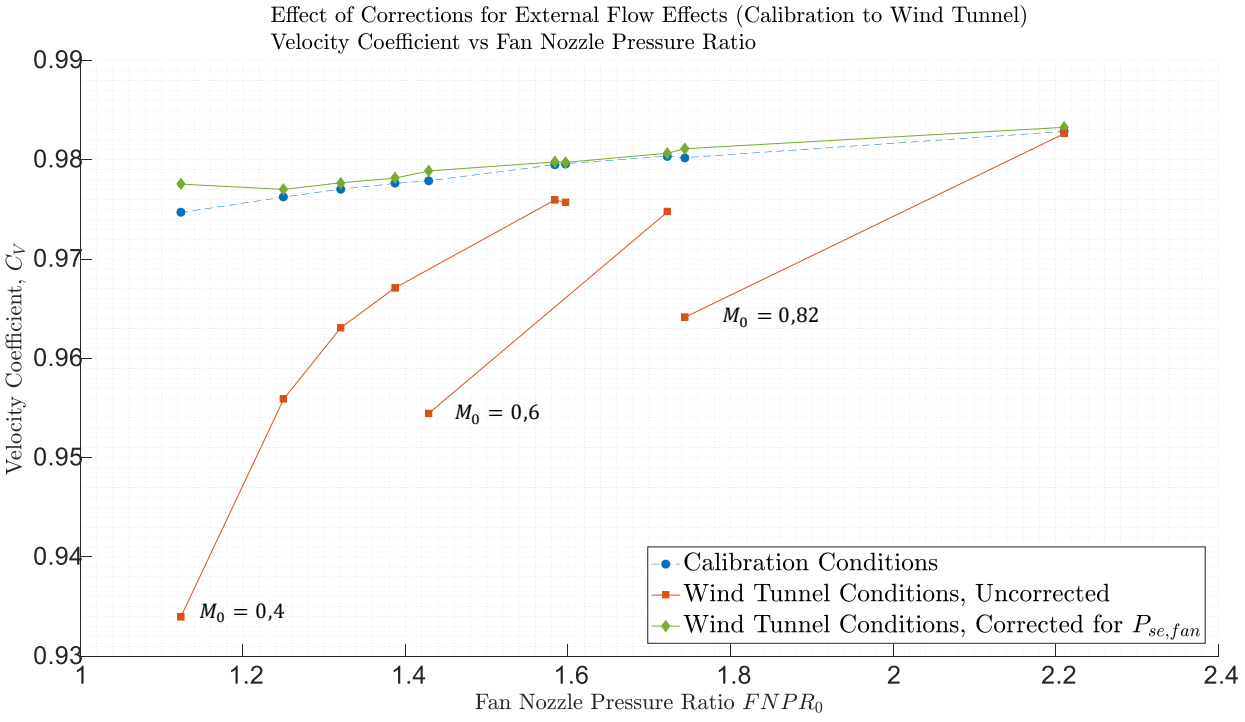

b)

Figure 5.6: Correction to deal with the differences between calibration and wind tunnel conditions for: **a**: Discharge Coefficient **b**: Velocity Coefficient

5.1.4. CHANGE IN BOATTAIL AND SCRUBBING DRAG

The boattail and scrubbing drag have been obtained as a function of the Mach number and Power Settings. The increase in external pressure in the fan exhaust plane with the freestream Mach number is directly proportional to the increase in the pressures along the core cowling. Due to the geometry, these forces have a net effect in the direction of thrust (negative boattail drag). Its effect can be important especially at high Mach numbers. However, in combination with the wing the boattail will be different, and this case should be studied with more detail.

As the plume velocity is decreased with the Mach number, the scrubbing drag (friction drag in the cowling wall) is also decreased. This change is small compared with the change in boattail drag.

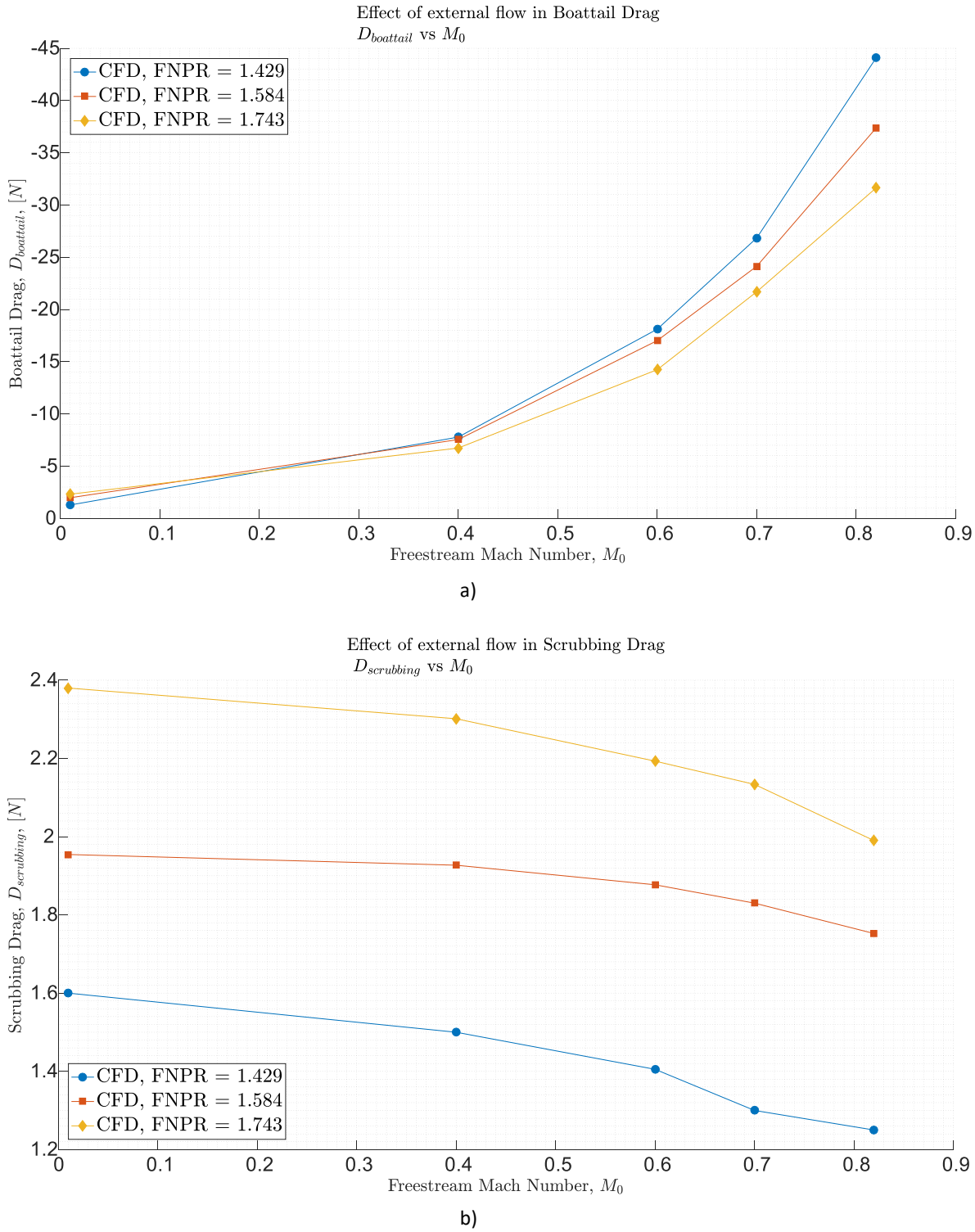

Figure 5.7: Correction to deal with the differences between calibration and wind tunnel conditions for: **a**: Discharge Coefficient **b**: Velocity Coefficient

5.2. FLOW THROUGH NACELLE

In the following section the numerical results of the analysis of the Through-Flow Nacelle are introduced.

5.2.1. EFFECT OF FLAT PLATE

Figure 5.8 a shows the pressure coefficient along the symmetry plane for different circular flat plate sizes in isolation simulated in CFD and the Rankine Half Body, for $M_0 = 0.22$. By using the pressure coefficient the pressure is independent of the freestream velocity. Also, it has been found a dimensionless length $x^* = \frac{x}{\sqrt{A}}$ that makes the distribution independent of the flat plate size. By placing the TFN fan exhaust in the desired location it is possible to simulate any desired suppression level.

In the same figure, the points represent the weighted average pressure coefficient $C_{p,e,fan}$ obtained in the TFN fan exhaust plane (station 19), at the given location $\frac{x}{\sqrt{a}}$ from flat plate. An offset follows from the pressure coefficient of combined TFN+flat plate with respect to the isolated flat plate. The value of the offset has been found to be equal to the pressure coefficient at the TFN fan exhaust plane in isolation, without flat plate ($C_{p,fan} = 0.148$). This demonstrates that the effects of the blockage and freestream flow in increasing the fan exhaust static pressure can be superimposed:

$$C_{p,fan,e} = C^{Mach}_{p,fan,e} + C^{Blockage}_{p,fan,e} \tag{5.6}$$

This is valid for the case of the flat plate but even in this case the offset is not perfect as small interference effects can be found. When a wing is analyzed, interference effects will be stronger, making equation 5.6 no longer valid.

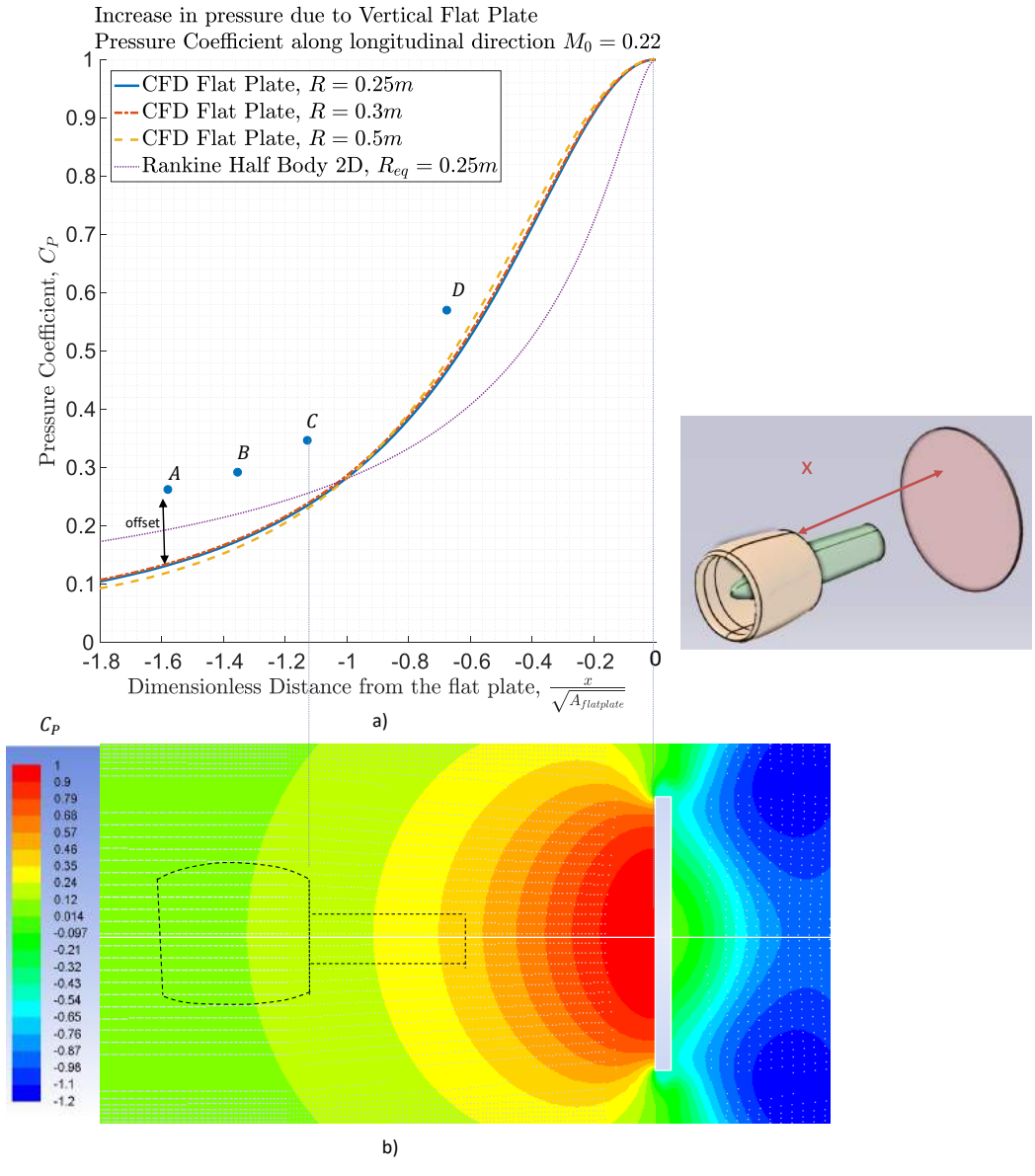

Figure 5.8: **a**: Pressure coefficient along the centerline for different flat plate sizes obtained in CFD and Potential Flow. Points represent the pressure coefficient at the TFN fan exhaust plane with the flat plate located $\frac{x}{\sqrt{A}}$ from station 19 **b**: Pressure Coefficient field obtained in RANS-SST generated for an isolated flat plate of Radius 0.25m

5.2.2. DIFFERENCE IN SUPPRESSION LEVEL

Figure 5.9 shows that the TFN dimensionless mass flow, a, and exhaust velocity, b are decreased as a result of the suppression level generated by the position and size (dimensionless distance) of the flat plate. The linear increase is also expected by the mathematical model of Section 3.1 (dotted line). This decrease can be detected by placing static pressure sensors in the fan exhaust plane or even upstream in the TFN intake.

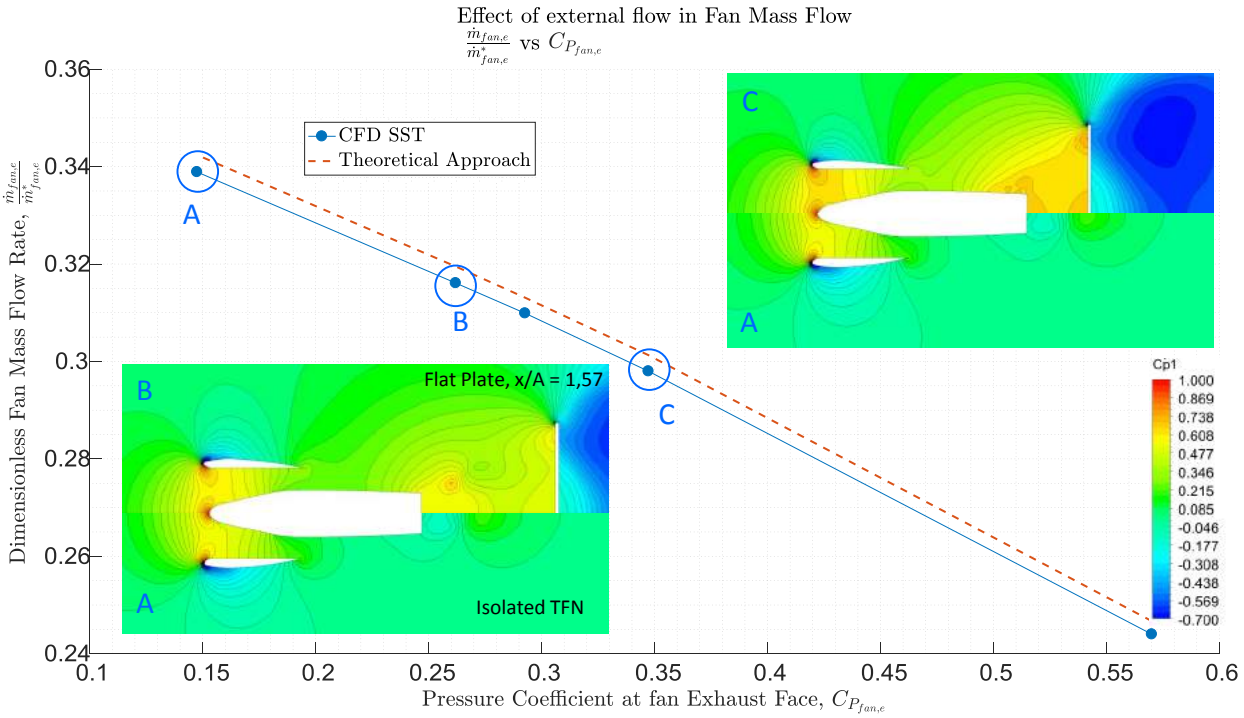

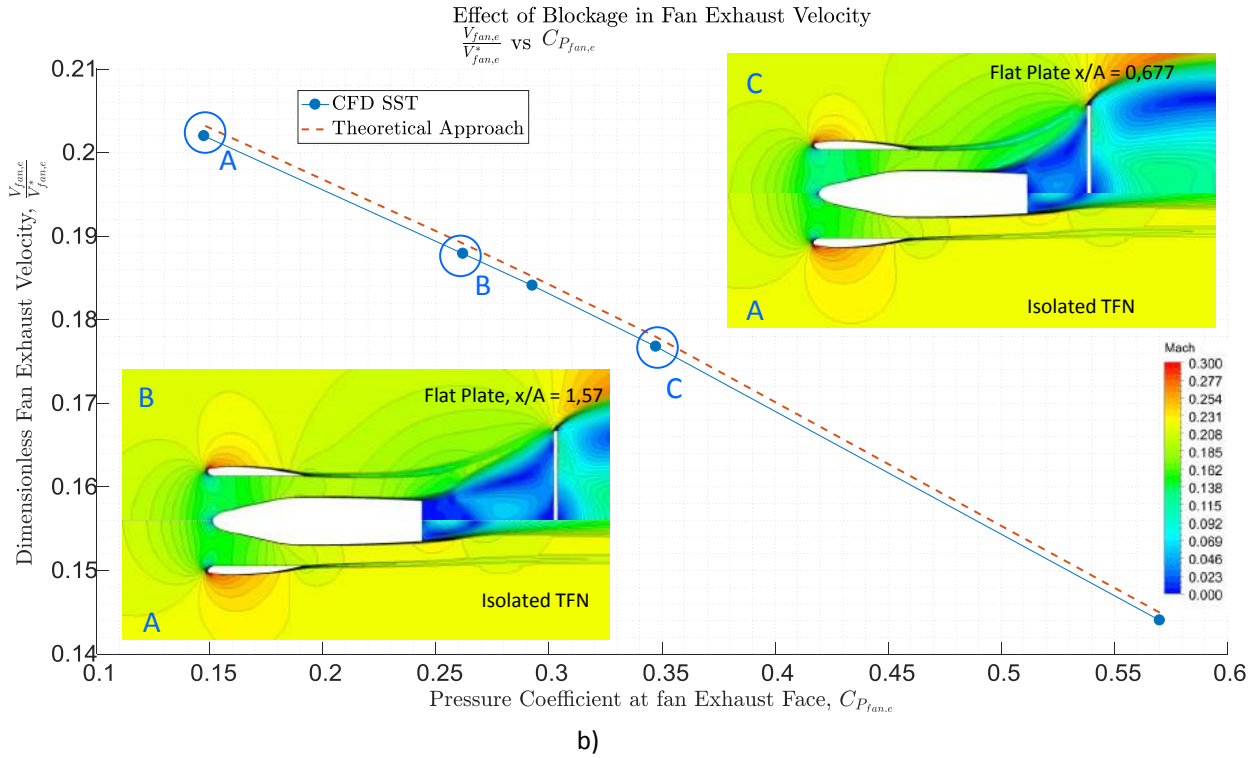

Figure 5.9: Influence of Suppression Level (blockage location) at the fan exhaust plane of the TFN in: **a**: Fan mass flow **b**: Fan exhaust velocity

5.3. CONCLUSIONS

Differences in the TPS Mach and pressure fields have been obtained between calibration and wind tunnel conditions at different power settings. The differences in flow spreading rate due to the difference in shear layer modifies the exhaust conditions with respect to calibration increasing the external pressure. This reduces the fan mass flow and exhaust velocity, changing the performance of the TPS. The influence of the external flow is more important at low power settings, and decreases with the FNPR till chocked conditions are reached, where the freestream velocity has no influence in the TPS performance.

As a result of the change in operating point, the introduced bookkeeping following the Jones Thrust must be followed. The actual mass flow should be obtained with the calibration discharge coefficient and the ideal mass flow accounting for local conditions. If the exhaust velocity is the simulating parameter, the power settings of the TPS must be increased to match the quiescent one.

The analysis of the TFN allows for the study of higher than freestream pressure fields acting on the fan exhaust. At idle conditions this effect is maximized. The increase in pressure due to the influence of the flat place reduces the mass flow and exhaust velocity. Superposition can be assumed by combining the independent effects of the external flow and flat plate.

Finally, in both TPS and TFN the numerical solution follows the expected trend calculated in the theoretical model. The gathered results are not only useful to better design the experiment, but to provide insight for the best bookkeeping approach.

6

EXPERIMENTAL METHODS

In this chapter the preparation of the experiment is explained. Theoretical and numerical results have determined that the influence of the external flow is higher at low power settings. As a result the experiment aims to study the effects of flow suppression and boattail drag in idle conditions by testing a ultra-high bypass ratio through-flow nacelle with and without a blockage. The experiment is designed keeping in mind that results can be extrapolated to power conditions, and will help to understand which instrumentation will be required to measure the identified external flow effects.

6.1. LOW SPEED TUNNEL

The test will be performed in the Low-Speed Wind Tunnel (LST) of DNW, shown in Figure 6.1. The LST is a steel shell structure and has a drive power of 700 kW, which drives a constant pitch fan. Variation of the wind tunnel speed is achieved by variation of the rotational speed of the fan. It is an atmospheric wind tunnel of the closed return type with a contraction ratio of 9. The maximum velocity in the (empty) test section is about 80 m/s.

The test section is 3 meters wide and 2.25 meters high. The length of the exchangeable part of the test section is 5.75 meters. Downstream of this exchangeable aeronautical test section is a fixed non-aeronautical test section with a length of 3 meters. For the present test the so-called 3D aeronautical test section is used.

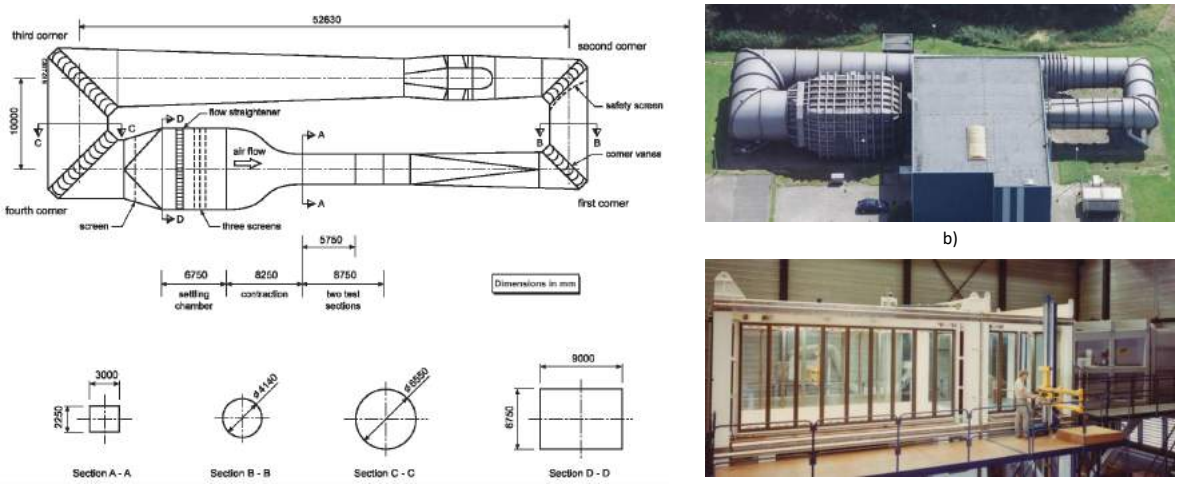

Figure 6.1: **a:** LST Top View **b:** LST aerial view **c:** Test Section

6.2. MODEL SELECTION

6.2.1. CRUF-TFN

The Counter-Rotating Ultra-High Bypass Ratio Through Flow Nacelle (CRUF-TFN) model, introduced in Section 2.2, is studied. Manufactured and owned by DLR, it was first used in 1994 [34] for the study of the jet drag interference effects on the ALVAST half model, in relation of the European Research Programmes DUPRIN and ENIFAIR, as shown in Figure 6.2 c. Static calibration data is available from previous tests, as explained in Section 2.2.2

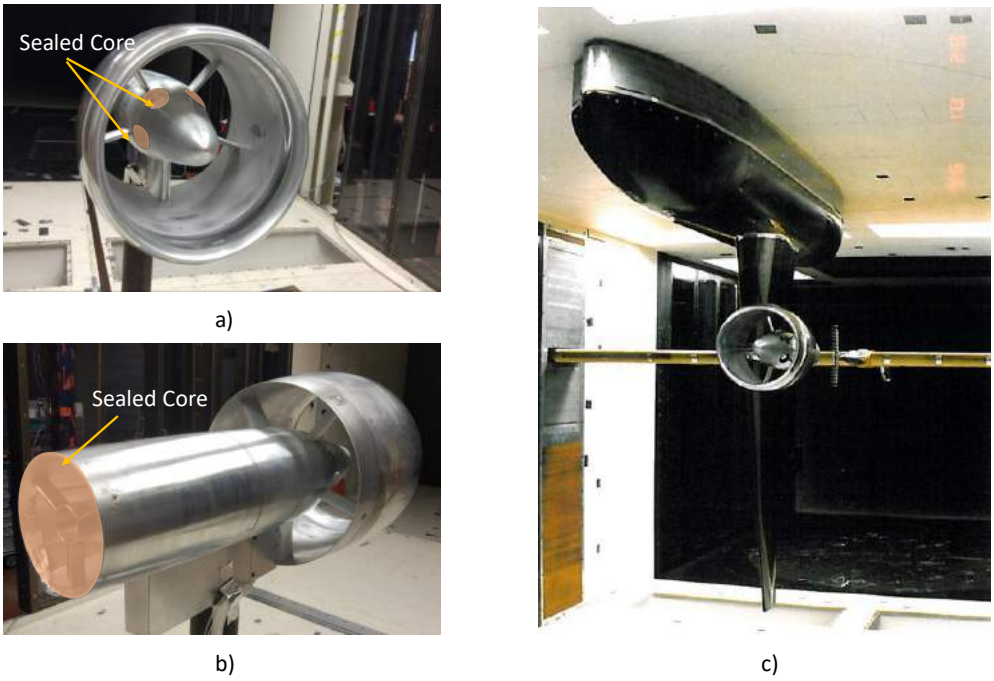

Figure 6.2: **a**: CRUF-TFN Model **c**: CRUF-TFN in ALVAST Model. Souce: [34]

6.2.2. PYLON + INTERFACE

A steel cylindrical bar 1.2 m high available at DNW is chosen as support/pylon. A special interface is designed and machined to integrate the pylon with the TFN.

6.2.3. BLOCKAGE

The blockage has been introduced in Section 4.3 as a vertical flat plate. The structure is manufactured at DNW. Two interchangeable flat plates are used with radius of respectively 0.25 and 0.35.

6.3. EXPERIMENTAL SETUP

The complete test setup is shown in Figure 6.3. The CRUF-TFN is mounted upside down by the support/pylon to the external balance. The traversing bar supports the hot wire (mean velocity measurements behind the exhaust) and Pitot-static tube from the top. The flat plate (blockage) is positioned behind the TFN, at several fixed positions along the center line. A Particle Image Velocimetryb (PIV) plane is proposed for future measurements of a more detailed study of the exhaust velocity and shear layer.

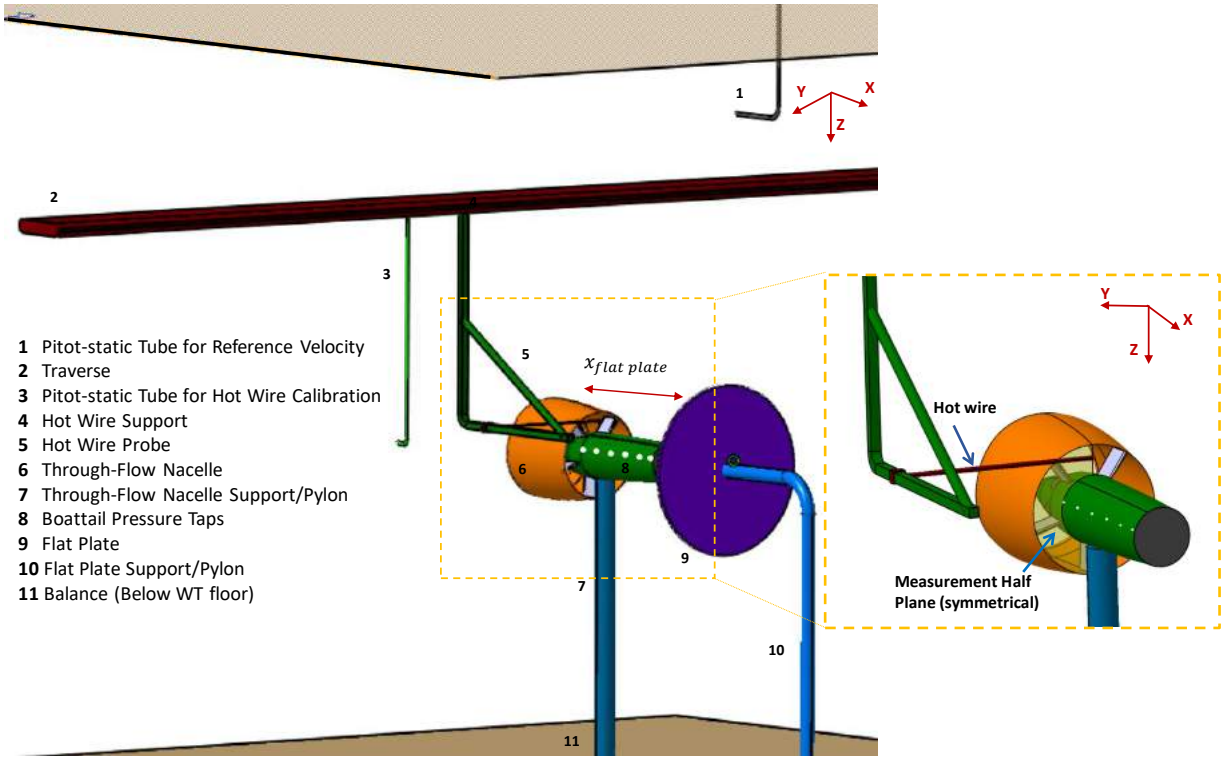

Figure 6.3: Wind Tunnel Test Setup.

6.4. INSTRUMENTATION

This section explains the instrumentation required for the experiment.

6.4.1. BALANCE SYSTEM

The total drag contribution (strut, nacelle internal + nacelle external drag) can be obtained with the half-model balance 518.

6.4.2. PITOT-STATIC TUBES

Two Pitot-static tubes are present to measure the tunnel velocity using the difference in total and static pressure. The first one is mounted to the upper wall at the x position of the TFN intake plane. This is used to obtain and adjust the wind tunnel velocity. The second one is placed on the traverse bar and is used to obtain a reference velocity to calibrate the hot wire. This is also used to provide a first order of magnitude of the TFN exhaust velocity.

6.4.3. HOT WIRE

The hot wire consist of a thin metallic element affixed to the end of a slender probe [57]. This is aligned with the flow, and heated by an electric current. Due to the convective heat transfer of the flow the metallic element is cooled. The electrical resistance of the wire/film is proportional to the temperature, allowing for the measurement of the heat transfer and the incident flow velocity. Hot wires operate at a high frequency acquisition in a large range of velocities, but intrude in the flow and are not suitable for reversed flow. A calibration curve is necessary in order to relate the voltage to the velocity.

The hot wire is used to measure the velocity profile at the fan exhaust plane. Symmetry is assumed along the vertical plane. In Figure 6.4 a the measured data points are shown. These will be closely spaced towards the walls and shear layer to measure the velocity gradients between internal and external flow. Measurements start $5mm$ away from the TFN core cowling to avoid any accidental impact with the wall surface. Each radial section corresponds with a polar. $\phi = 0^o$ stands for the reference point. In this section more data points are gathered. Check points are chosen to validate the symmetry condition and to evaluate the hot wire drift.

6.4.4. CRUF-TFN INSTRUMENTATION

The model is originally supplied with six static pressure taps at the intake, spaced every 60 degrees, and five static pressure taps at the fan nozzle exhaust, as shown in 6.4 b.

In addition, six static pressure taps are placed longitudinally in the core cowling (boattail). These were not included in the original configuration and were specially drilled for the experiment.

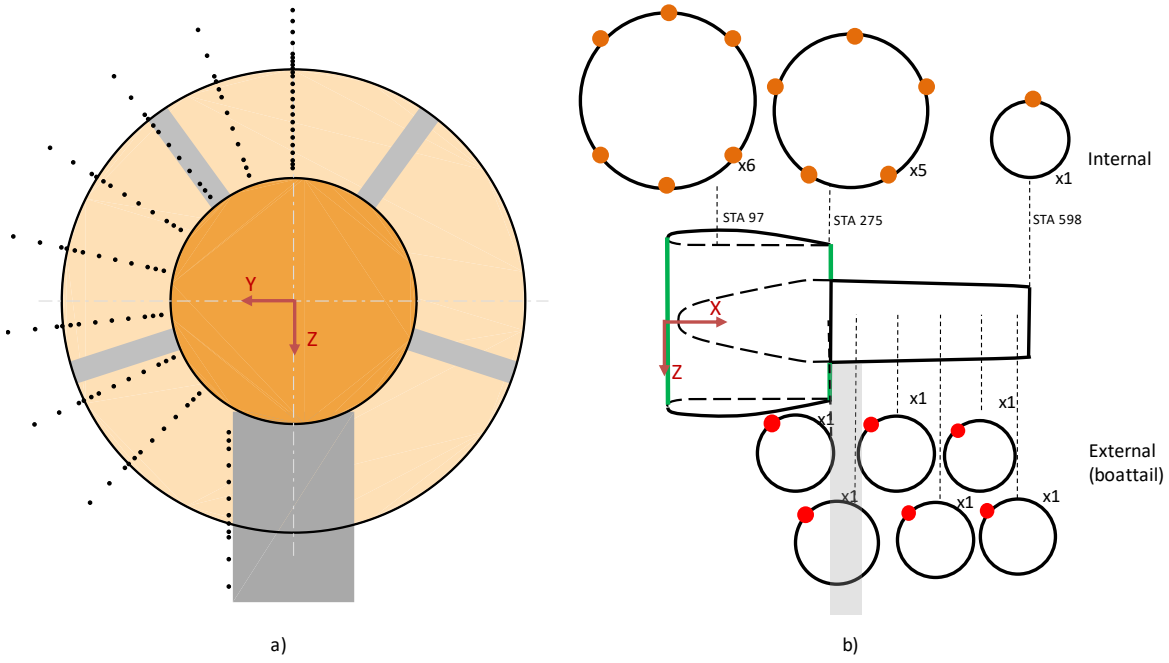

Figure 6.4: **a**: Hot Wire measurement points **b**: Location of static pressure taps

6.4.5. TRAVERSE SYSTEM

The current traverse system, used for the supporting and translation of the Pitot-static tube and hot wire, consists of a longitudinal bar that crosses the vertical walls of the wind tunnels. It can operate in the Y and Z direction by means of two servomotors with high accuracy. By properly positioning the hot wire, it is possible to measure the velocity at the semi-half exhaust plane. To displace the probe in the X direction the hot wire is attached to a slider and fixed in each measurement in predetermined positions.

6.5. DATA ACQUISITION

All measured data from the wind tunnel, TFN model and blockage are acquired in the control room. The following physical quantities are measured:

- Balance Forces
- Total Temperatures: the temperatures are measured with thermocouples and their voltage output to temperature relations are derived from standard tables.
- Total Pressure and static pressure: the pressures are measured as differential pressures with respect to the tunnel reference pressure (static back pressure of the wind tunnel). The pressure transducers are of the strain gage type. Their pressure to voltage relations are represented by polynomials of the third degree derived from their calibration. Accuracy is of ±0.2% of their full range
- Velocity from the hot wire

The output of all measurement equipment is acquired in the control room by the DNW-LST data acquisition system GAIUS. The instrumentation for data acquisition is checked daily, before a measurement day starts. Parameter settings are checked before and after a run. All the data except for the TFN measurements

are read by single channels. The TFN pressures are measured with an electronic pressure scanning RAD module.

The flow field measurements are performed in continuous testing mode. All other measurements are performed in a step-by-step mode, with the averaging time set at 5 seconds for the hot wire, and 10 seconds for the pressures. All the data is gathered by the Data Acquisition Computer that is located in the wind tunnel control room and send to the Data Processing Computer for further processing.

6.6. TEST PROGRAMME

The test program consists of a number of measurement series corresponding to two model configurations: isolated TFN and TFN+blockage, at constant Mach number 0.18. The test matrix is shown below:

Table 6.1: Test Matrix

Run #	**TFN Pylon**	**TFN**	**Flat Plate**	**Flat Plate Size** $[mm]$	**Flat Plate Distance X** $[mm]$	**Expected Cp**	Description
1	Yes	Yes	No	-	-	$C_{p,0}$	Isolated TFN
2	Yes	Yes	Yes	375	800	$0.21 + C_{p,0}$	TFN + Blockage
3	Yes	Yes	Yes	375	600	$0.32 + C_{p,0}$	
4	Yes	Yes	Yes	250	600	$0.17 + C_{p,0}$	
5	Yes	Yes	Yes	250	800	$0.11 + C_{p,0}$	
6	Yes	Yes	Yes	350	800	Asymmetric	
7	No	No	Yes	250	800	0.11	Isolated Blockage
8	No	No	Yes	250	600	0.17	
9	No	No	Yes	375	600	0.32	
10	No	No	Yes	375	600	0.21	
11	No	No	Yes	375	800	Asymmetric	
12	Yes	No	No	-	-	-	Isolated TFN Pylon

Figure 6.5: Different tested configurations. From left to right: TFN + flat plate, R = 0.25 m. TFN + flat plate, R = 0.375 m, TFN + asymmetric flat plate, R = 0.375 m

6.6.1. ISOLATED THROUGH-FLOW NACELLE

The hot wire is calibrated versus the Pitot-static tube in an undisturbed area according to the expected velocity range. This range is obtained by placing the Pitot-static tube in the TFN fan exhaust plane. After calibration this exhaust plane is scanned again with the the hot wire in order to obtain a more accurate velocity profile. Also, the balance and the internal TFN pressure measurements are recorded.

6.6.2. THROUGH-FLOW NACELLE + BLOCKAGE

The relative distance of the blockage with respect to the TFN is changed, in order to produce a measurable flow suppression and change in boattail, as estimated from the numerical results. The same procedure as in the previous is followed.

6.7. DATA PROCESSING

6.7.1. PRESSURE INFORMATION

The pressures are obtained at the intake, fan and boattail. The mean value can be directly obtained as:

$$\bar{P}_{s,intake} = \frac{\sum_{i=1}^{6} P_{s,fan,i}}{6} \tag{6.1}$$

$$\bar{P}_{s,fan} = \frac{\sum_{i=1}^{5} P_{s,fan,i}}{5} \tag{6.2}$$

$$\bar{P}_{s,boattail} = \frac{\sum_{i=1}^{6} P_{s,boattail,i}\, d_i}{6} \tag{6.3}$$

The pressure coefficient is then obtained for each section as:

$$C_P = \frac{\bar{P}_s - P_{s,0}}{\frac{1}{2}\rho V_0^2} \tag{6.4}$$

6.7.2. CALIBRATION APPROACH

In the calibration report the configuration with the blocked core is calibrated in the ECF by obtaining the discharge coefficient for intake and fan nozzle, and velocity coefficient for the TFN. The gathered data is useful to obtain the actual TFN mass flow and ideal exit velocity according to the information from the pressure taps (standard method), as no core flow is present. In this case, the local conditions should be used, as explained in Section 3.1.3.

The mass flow is obtained according to the average pressure at the fan exhaust plane, $\bar{P}_{s,fan}$ (standard method) or intake $\bar{P}_{s,intake}$ (new method) and the calibration discharge coefficients. Both methods should give the same mass flow:

$$\dot{m}_{ac,fan} = C_{D,fan}\dot{m}_{id,fan} \tag{6.5}$$

$$\dot{m}_{ac,intake} = C_{D,intake}\dot{m}_{id,intake} \tag{6.6}$$

$$\dot{m}_{id,fan} = \frac{P_{t,0}A_{19}}{\sqrt{T_{t,0}}}\left(\frac{P_{t,0}}{\bar{P}_{s,fan}}\right)^{\frac{-1}{\gamma}}\sqrt{\frac{2}{R}\frac{\gamma}{\gamma-1}\left(1-\left(\frac{P_{t,0}}{\bar{P}_{s,fan}}\right)^{\frac{1-\gamma}{\gamma}}\right)} \tag{6.7}$$

$$\dot{m}_{id,intake} = \frac{P_{t,0}A_{19}}{\sqrt{T_{t,0}}}\left(\frac{P_{t,0}}{\bar{P}_{s,intake}}\right)^{\frac{-1}{\gamma}}\sqrt{\frac{2}{R}\frac{\gamma}{\gamma-1}\left(1-\left(\frac{P_{t,0}}{\bar{P}_{s,intake}}\right)^{\frac{1-\gamma}{\gamma}}\right)} \tag{6.8}$$

The ideal jet velocity in the exhaust is assumed to be fully expanded to the local pressure $\bar{P}_{s,fan}$.

$$V_{id,fan,e} = \sqrt{\frac{2\gamma}{\gamma-1} R T_{t,fan} \left[1 - \left(\frac{\bar{P}_{s,fan}}{P_{t,0}} \right)^{\frac{\bar{P}_{s,fan}}{P_{t,0}}} \right]} \tag{6.9}$$

6.7.3. HOT WIRE APPROACH

The velocity is obtained at 5 mm away from the fan exhaust plane with the hot wire. The obtained velocity field is interpolated in a uniform grid of $n_{i,HW}$ points. An area weighted average is obtained with the measurement points to obtain the average value.

$$\bar{V}_{HW,fan} = \frac{\sum_{i=1}^{n_{i,HW}} V_i A_i}{\sum_{i=1}^{n_{i,HW}} A_i} \tag{6.10}$$

The mass flow is obtained according to this velocity and the freestream density:

$$\dot{m}_{fan} = \rho_0 A_{fan} \bar{V}_{HW,fan} \tag{6.11}$$

6.8. CONCLUSIONS

The experimental approach has been introduced. This consists in the testing of a high bypass ratio Through-Flow Nacelle with different blockages to simulate the influence of the wing pressure wing in the fan exhaust. The static pressure distribution at the intake plane, fan exhaust plane and boattail are measured. The velocity 5 mm away from the fan exhaust is scanned with a hot wire.

The final objective is to show the effect of flow suppression by correlating the hot wire and the calibration approach. This will provide insight regarding the new bookkeeping approach introduced in previous chapters.

7

EXPERIMENTAL RESULTS

This chapter outlines the main experimental results as of the test campaign. First the results of the isolated Trough-Flow Nacelle, the baseline configuration, are presented in detail. Then these are compared with the combined TFN + flat plate. The effects of flow suppression and boattail drag are also compared with the mathematical model (ideal effect of flow suppression) and the CFD results, that have been computed again according to the wind tunnel conditions.

7.1. ISOLATED THROUGH-FLOW NACELLE

The isolated TFN serves as baseline configuration to later investigate the effects of flow suppression.

7.1.1. VELOCITY PROFILE

Figure 7.1 a shows the measured velocity profile at 5 mm from the exhaust plane, obtained with the Hot Wire following Section 6.4.3. This is field is interpolated with splines in Figure 7.1 b. From the interpolated field an area weighted average velocity of 56.54 m/s is obtained. The velocity decrease in the wake can be recognized by the blue color, as well as the decrease in velocity due to the TFN internal support, indicated by the arrow.

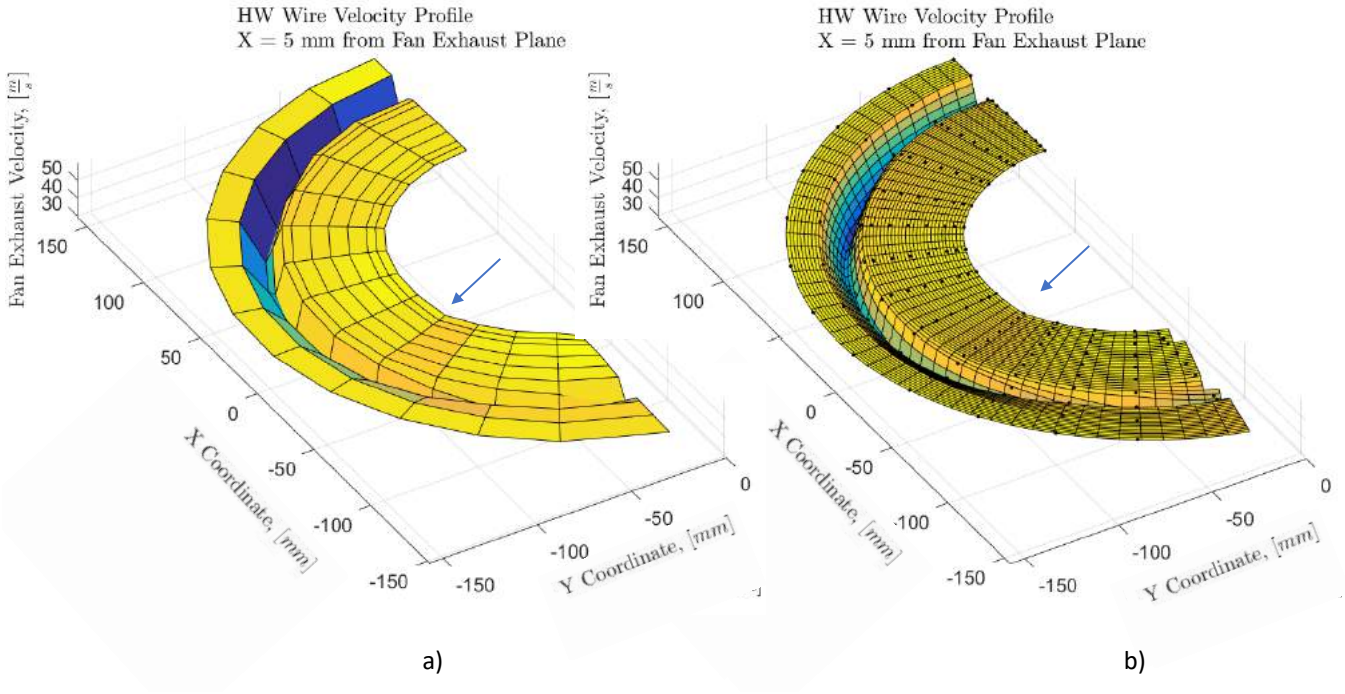

Figure 7.1: Velocity Profile at 5 mm away from the fan exhaust plane. **a:** Obtained with Hot Wire **b:** Interpolated following spline method

Figure 7.2 compares the measured velocity profile along $\phi = 0^o$ (with the smaller step of one millimeter, with the axisymmetric numerical solution. The latter underestimates the velocity in this fan plane and wake, reaching the same value as in the experiment outside of the wake.

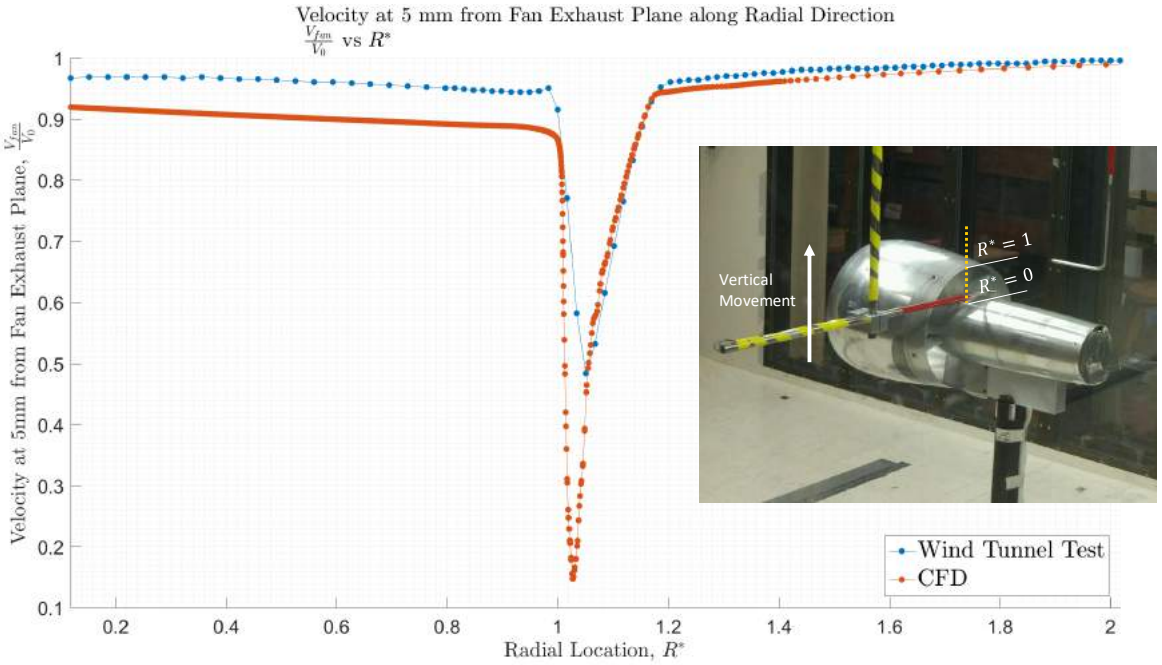

Figure 7.2: **a:** Change along the fan exhaust plane pressure due to the location of the hot wire

7.1.2. EFFECT OF HOT WIRE

The influence of the hot wire probe in the fan exhaust plane is shown in Figure 7.3. In this case the probe scans the vertical line along $\phi = 0^o$. Pressure information is gathered when the hot wire probe is in the calibration position, far away from the TFN (straight lines). However, when measuring the exhaust velocity, a small blockage may be present. This blockage artificially increases the static pressure in the fan exhaust plane, especially in the section that is closer to the horizontal probe ($\phi = 72^o$). No correction is applied to this effect as it is not dominant, and it is always present. When comparing the isolated TFN with the TFN + flat plate, its effect will be removed.

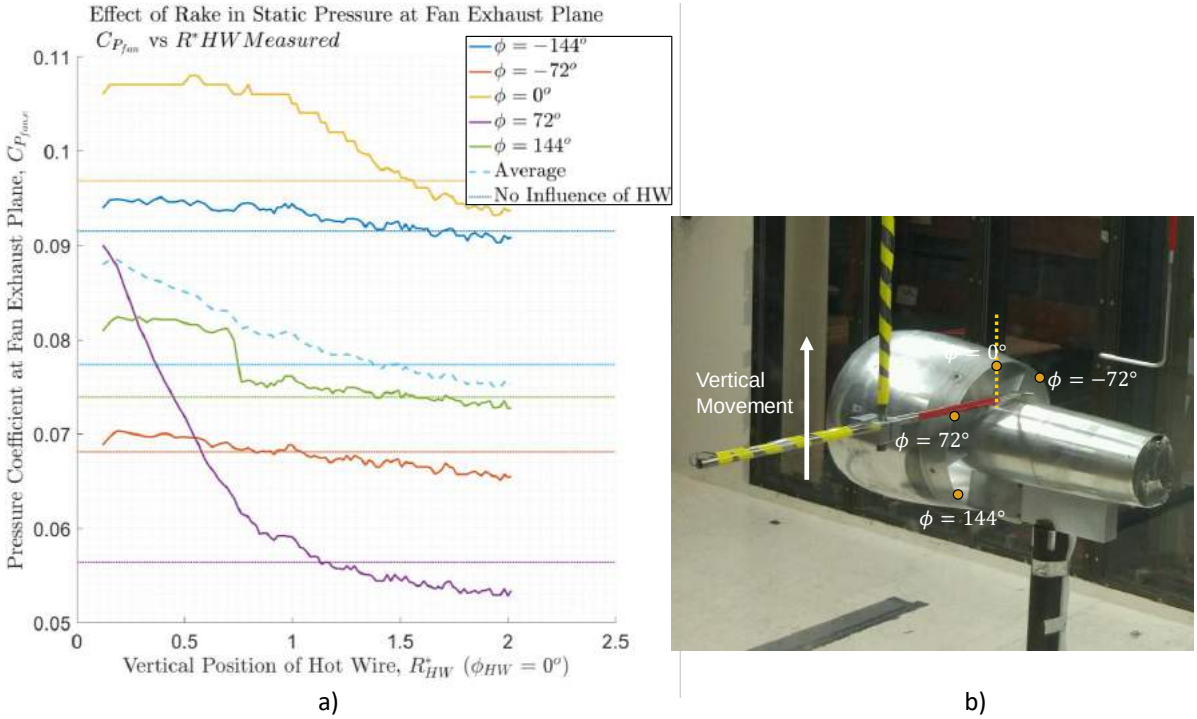

Figure 7.3: **a:** Influence of the hot wire location on the fan exhaust pressure

7.1.3. PRESSURE PROFILES

The pressure profiles in the intake plane, fan exhaust plane and boattail are shown in Figure 7.4 a, b and c respectively. Symmetry is present along the vertical plane. The CFD overestimates the pressure coefficient at the fan exhaust and boattail plane, while underestimates the intake pressure. Differences are due to 3D flow effects (the pressure is not constant along the circumferential direction), improper representation of the geometry, numerical and modelling errors and wind tunnel effects. However, both computation and experiment determine that at the TFN in isolation, the exhaust pressure is slightly higher than freestream. In this case, suppression is already present due to the freestream flow as explained in Section 5.1.

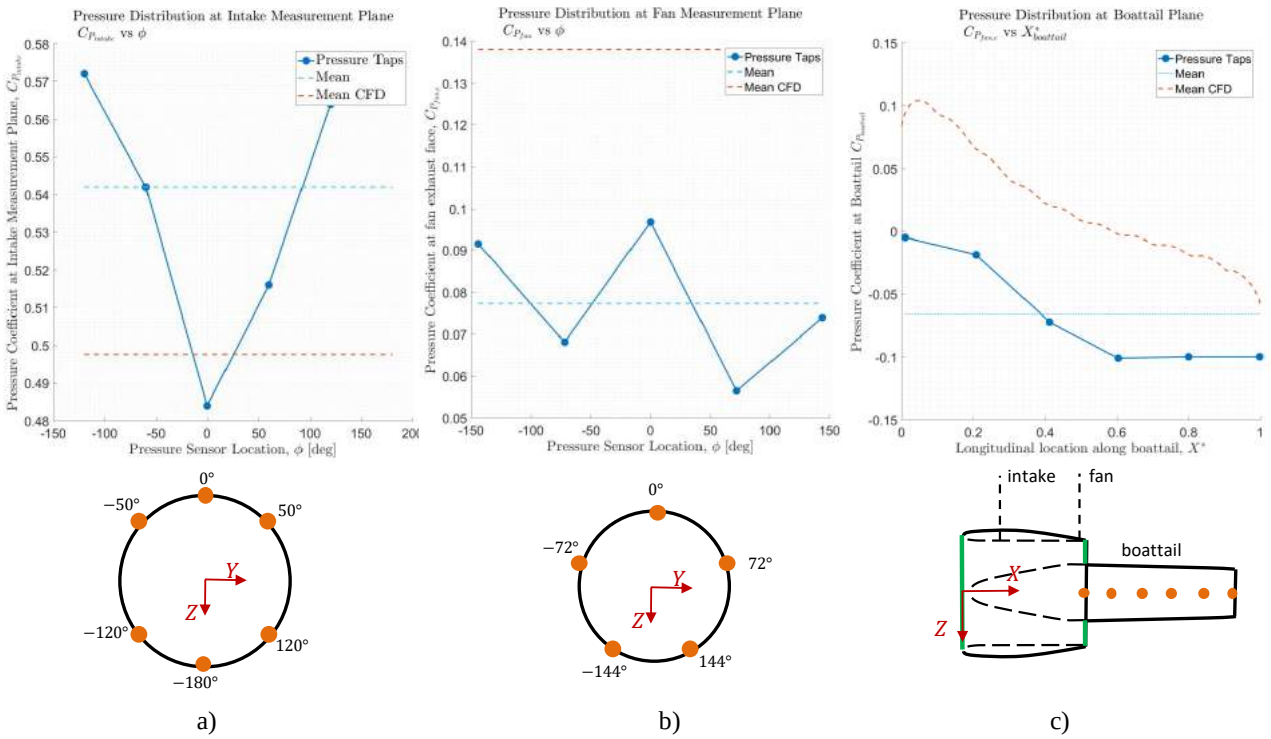

Figure 7.4: Pressure coefficient profiles along **a:** Intake measurement plane, **b:** fan exhaust plane **c:** boattail plane

7.2. THROUGH-FLOW NACELLE + FLAT PLATE

This section analyzes the effects of the location of the flat plate in the TFN performance.

7.2.1. COMPARISON OF PRESSURE PROFILES

CHANGE IN FAN AND INTAKE PRESSURE

Figure 7.5 shows the fan, intake and boattail pressure distributions respectively at different flat plate locations, represented by the dimensionless distance, $\frac{x}{\sqrt{A_{flatplate}}}$. As the flat plate diameter increases and moves closer to the TFN, the suppression effect increases by increasing the pressure coefficient. The pressure field generated by the flat plate is not only detected by the fan plane pressure sensors, but also by the intake pressure sensors. The asymmetrical configuration (dash line in light blue color) leads to a similar suppression level as with the symmetrical position due to the increase in pressures in the lower surface and decrease in the upper surface.

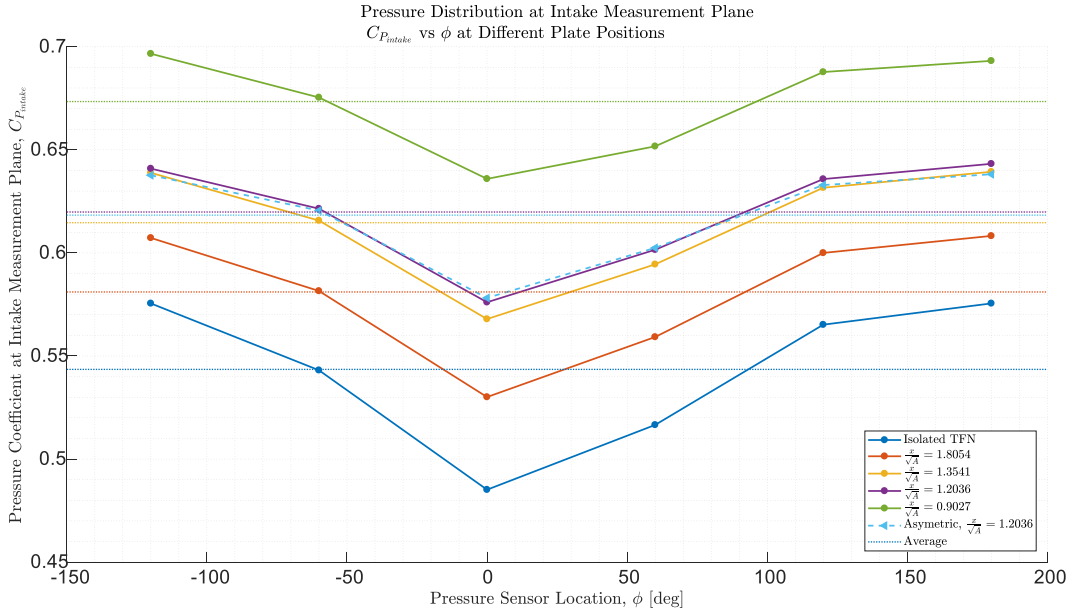

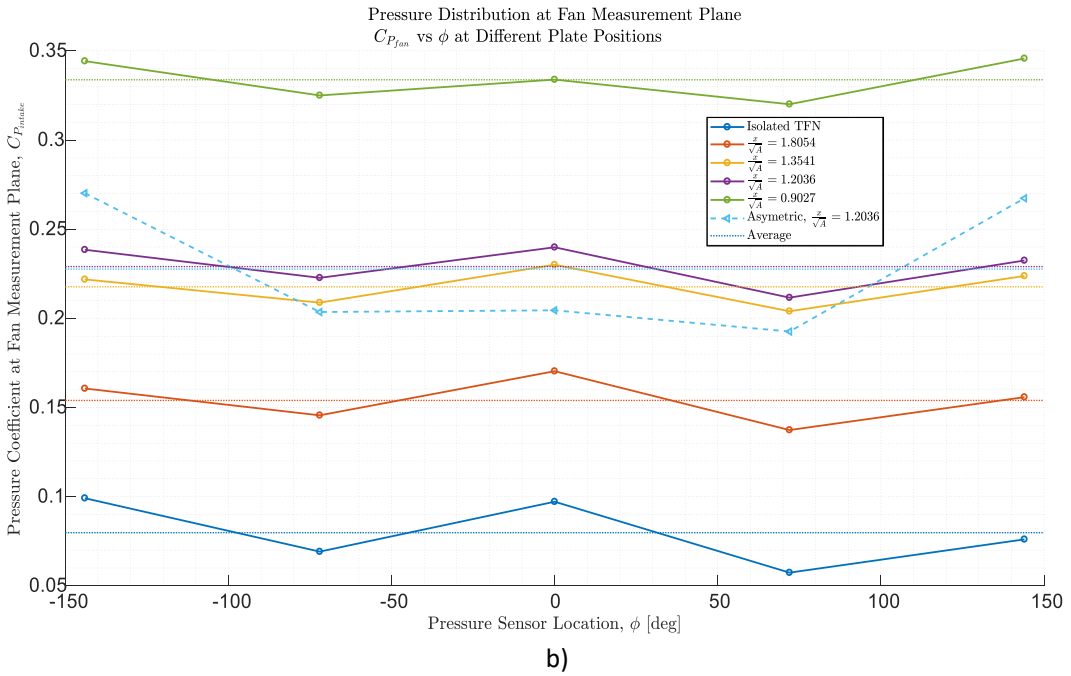

Figure 7.5: Pressure Distribution in **a:** Intake Measurement Plane and **b:** Fan Exhaust Plane

CHANGE IN BOATTAIL PRESSURE

Figure 7.6 shows the pressure distribution along the boattail measurement line. The boattail suffers higher pressures with the location of the flat plate. This increases the force and affects the internal drag of the TFN, bookkept as a lost of thrust. According to the geometry, this increase could strongly affect the bookkeeping.

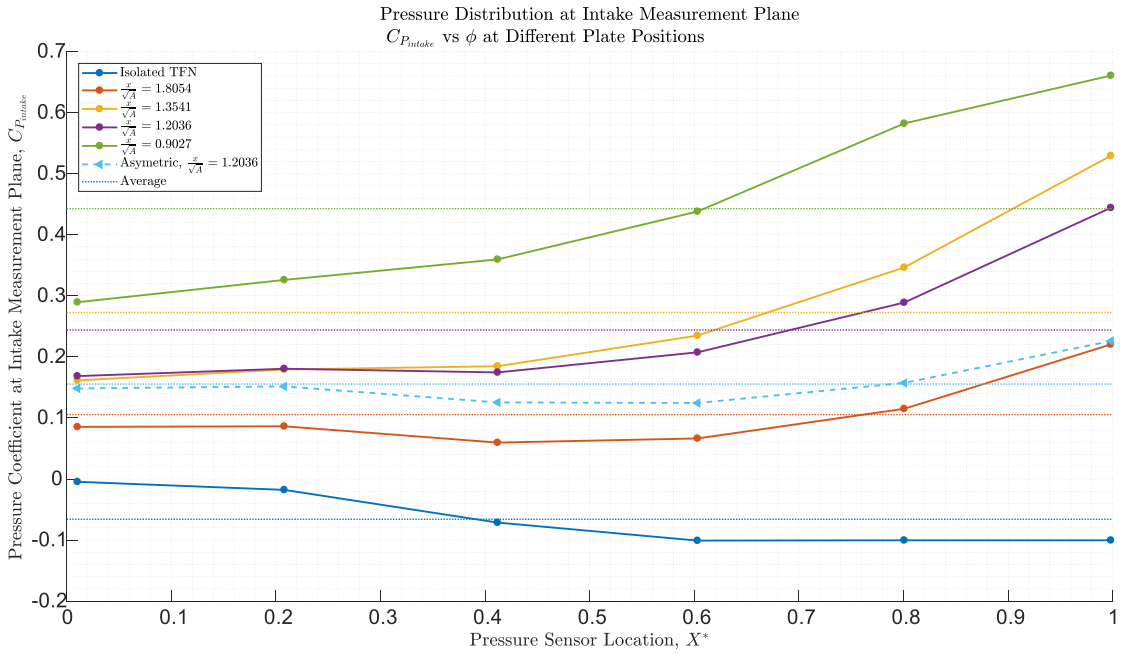

Figure 7.6: Pressure distribution along the boattail at different positions of the plat plate

7.2.2. COMPARISON OF VELOCITY PROFILES

Figure 7.7 compares the velocity profiles obtained with the hot wire, between the isolated TFN (left hand side) and the TFN + flat plate (right hand side). When the flat plate is present the velocity is decreased in the TFN fan exhaust plane. The effect is stronger with the larger flat plates. The asymmetric configuration decreases more the velocity in the lower part of the fan exhaust plane, in order to simulate the pressure field generated by a wing.

Flat Plate Distance
x = 0,8 m

Flat Plate Distance
x= 0,6 m

Flat Plate Size
R = 0,25 m

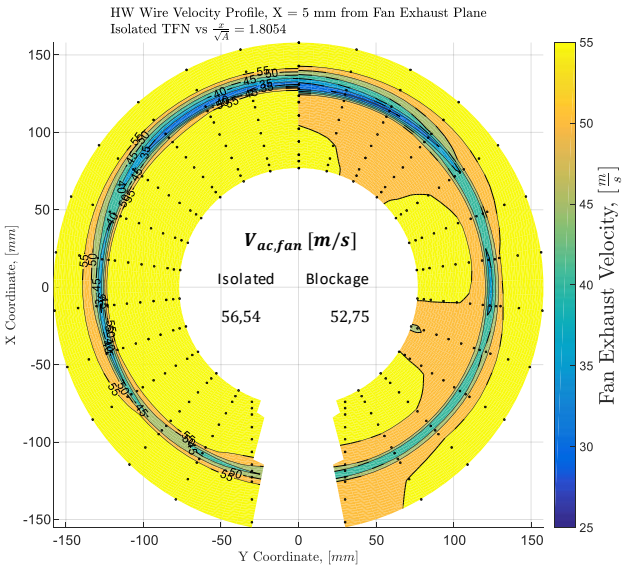

a)

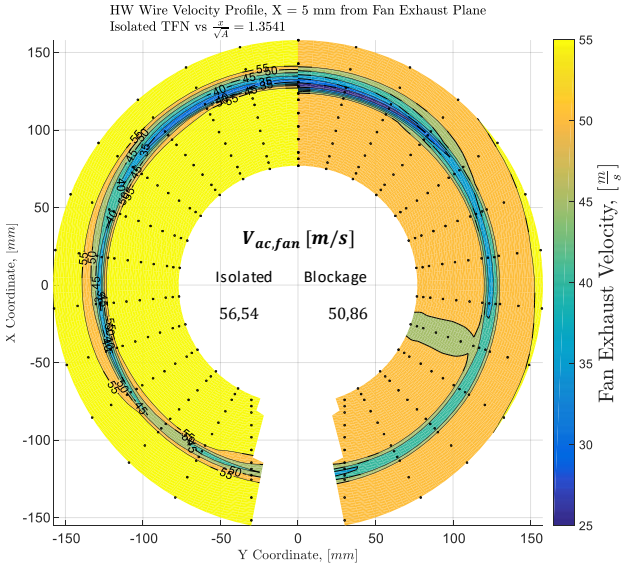

b)

Flat Plate Size
R = 0,375 m

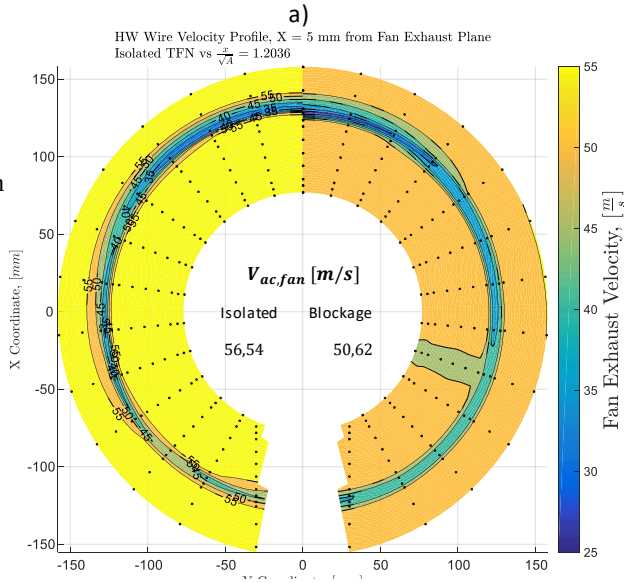

c)

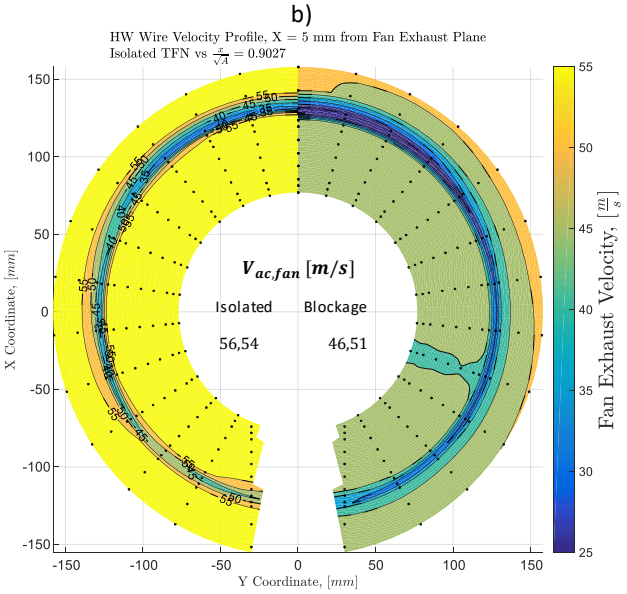

d)

Asymmetric, Flat Plate Size
R = 0,375 m

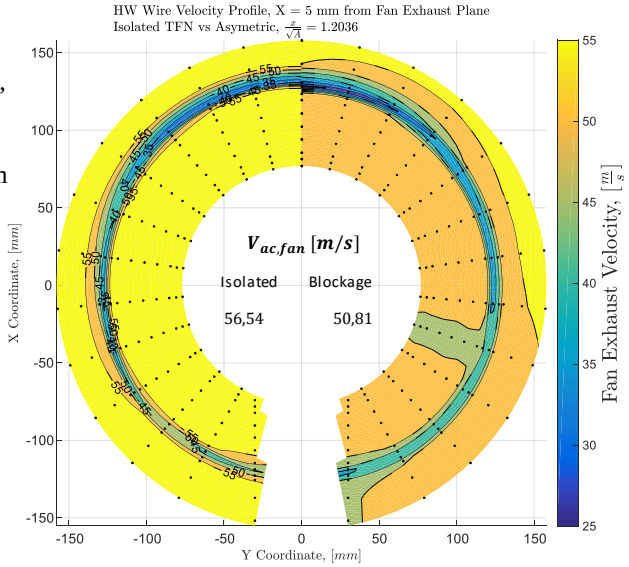

e)

Figure 7.7: Interpolated velocity profile obtained with the hot wire. Left hand side: isolated TFN. Right Hand side:**a:** $\frac{x}{\sqrt{A}} = 1.805$, **b:** $\frac{x}{\sqrt{A}} = 1.354$, **c:** $\frac{x}{\sqrt{A}} = 1.204$, **d:** $\frac{x}{\sqrt{A}} = 0.903$,**e:** Asymmetric $\frac{x}{\sqrt{A}} = 1.204$

7.2.3. DECREASE IN MASS FLOW AND EXHAUST VELOCITY

Figures 7.8 a and b summarize the experimental results. These show the decrease in TFN exhaust velocity and mass flow due to the increase in fan exhaust pressure caused by the different flat plates. The decrease is also proportional to the dimensionless distance. Error bars are placed according to the accuracy of the hot wire (due to drift vs time) and the pressure sensors.

Looking at Figure 7.8 a the ideal velocity obtained with the mathematical model of section 3.1 and the CFD results, follows the same decrease rate (slope) with the suppression level. The offset can be corrected for using calibration coefficients or by increasing the sophistication of the numerical approach.

In Figure 7.8 b the actual mass flow obtained with the intake and fan calibration coefficients [35], also captures the same decrease of mass flow as with the hot wire. This is relevant as it shows a path to bookkeep the pressure level measured at the intake with the actual mass flow.

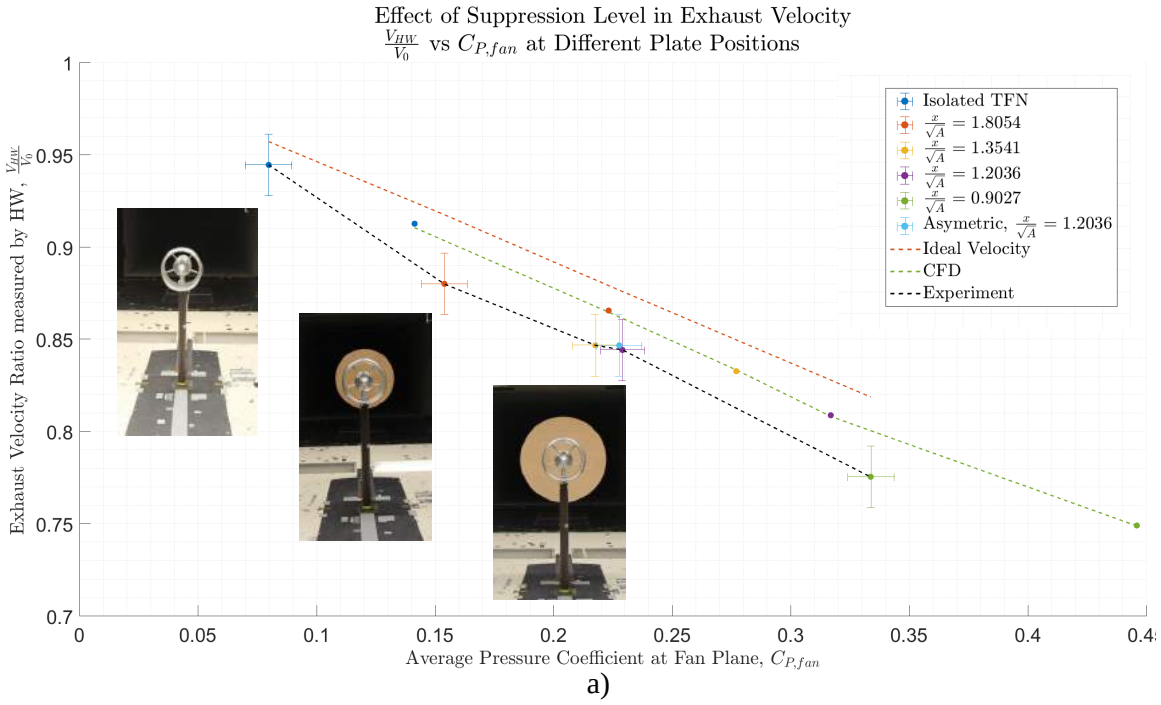

a)

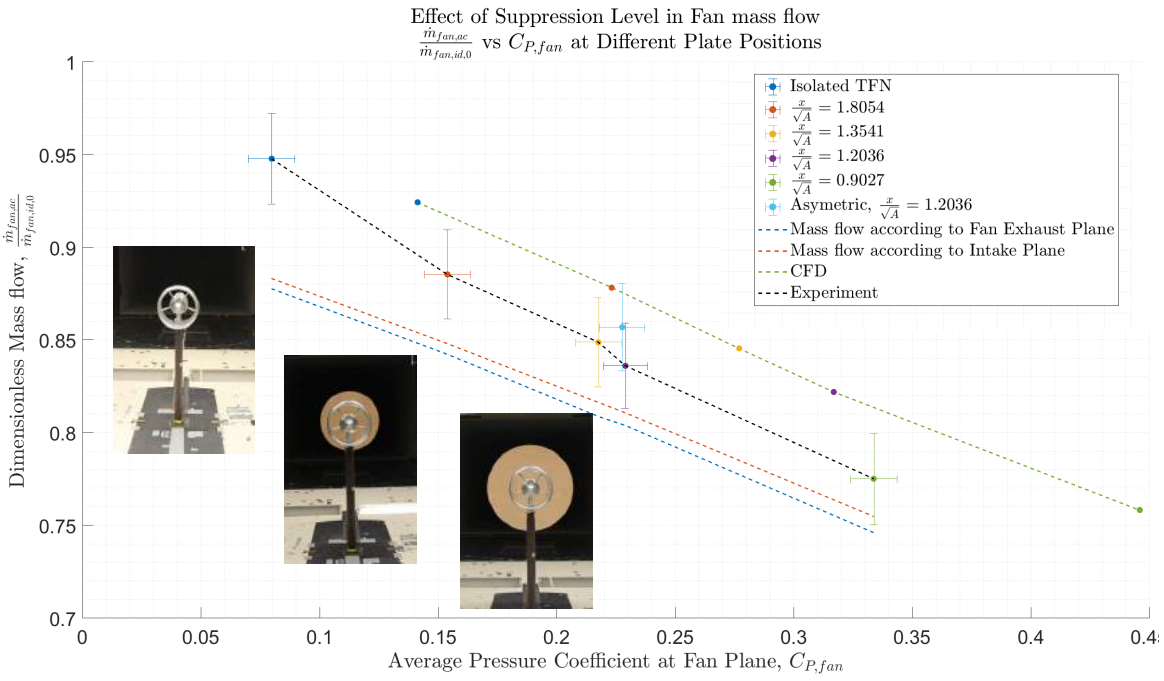

b)

Figure 7.8: Effect of flow suppression at different configurations **a:** Velocity at the Fan exhaust plane obtained with the hot wire vs Pressure Coefficient at the fan exhaust plane **b:** Fan mass flow obtained with the hot wire vs Pressure Coefficient at the fan exhaust plane

7.2.4. CORRELATION OF FAN EXHAUST PLANE CONDITIONS

This subsection shows the relationship between conditions at the fan exhaust plane (the area of interest) with the boattail and intake measurement planes. In real practise is difficult to locate static pressure taps in the fan exhaust plane. By placing instrumentation in the intake plane or boattail it would be possible to bookkeep the decrease in mass flow with the pressure in these stations.

Figure 7.9 a shows a linear relationship between the intake and fan pressure, independently of the flat plate size. In subsonic conditions the information (blockage) travels upstream and reaches the intake measurement plane. This shows that the decrease in velocity and mass flow of the previous Figure 7.8 can be perfectly represented vs the intake pressure (instead of the fan exhaust pressure).

Figure 7.9 b shows that the increase in fan pressure can also be correlated with the first pressure tap in the boattail. This relation is not as good as with the intake (specially in the asymmetric condition) but can lead to the measurement and quantification of flow suppression as well as boattail drag.

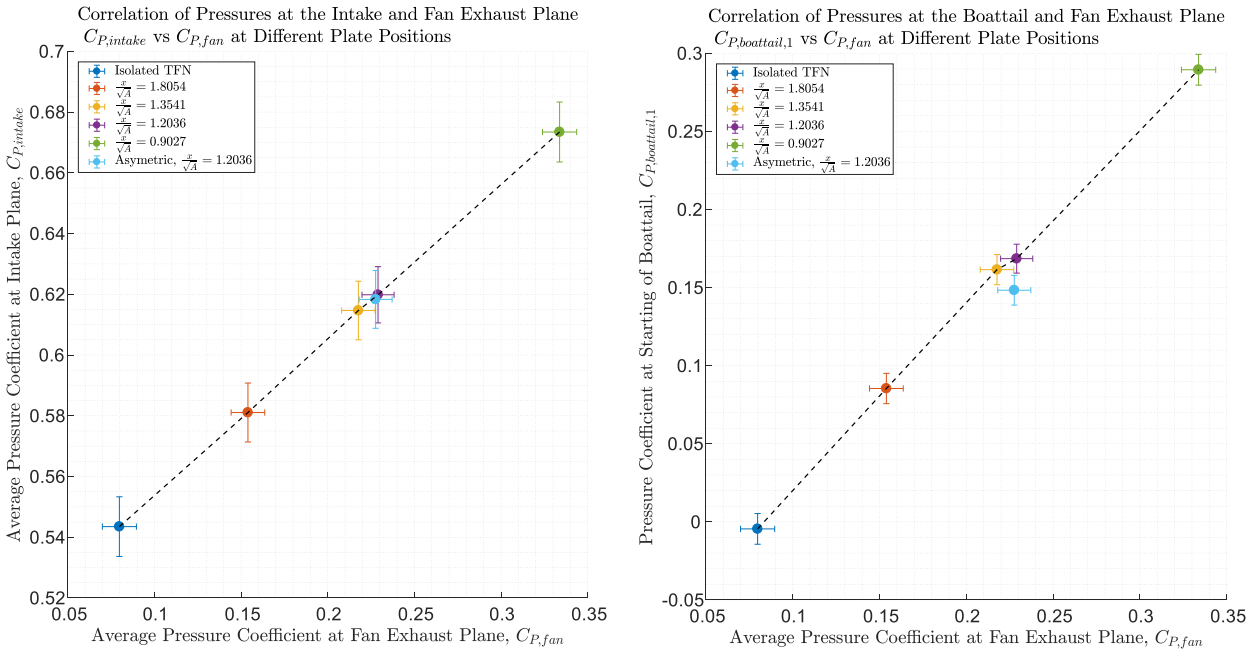

a) b)

Figure 7.9: Correlation of the pressure at the fan exhaust plane (suppression level) with **a:** Pressure at the intake measurement plane **b:** Pressure at the first measurement point of the boattail (near fan exhaust plane)

7.3. CONCLUSIONS

The hot wire is a reliable but slow method to map the fan exhaust velocity, while the pressure taps provide fast, accurate but limited information regarding the pressure distribution of the internal flow.

The suppression effect has successfully been recreated by placing the vertical flat plate at different configurations of size and distance to the fan exhaust plane. This increases the pressure level at the fan exhaust plane. As a result the fan mass flow and exhaust velocity is decreased up to a 23 % as the flat plate dimensionless distance is reduced. The decrease rate follows with the theoretical and numerical calculations, despite an offset is present between the three methods that can be corrected for. Also in the isolated configuration already a slightly higher than freestream pressure (suppression) is present in the fan exhaust plane only due to the freestream flow. the suppression effect is related with a considerable increase of the pressures in the boattail. This increase should be corrected for according to the proposed thrust/drag bookkeeping method.

The decrease in mass flow and velocity can be effectively captured by the pressure taps located at both the intake and fan plane. A linear correlation exists between the fan and intake pressure, that can be used in the future for the bookkeeping of the TPS mass flow in the wind tunnel according to calibration coefficients obtained in static and wind-on conditions.

To sum up, the experimental approach has validated the mathematical model and provides insight regarding the required instrumentation for the bookkeeping of the next generation of turbofan engines.

8

CONCLUSIONS AND RECOMMENDATIONS

The optimization of the whole system engine/pylon/airframe is necessary to achieve low levels of interference drag and can determine the success of an aircraft. The integration of the engine with the airframe has been effectively investigated in wind tunnels during the last 40 years by means of Turbofan Powered Simulators. However, the traditional bookkeeping approach, which assumes that the static calibrated thrust is the same in the wind tunnel, is no longer valid for the next generation of ultra-high bypass ratio turbofan engines. These engines are not only placed closer to the wing (increasing interference effects) but also operate with an unchocked nozzle in a larger part of the flight regime.

The following chapter presents the conclusions and recommendations to effectively implement a new bookkeeping method for the Engine/Airframe Integration testing technique by including the external flow effects.

8.1. CONCLUSIONS

Based on the comparison of procedures undertaken in other testing facilities, the review of the thrust/drag bookkeeping of full-scale turbofan engines, the study of previous test data and the analysis of theoretical numerical and experimental models, the main hypothesis has been validated: the external flow affects the fan exhaust jet of Turbofan Powered Simulators (and Through Flow Nacelles) with respect to quiescent conditions.

The numerical model highlights that the shear layer (interface between the exhaust plume and freestream flow) decreases in size with the external velocity as the difference in velocities between plume and free air is decreased. As a result the flow spreading rate, the exchange in velocity between the plume and the medium, decreases with the freestream Mach number. This changes the development of the fan exhaust jet and increases the static pressure in this location. This increase of static pressure with the Mach number is independent of the power conditions. In addition, the fan exhaust plane of modern turbofan engines is located very close to the lower leading edge of the airfoil, in an area of higher than freestream pressures. This increase in pressure in the fan nozzle exhaust adds up to the increase due to the freestream velocity.

As a result of the change in static pressure, the local nozzle pressure ratio is reduced. In unchocked conditions, flow suppression is originated. The TPS suffers a decrease of the fan mass flow and exhaust velocity that is dominant at low power settings and high freestream Mach numbers. External flow effects are reduced with the fan nozzle pressure ratio until chocked conditions are reached, where the freestream velocity has no influence in the TPS performance. In addition the boattail drag (bookkept as a loss of thrust) is considerably affected due to the change in the pressure distribution. These two effects change the TPS thrust with respect to calibration conditions, especially at medium power settings. This leads towards an improperly bookkeeping of the aircraft installation drag of 5 to 30 drag counts depending on the freestream Mach number ($M_0 = 0.8$ and $M_0 = 0.25$ respectively). The differences are compared with the standard instrumentation error by means of an error propagation study together with a Monte Carlo analysis. It is concluded that flow suppression produces a bias error one order of magnitude higher than the standard error and should be corrected for.

A possible solution lies in the definition of thrust. The current approach neglects the thrust contribution from the nozzle exhaust (station 9) to infinite downstream (station 00). This simplification is not valid when the exit pressure differs from the freestream. By expanding the flow from the exhaust to 00 without any trans-

fer of energy of momentum it is possible to relate conditions at 00 from those at 9. As a result the Jones Thrust must be used in the new bookkeeping method, together with the accounting of the boattail and scrubbing drag. The actual mass flow should be obtained with the calibration discharge coefficient and the ideal mass flow calculated for local conditions. If the exhaust velocity is the simulating parameter, the power settings of the TPS must be increased to match the quiescent one.

These effects are further investigated for idle conditions (where the maximum influence occurs) by testing a Through-Flow Nacelle in the wind tunnel. The suppression is successfully created by placing a vertical flat plate with different configurations of size and distance behind the fan exhaust plane. The pressure level is increased at the fan exhaust plane dependent on the dimensionless distance. As a result the fan mass flow and exhaust velocity is decreased up to 23 % when the flat plate dimensionless distance is reduced. The decrease rate follows with the theoretical and numerical calculations, despite an offset between the three methods that can be corrected for. In the isolated configuration already a slightly higher than freestream pressure is present in the fan exhaust plane. This indicates the presence of suppression effect also due to the freestream flow.

From the experimental approach it has also been concluded that the decrease in mass flow and velocity can be effectively captured by the pressure taps located at both the intake and fan exhaust plane. A linear correlation exists between the fan and intake pressure, that can be used in the future for the bookkeeping of the TPS mass flow in the wind tunnel according to calibration coefficients obtained in static and wind-on conditions. The suppression effect also causes a considerable increase of the pressures in the boattail. This increase should be corrected for according to the proposed thrust/drag bookkeeping method.

The use of simplified CFD models provides a first order of magnitude to assess the influence of the wing pressure field and freestream velocity in the thrust. However, the current numerical model does not predict the static calibration trend of the TPS. The performance of each TPS is unique due to manufacturing tolerances, operating conditions and flow complexity inside the fan and core nozzles. Calibration of the TPS in isolation will be necessary in the short to medium term future.

Finally, external flow effects were investigated in the past by aircraft manufacturers. However, these effects had no significant contribution to the engine thrust due to the lower bypass ratio and operation at high nozzle pressure ratios and in chocked conditions. This research has demonstrated that nowadays the effect of external flow on thrust is significant. Theoretical, numerical and experimental results explain flow suppression and boattail drag is present in modern turbofan engines and should be corrected for.

8.2. RECOMMENDATIONS

Based on the analysis, future engine/integration tests should include external flow effects in the bookkeeping. Otherwise an overestimation of thrust, leading to a considerable overestimation of aircraft drag is expected. The following recommendations are given:

- The Jones thrust as introduced in Section 2.5 should be used in the new bookkeeping approach. This accounts for the decrease in mass flow, the expansion to infinity and, if desired by the costumer, the addition of the boattail drag. The latter can be calculated by integrating the pressure field obtained by sensors at the TPS fan boattail.

- Following the modified bookkeeping method it is necessary to correct for the decrease in the local Nozzle Pressure Ratio by increasing the TPS power settings. Despite the Jones thrust assumes perfect expansion to infinity, the exhaust Mach number M_{fan} is the main parameter of interest with respect to full scale tests and should be kept the same.

- The suppression level (pressure coefficient) at the fan nozzle exhaust must be measured. As explained, the increase in static pressure in this area is the basic indicator of external flow effects that change the thrust with respect to calibration conditions. It is then necessary to add static pressure taps in the fan nozzle exhaust plane of the TPS, in a similar distribution as with the analyzed Through Flow Nacelle. By also locating static pressure taps along the boattail it would be also possible to measure the boattail drag.

- Due to size constraints it is not always possible to add new instrumentation to the fan exhaust nozzle. The experimental approach has shown a perfectly linear correlation between the intake and fan exhaust pressure. Also a good correlation exists between the boattail and fan exhaust pressure. Then, it is possible to correlate the suppression level with pressure sensors placed at the TPS intake (where more

space is available). This can be done both at the Engine Calibration Facility and at the wind tunnel, with only two data points.

- Based on the result of this research it is recommended for future tests to compare the TPS performance in the wind tunnel with respect to the calibrated conditions. It would be useful to measure again the velocity and pressure profile of a TPS at different power settings and freestream Mach numbers, and compare if a linear correlation still exists between the intake and exhaust station.

In addition of the previous recommendations for a successful engine/airframe integration test, the research could be extended. Future work includes:

- The further study of TPS and TFN with asymmetric configurations. This configuration is expected to have the most similar pressure field to the wing. Due to limitations in the test setup it could not be studied with more detail.
- The validation of the proposed correlation between fan and intake pressure field in the TPS unit. This can be achieved in the ECF or in the wind tunnel.
- The expansion of the CFD model to simulate the 3D wing with a TPS. Boundary conditions at the measurement plane can be introduced according to the distortion pattern of the TPS. Then, the differences with respect to calibration conditions can be studied in a similar way as presented in the 2D case, but with more detail.
- The identification of additional external flow effects. In this thesis, the primary influences of the freestream flow (the ones that affect the most the classical bookkeeping method) have been identified. However, additional effects may be present such as the interaction with the exhaust flow with the supersonic flow in transonic flight or the influence of the plume with high lift devices. Appendix D provides an overview of additional interference effects that could affect the bookkept thrust of TPS units.
- The Jones thrust is an improvement with respect to the previous bookkeeping approach. However, it assumes that the expansion of the exhaust velocity to infinity is done adiabatically and isentropically. This may not be the case when losses are present and the flow in the plume is not perfectly expanded.
- The study of the limitations involving the core flow. This research has been focused on the bookkeeping of the fan flow. Despite the mass flow core is measured from the supply line, several problems have been found in the Literature regarding the core. Examples are the condensation of the flow due to the expansion at low temperatures and the possibility of reversed flow at the core at low power settings due to the increase in the static pressure. The latter problem has actually been found in the CFD simulations at low core nozzle pressure ratios.

More than 40 years ago, Turbofan Powered Simulators bridged the gap between engine and airframe companies by providing enough visibility to the problem of engine/airframe integration. Nowadays, as these effects are further increased due to larger and more efficient engines, the collaboration must be greater. The combined work of aircraft designers, engine manufacturers and wind tunnel experts is key to provide a consistent testing approach that will lead to the next generation of commercial aircraft.

A

Reference Stations

In Figure A.1 the reference stations of the TPS are shown. With the difference of the compressor, the stations are the same as for turbofan engines.

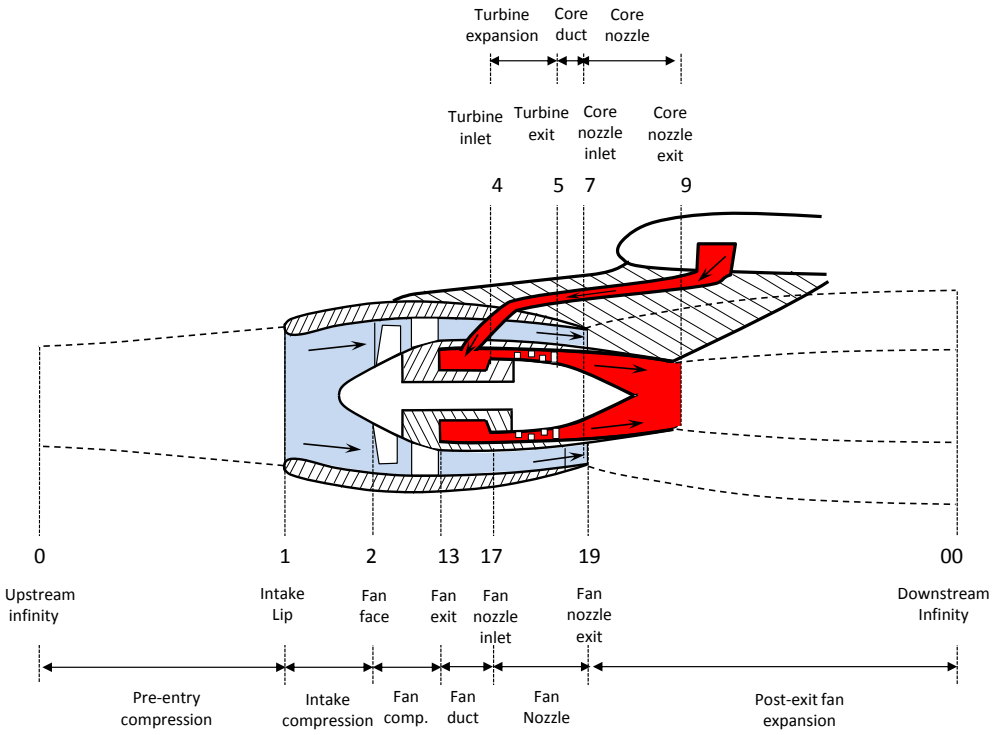

Figure A.1: Reference stations following SAE standards [42]

- 0: Upstream infinity
- 1: Intake lip
- 2: Fan face
- 13: Fan exit
- 4: Turbine inlet
- 5: Turbine exit
- 17: Fan nozzle inlet
- 7: Core nozzle inlet
- 19: Fan nozzle exit
- 9: Core nozzle exit
- 00: Downstream infinity.

B

Definitions of Interference Effects

In the following section several definitions are introduced useful in engine/airframe integration tests. These have been changing along the years according to the requirements of the engine and airframe manufacturers. A consistent approach, based on what was found in literature [16], [58] is presented.

B.1. Basic Definitions

The Drag of the aircraft at flow-through nacelle (TFN) conditions is equivalent to engine idle conditions and obtained from the measured balance force minus the internal drag of the nacelle. If instead of TFN a TPS is installed, idle conditions are achieved by equating the inlet and exhaust velocities.

$$D_{WBPN_{TFN}} = F_{BAL_{WBPN_{TFN}}} - D_{I,TFN} = \quad \text{(B.1)}$$

The Drag of the aircraft at power conditions D_{WBPN_P} is obtained from the measured balance force minus the net thrust, obtained from calibration data.

$$D_{WBPN_P} = F_{BAL,WT_{WBPN_P}} - F_N = \quad \text{(B.2)}$$

Also the isolated configuration Pylon/Nacelle can be investigated in wind-on conditions. In a similar way as before, the drag of Pylon/Nacelle at flow/through nacelle conditions is obtained through:

$$D_{PN_{TFN}} = F_{BAL_{PN_{TFN}}} - D_{I,TFN} = \quad \text{(B.3)}$$

The drag of the Pylon/Nacelle at power conditions is obtained through:

$$D_{PN_{TFN}} = F_{BAL_{PN_P}} - T_N = \quad \text{(B.4)}$$

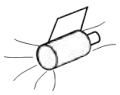

B.2. Engine/Airframe Definitions

Combining the precious estates is possible to obtain the installation and interference effects of the pylon/ nacelle and jet. The installation effect at TFN, $D_{INST_{TFN}}$ is defined as the addition drag due to the installation

of the engine at flow-through nacelle (idle) conditions.

$$D_{INST_{TFN}} = D_{WBPN_{TFN}} - D_{WB} \tag{B.5}$$

$D_{INST_{TFN}} =$ 

The interference effect is defined as the difference in drag between the combined $WBPN_{TFN}$ and isolated $WB + PN_{TFN}$ engine/airframe configuration at flow-through nacelle conditions. Additional tests in order to obtain the drag of the isolated pylon/nacelle at TFN conditions $D_{PN_{TFN}}$ are required.

$$D_{INT_{TFN}} = D_{WBPN_{TFN}} - (D_{WB} + D_{PN_{TFN}}) \tag{B.6}$$

$D_{INT_{TFN}} =$ 

This last formula can be used at any power condition, not only at flow-through nacelle:

$$D_{INT_P} = D_{WBPN_P} - (D_{WB} + D_{PN_P}) \tag{B.7}$$

$D_{INT_P} =$ 

In this last case the calibration of the TPS can be omitted, as far as the same power conditions are achieved for both the combined and the isolated pylon/nacelle configurations.

The power or jet effects are defined as the difference in drag between power conditions and flow-through nacelle conditions

$$D_{INST_P} = D_{AC,WBPN_P} - D_{AC,WBPN_{TFN}} \tag{B.8}$$

$$D_{INST_P} = \text{  } \tag{B.9}$$

The flow-through nacelle to power jet interference effects are the difference between the jet effects at the combined configuration minus the jet effects at the isolated pylon/nacelle configuration.

$$D_{INT_{TFN-P}} = (D_{WBPN_P} - D_{WBPN_{TFN}}) - (D_{PN_P} - D_{PN_{TFN}}) \tag{B.10}$$

$$D_{INT_{TFN-P}} = \text{  } \tag{B.11}$$

Also in this case the calibration of the TPS can be omitted as far as the power conditions are matched between the wing/body/pylon/nacelle and pylon/nacelle configurations.

The installation effect at power conditions or global installation drag is obtained by subtracting the drag of the powered model minus the drag of the clean configuration. Is defined as the addition of drag due to the installation of the engine at power conditions and equivalent to the sum of the installation at TFN and jet effect.

$$D_{AC,INST_G} = D_{WBPN_P} - D_{AC,WB} = D_{INST_{TFN}} + D_{INST_P} \tag{B.12}$$

$D_{AC,INST_G} =$ 

C

Additional CFD Results

C.1. Convergence History

The convergence history for a single CFD simulation is shown in Figure C.1 for the parameters of interest: Fan momentum, fan mass flow, fan exhaust velocity, fan exhaust pressure and boattail drag.

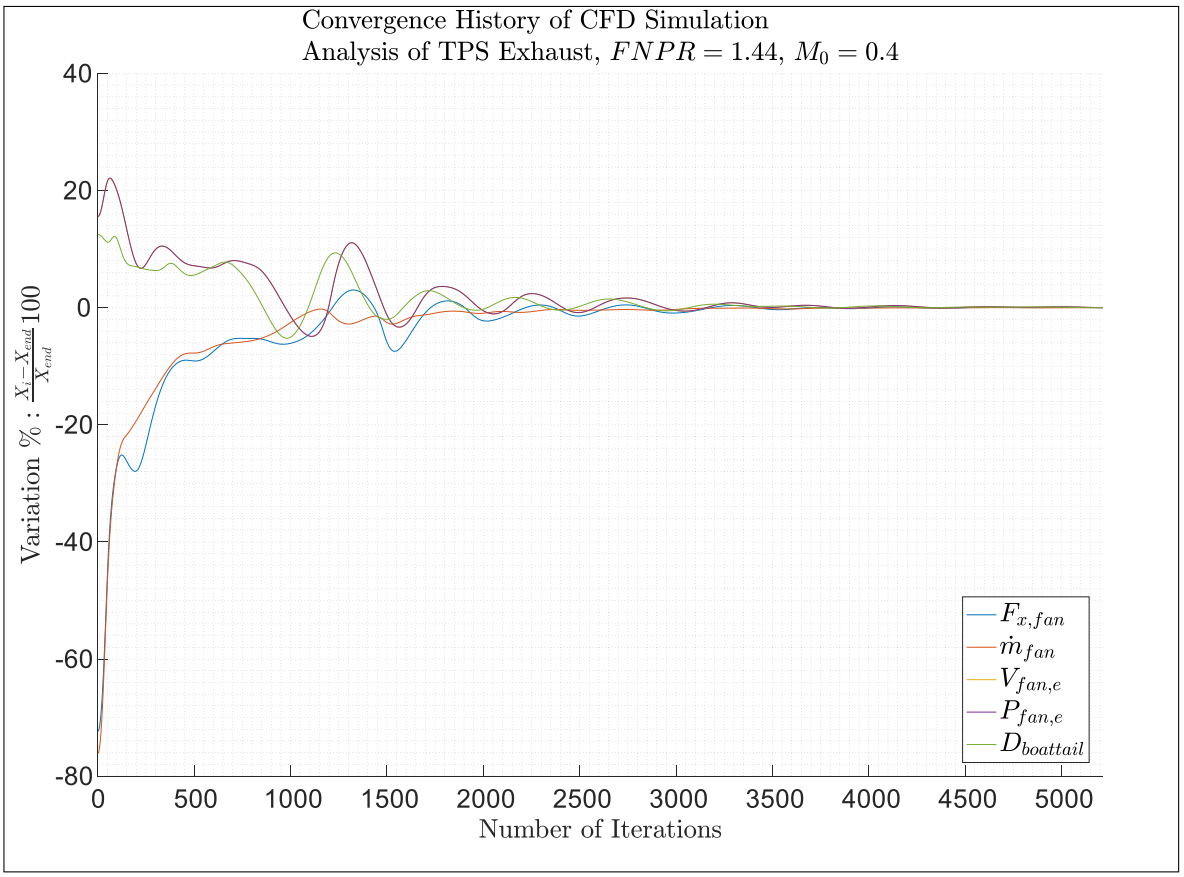

Figure C.1: Convergence history of variables of interest for analysis of TPS exhaust. $M_0 = 0.4, FNPR = 1.44$

C.2. Velocity Development

Figure C.2 shows the velocity development at different stations for the TPS exhaust at $FNPR = 1.58$ for calibration $M_0 = 0.01$ and wind tunnel conditions $M_0 = 0.4$.

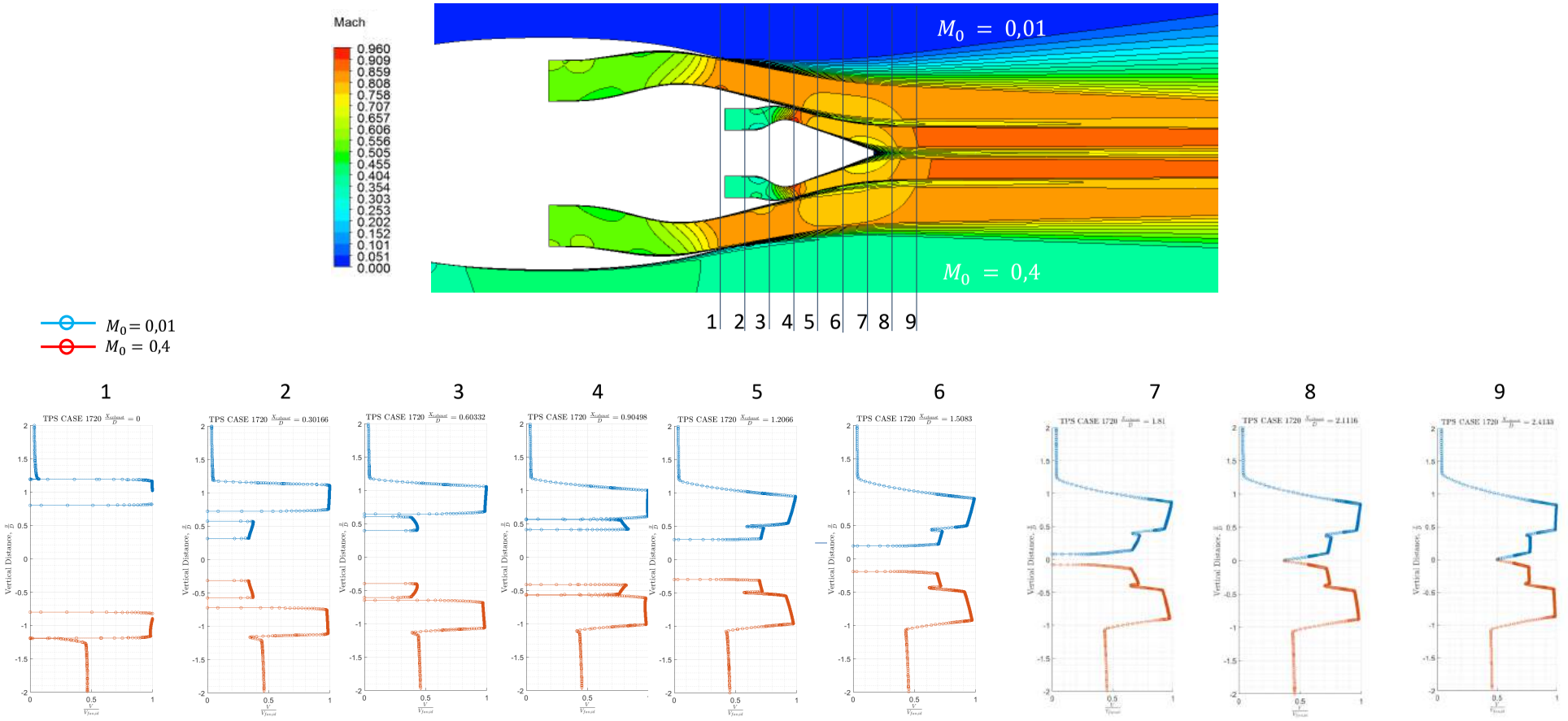

Figure C.2: Velocity development for the TPS exhaust at $FNPR = 1.58$ for calibration $M_0 = 0.01$ and wind tunnel conditions $M_0 = 0.4$.

D

AERODYNAMIC EFFECTS OF ENGINE/AIRFRAME

Several aerodynamic aspects occur as a result of the installation of high bypass ratio turbofan under the wing are identified, following *Harris* [5]:

1. Change in the spillage drag of the intake cowl due to the presence of the upwash, sidewash and the velocity field of the wing lift.
2. Development of the flow over the rear part of the fan cowl due to the pressure gradients that are imposed by the wing circulation.
3. Spillage drag development in the leading edge of the pylon as a result of the spilled air of the intake cowl, wing upwash and sidewash and wing leading edge influence.
4. Suction peak developed in the leading edge of the wing due to the addition of spilled air from the nacelle.
5. Development of a supersonic channel flow region inboard and outboard the gulley (vertical gap between nacelle and wing) with the appearance of a strong shockwave were mixing, separation and flow entrainment effects can occur.
6. Non-planar lifting effects due to vortex/viscous/wave drag effects produced by the interaction of the wing lift, pylon side lift, nacelle lift, and jet induced circulation. The lift is reduced due to the decrease of the wing lower surface pressure due to the fan jet velocity.
7. Local lift pocket on the wing on the nacelle station influencing viscous, lift induced and wave drag in the wing upper surface and increasing vortex drag.
8. Lift shedding and volume effects due to the presence of the pylon and nacelle affecting the supercritical flow development on the wing upper surface.
9. Over-expanded fan jet flow over the curved core cowling and pylon increasing friction drag in the submerged efflux with a strong terminal shock which also increases the wave and form drag.
10. Post Exit force due to the incomplete expansion of the flow to freestream conditions
11. Separation in the wing trailing edge as a result of the impingement of the turbulent flow from the jet exhaust .
12. Entrainment effects due to the mixing of external flow with the fan streamtube and the core and fan streamtubes.
13. Flow suppression in the nozzle: the presence of external flow increases the local pressure at the exhaust exit reducing the effective nozzle mass flow.

14. Boattail drag resulting from external air flowing over the afterbody.

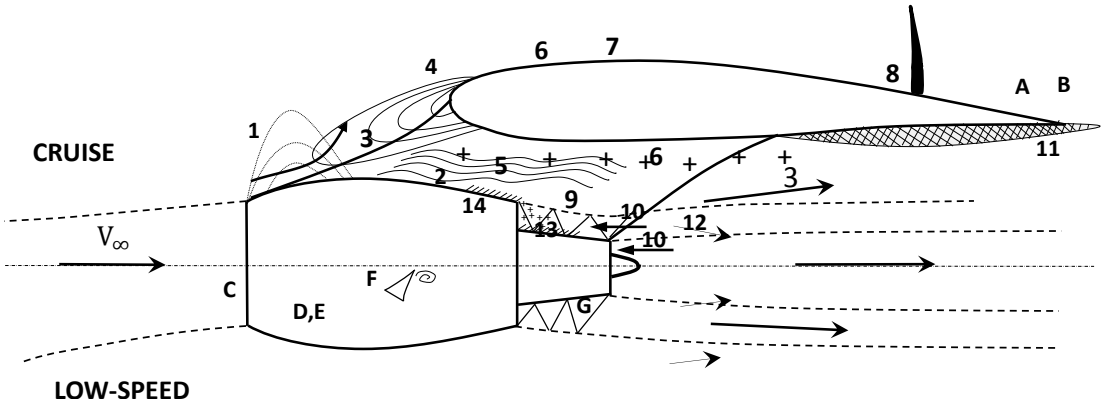

Figure D.1: Interference effects at cruise conditions on nacelle, pylon and wing [37] and [5]

Conditions outside of the envelope must be finely studied in order to capture any source of separation or adverse flow. For example, away from cruise a long cowl originates a strong interaction in the gulley, between the nacelle and the wing pylon. This interaction could cause shock induced separation of the boundary layer that trails downstream as a vortex. Then, more instrumentation is necessary to evaluate high or very high bypass ratio [7]. At low speed, the following interference effects may be present in addition of many of the above effects:

A Effect on nacelle due to interference with high lift devices: possibility of separation of the flow at the inlet cowl and at the aft cowl during second segment climb due to the influence of the proximity of the slat.

B Effect on high lift devices due to interference with exhaust plume: affect in aerodynamic performance (some effects could be favourable).

C Engine-out effects: windmilling and locked fan

D Nacelle thrust reverser exhaust flow field interferences.

E Thrust reverser exhaust interference such as drag cancellation (wipe out) and plume re-ingestion.

F Effect of nacelle strakes (vortex generators) at high angles of attack. These generate a powerful vortex that flows over the wing opposing to the strong upwash around the nacelle and providing a strong downwash marked by marginal trailing vortices, delaying flow separation.

G Higher flow spreading rate at lower Mach numbers influenced by the external flow. It increases the displacement effect and changes the recompression of the flow at the nacelle fan exhaust plane[2].

E

EFFECT OF NET THRUST IN DRAG

In the following Appendix the effects of an incorrect calibration of the net thrust is outlined. Following Figure E.1, we can find several situations:

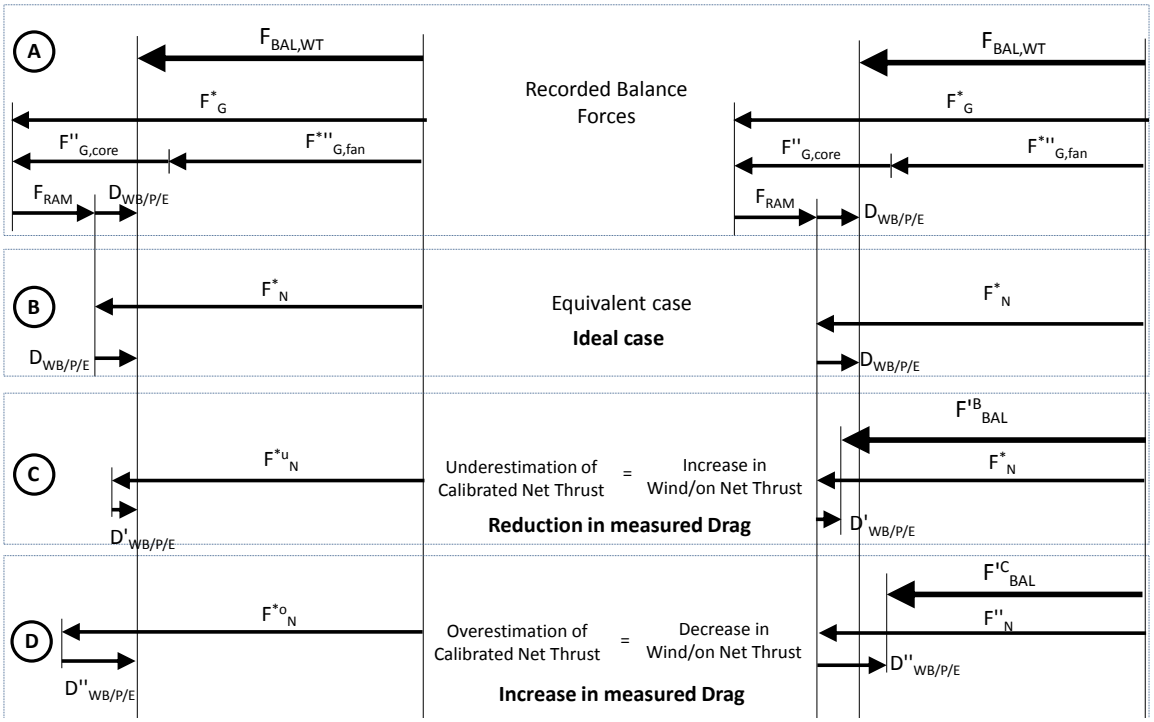

Figure E.1: Effect of static calibration in model drag

(A) The total forces in the wind tunnel model are represented. $F_{BAL,WT}$ is the force reading of the balance force in x direction at the wind tunnel model. It consists of the sum of the fan $F''_{G,fan}$ and core $F^{*''}_{G,core}$ modified gross thrust in x direction, the ram drag F_{RAM} and the model drag D_{WBPE}.

(B) Following from A, it is shown the ideal case: the total balance force is the sum of the modified net thrust F_N and the model Drag D_{WBPE}.

(C) The underestimation of the Calibrated Modified Standard Net Thrust, $F^{*u}_N < F^*_N$ follows with an underestimation of the model drag. The measured drag will be smaller than the real. This case is equivalent as if in wind-on conditions the Net Thrust increases respect to the calibration, as shown in the right of the figure.

(D) The overestimation of the Calibrated Net Thrust, $F_N^{*o} > F_N^*$ follows with the overestimation of the model drag. Then the measured drag will be higher than the real. This case is equivalent as if in wind-on conditions the Net Thrust is reduced respect to the calibration, as shown in the right. This can occur if the external flow affects the exhaust by flow suppression.

BIBLIOGRAPHY

[1] A. Einstein and L. Infeld, *The Evolution of Physics*, Essandess paperbacks (Cambridge University Press, Cambridge, 1971).

[2] H. Geyr and C. Rossow, *A Correct Thrust Determination Method for Turbine Powered Simulators in Wind Tunnel Testing,* in *41st AIAA/ASME/SAE/ASEE Joint Propulsion Conference & Exhibit*, July (American Institute of Aeronautics and Astronautics, Reston, Virigina, 2005) pp. 1–12.

[3] W. Burgsmüller and H. Hoheisel, *ENIFAIR — EU research into engine integration on future transport aircraft,* Air & Space Europe **2**, 81 (2000).

[4] A. Dumas, G. J, and M. L, *Analysis of ENIFAIR High Speed Test Results, an Evaluation of Interference Effects,* in *Workshop on EU-Research on Aerodynamic Engine/Aircraft Integration for Transport Aircraft,* edited by DLR (Braunschweig, Germany, 2000).

[5] A. HARRIS and K. PALIWAL, *Civil turbofan propulsion system integration studies using powered testing techniques at ARA, Bedford,* in *13th Aerodynamic Testing Conference* (American Institute of Aeronautics and Astronautics, Reston, Virigina, 1984).

[6] W. Burgsmuller, C. Castan, H. Hoheisel, and J. W. Kooi, *Preparation and Use of TPS-Technique for Low Speed Investigations on Transport Aircraft,* in *International Forum on Turbine Powered Simulation* (Marknesse, the Netherlands, 1995).

[7] A. E. Harris, *Test Techniques for Engine/Airframe Integration*, Tech. Rep. (Aircraft Research Association Ltd, Bedford, 1992).

[8] MIDAP Study Group, *Guide to In-Flight Thrust Measurement of Turbojets and Fan Engines*, agard-ag-2 ed. (Defense Technical Information Center, London, 1979).

[9] D. Daggett, S. Brown, and R. Kawai, *NASA*, NASA CR-2003-212309 (NASA Center for AeroSpace Information, 2003).

[10] G. H. Hegen and K. R, *Experiences with ultra-high bypass simulators from calibration and isolated engine testing,* International Forum on Turbine Powered Simulation (1995).

[11] J. Kooi, L. de Haij, and G. Hegen, *Engine Simulation with Turbofan Propulsion Simulators in the German-Dutch Wind Tunnels (Invited),* in *22nd AIAA Aerodynamic Measurement Technology and Ground Testing Conference* (American Institute of Aeronautics and Astronautics, Reston, Virigina, 2002).

[12] W. B. De Wolf, *Possibilities and limitations of VHBR and UHBR turbofan simulations in engine-airframe integration wind tunnel experiments,* in *Aspects of Engine-Airframe Integration for Transport Aircraft. Proceedings of the DLR Workshop Braunschweig* (DLR, Braunschweig, Germany, 1996).

[13] W. BURGSMUELLER and J. SZODRUCH, *Benefits and costs of powered engine simulation at low speeds,* in *23rd Aerospace Sciences Meeting* (American Institute of Aeronautics and Astronautics, Reston, Virigina, 1985).

[14] H. Hoheisel, *Aerodynamic aspects of engine-aircraft integration of transport aircraft,* Aerospace Science and Technology **1**, 475 (1997).

[15] J. E. McCall, P. Tracksdorf, and K. Heinig, *Advanced Ducted Engine Nacelle Aerodynamics and Integration Testing,* Journal of Engineering for Gas Turbines and Power **114**, 802 (1992).

[16] G. Doornbos and W. B. De Wolf, *The Engine/Airframe Interference Drag at Cruise Conditions, Using Propulsion Simulation*, Tech. Rep. (NLR, Marknesse, 1983).

[17] A. E. Harris, J. T. Kutney, and F. B. Ogilvie, *25 Years of Turbine Powered Simulation Success.pdf,* in *International Forum on Turbine Powered Simulation* (Marknesse, the Netherlands, 1995).

[18] D. M. Tompkins, J. D. Flamm, K. R. Long, and K. D. James, *Experimental Validation of Modifications to a TDI Model 2700 Turbine Powered Simulator to Simulate a High-Bypass Ratio Engine,* in *50th AIAA/ASME/SAE/ASEE Joint Propulsion Conference* (American Institute of Aeronautics and Astronautics, Reston, Virginia, 2014).

[19] H. R. WELGE and J. R. ONGARATO, *Powered -Engine Simulator Procedures and Experience for the DC-10 Wing Engine,* Journal of Aircraft **8**, 523 (1971).

[20] M. Laban, B. Soemarwoto, and J. Kooi, *Reshaping Engine Nacelles for Testing in Wind Tunnels with Turbofan Propulsion Simulators,* in *41st AIAA/ASME/SAE/ASEE Joint Propulsion Conference & Exhibit* (American Institute of Aeronautics and Astronautics, Reston, Virigina, 2005) pp. 1–12.

[21] H. Hoheisel and H. Frhr. von Geyr, *The influence of engine thrust behaviour on the aerodynamics of engine airframe integration,* CEAS Aeronautical Journal **3**, 79 (2012).

[22] D. Eckert, V. Van Ditshuizen, B. Munniksma, and W. Burgsmuller, *Low Speed Twin Engine Simulation on a Large Scale Transport Aircraft Model in the DNW,* International Council of the Aeronautical Sciences **2**, 81 (1984).

[23] J. Kooi, N. Corby, J. Becle, and G. Hegen, *TPS Calibration Procedures,* in *International Forum on Turbine Powered Simulation* (Marknesse, the Netherlands, 1995).

[24] G. W. Hall, *Application of Boundary Layer Theory To Explain Some Nozzle and Venturi Flow Peculiarities,* SAE **173** (1959).

[25] R. DECHER and D. TEGELER, *High accuracy force accounting procedures for turbopowered simulatortesting,* in *11th Propulsion Conference* (American Institute of Aeronautics and Astronautics, Reston, Virigina, 1975).

[26] J. ONGARATO, *Powered engine simulator procedures and experience for the DC-10 wing engine at high subsonic speeds,* in *Propulsion and ASW Meeting* (American Institute of Aeronautics and Astronautics, Reston, Virigina, 1970).

[27] F. W. Steffen, E. A. Satmary, M. R. Vanco, and S. M. Nosek, *A Turbojet Simulator for Mach Numbers up to 2,* in *Sixteenth Annual International Gas Turbine Conference and Products Show* (San Francisco, CA, 1972).

[28] E. Meleason and O. Wells, *Investigation of upper-surface-blowing nacelle integration at cruisespeeds utilizing powered engine simulators,* in *12th Propulsion Conference* (American Institute of Aeronautics and Astronautics, Reston, Virigina, 1976).

[29] R. K. Rowe, *Nozzle Performance Calibration and Turbomachinery Operational Analysis of the Turbo-Powered Simulators (TPS) for the NASA-Langley EET Propulsion Airframe Integration Investigation,* Tech. Rep. (NASA, Hampton, 1984).

[30] P. R. Shea, J. D. Flamm, K. Long, K. D. James, D. Tompkins, and M. D. Beyar, *Turbine Powered Simulator Calibration and Testing for Hybrid Wing Body Powered Airframe Integration (Invited),* in *54th AIAA Aerospace Sciences Meeting* (American Institute of Aeronautics and Astronautics, Reston, Virginia, 2016).

[31] J. Becle, P. Desplas, and R. Perin, *Progress on engine airframe integration - Aerospatiale's experience in ONERA's large wind tunnels,* in *25th Plasmadynamics and Lasers Conference* (American Institute of Aeronautics and Astronautics, Reston, Virigina, 1994).

[32] C. Sabater Campomanes, *Engine/Airframe Integration Testing at the German-Dutch Wind Tunnels,* Ph.D. thesis, TU Delft (2017).

[33] Rolls-Royce, *Gas Turbine Technology - Introduction to a jet engine,* Tech. Rep. (2007).

[34] G. H. Hegen, *NLR TR 96576 L Test report of force and flowfield measurements on the ALVAST half model in the low speed wind tunnel LST phase 1. Test Number: 5619*, Tech. Rep. (NLR, Marknesse, the Netherlands, 1995).

[35] N. L. En, *NLR-TR-94442-L Calibration of a Through Flow Nacelle Model of a Counter Rotating Ultra-High Bypass Fan Simulator in the Model Engine Calibration Facility*, Tech. Rep. (NLR, Marknesse, the Netherlands, 1993).

[36] E. Torenbeek, *Synthesis of Subsonic Airplane Design* (Springer Netherlands, Dordrecht, 1982).

[37] E. E. Covert, *Thrust and Drag: Its Prediction and Verification*, edited by W. F. Kimzey, E. E. Covert, E. C. Rooney, G. K. Richey, and C. R. James (American Institute of Aeronautics and Astronautics, New York, 1985).

[38] E. Obert, *Aerodynamic Design of Transport Aircraft* (Ios Press ; Delft University of Technology, Faculty of Aerospace Engineering, Section Design of Aircraft and Rotorcraft, Amsterdam, 2009) p. 657.

[39] O. F. Supply, *Definitions of the Thrust of a Jet Engine and of the Internal Drag of a Ducted Body*, Journal of the Royal Aeronautical Society **59**, 517 (1955).

[40] A. Mair, D. Bottle, R. Pankhurst, T. Somerville, C. Vernon, C. Warren, E. Rogers, S. Gray, H. Pearson, and J. Seddon, *Report of the Definitions Panel on Definitions to be used in the Description and Analysis of Drag*, (1958).

[41] P. G. Street, *Thrust Drag Analysis for a Front Fan Nacelle having Two Separate Coaxial Fan Nacelle having Two Separate Coaxial Exhaust Streams*, Tech. Rep. (National Gas Turbine Establishment, 1973).

[42] SAE Technical Committee E-33, *In-Flight Thrust Determination and Uncertainty, SP-674* (Society of Automotive Engineers, Inc, Pennsylvania, 1986).

[43] D. O. Dommasch, *Performance: Flight Testing* (Pergamon Press, Michigan, 1959) pp. 2:23–2:28.

[44] J. E. Green, *Short-Cowl Front-Fan Turbojets: Friction Drag and Wall-jet Effects on Cylindrical Afterbodies*, Tech. Rep. (Aeronautical Research Council, Bedford, UK, 1969).

[45] V. Czitrom, *One-Factor-at-a-Time versus Designed Experiments*, The American Statistician **53**, 126 (1999).

[46] G. E. P. Box, J. S. Hunter, and W. G. Hunter, *Statistics for Experimenters. Design, Innovation and Discovert*, 2nd ed. (John Wiley & Sons Inc, 2005).

[47] Y. Zhang, H. Chen, M. Zhang, M. Zhang, Z. Li, and S. Fu, *Performance Prediction of Conical Nozzle Using Navier–Stokes Computation*, Journal of Propulsion and Power **31**, 192 (2015).

[48] R. Tognaccini, *Drag Computation and Breakdown in Power-on Conditions*, Journal of Aircraft **42**, 245 (2005).

[49] D. Yoder, V. Dippold, and N. Georfiadis, *Wind-US Results for the AIAA 1st Propulsion Aerodynamics Workshop*, in *AIAA 1st Propulsion Aerodynamics Workshop* (Atlanta, GA, 2012) pp. 1–35.

[50] R. L. Thornock and E. F. Brown, *An Experimental Study of Compressible Flow Through Convergent-Conical Nozzles, Including a Comparison With Theoretical Results*, Journal of Basic Engineering **94**, 926 (1972).

[51] Z. Li, H. Chen, and Y. Zhang, *NSAWET Results of the Dual Separate Flow Reference Nozzle from AIAA PAW02*, in *51st AIAA/SAE/ASEE Joint Propulsion Conference* (American Institute of Aeronautics and Astronautics, Reston, Virginia, 2015) pp. 1–7.

[52] D. Li, S. Venkateswaran, K. Fakhari, and C. Merkle, *Convergence assessment of general fluid equations on unstructured hybrid grids*, in *15th AIAA Computational Fluid Dynamics Conference* (American Institute of Aeronautics and Astronautics, Reston, Virigina, 2001).

[53] R. L. Thornock, *Comparison of Participant Analyses with Experimental Results for Conical Nozzle Flowfields and Performance*, in *49th AIAA/ASME/SAE/ASEE Joint Propulsion Conference* (American Institute of Aeronautics and Astronautics, Reston, Virginia, 2013).

[54] R. L. Thornock, *Propulsion AerodynamicWorkshop II, Summary of Participant Results for a Dual Separate Flow Reference Nozzle, Including Some Experimental Results*, 52nd AIAA/SAE/ASEE Joint Propulsion Conference , 1 (2016).

[55] P. Bradshaw and E. Love, *The Normal Impingement of a Circular Air Jet on a Flat Surface*, Tech. Rep. (Aeronutical Research Council, Aerodynamics Division, Bedford, UK, 1961).

[56] K. Masatsuka, *I do like CFD, VOL.1, Second Edition*, v. 1 (K. Masatsuka, 2013).

[57] R. W. Johnson, *Handbook of Fluid Dynamics* (CRC Press, 2016).

[58] H. Hoheisel, *Engine Thrust Determination for Wind Tunnel Experiments*, in *Workshop on EU-Research on Aerodynamic Engine/Aircraft Integration for Transport Aircraft*, edited by DLR (Braunschweig, 2000).